

LAPPEENRANTA UNIVERSITY OF TECHNOLOGY

LUT School of Energy Systems

LUT Mechanical Engineering

Atte Posa

**VIBRATION BEHAVIOR OF A CENTRIFUGAL PUMP WITH INTEGRATED
PERMANENT MAGNET MOTOR**

Examiners: Prof. Jussi Sopanen

D.Sc. (Tech.) Janne Heikkinen

TIIVISTELMÄ

Lappeenrannan teknillinen yliopisto
LUT Energiajärjestelmät
LUT Kone

Atte Posa

Keskipakopumpun värähtelykäyttäytyminen integroidulla kestopagneettimoottorilla

Diplomityö

2016

88 sivua, 59 kuvaa, 12 taulukkoa ja 4 liitettä

Tarkastajat: Professori Jussi Sopenen
Tkt Janne Heikkinen

Hakusanat: , Sähkömagneettinen voima, Epätasainen magneettinen veto, epäkeskeinen ilmarako, Kestomagneettimoottori, Värähtely, Simulointi, värähtelymittaus

Tässä työssä tutkitaan roottorin ja staattorin yhdistävien sähkömagneettisten voimien luonnetta ja niiden yhteyttä moottorin rakenteeseen. Sähkömagneettisten voimien suhdetta systeemin värähtelykäyttäytymiseen tutkitaan rakentamalla simulointimalli keskipakopumpusta joka on varustettu integroidulla kestopagneettimoottorilla. Simulointimallin verifiointi tapahtuu vertaamalla tuloksia prototyypillä suoritettuihin mittauksiin. Nykyiset simulointimetodit eivät huomioi sähkömagneettisia voimia roottorin ja staattorin välillä, antaen väärät rajat moottorin turvalliselle käyttöalueelle.

Epätasaista magneettista vetoa roottorin ja staattorin välillä simuloidaan lineaaristen jousi-elementtien avulla asettamalla näille negatiivinen jousivakio. Roottorin ja staattorin välinen radiaalisuuntainen vetovoima määräytyy jousen pituuden mukaan. Systeemin ominaistajuuksien ja värähtelynopeuksien selvittämiseen eri ilmaraon epäkeskeisyyksillä käytetään ANSYS Mechanical-ohjelman moodi- ja harmoonista analyysiä. Värähtelykäyttäytymistä tutkitaan asettamalla herätteeksi samansuuruinen massaepätasapaino simulointimalliin, sekä prototyyppiin ja mittaamalla värähtelynopeudet 0, 10 ja 20 % epäkeskeisellä ilmaraolla.

Simuloinnin tulokset osoittivat kuinka neljän ensimmäisen värähtelymuodon ominaistajuudet laskevat huomattavasti kun sähkömagneettiset voimat huomioidaan. Ensimmäisen muodon ominaistajuus laski 137 Hz:stä 34 Hz:iin ja toinen 144 Hz:stä 50 Hz:iin. Moottorin pyörimisnopeus alue on 68 Hz:iin saakka, joten käyttämällä tätä metodia moottorin pyörimisnopeusalueelta pystytään löytämään kaksi kriittistä nopeutta. Ilmaraon epäkeskeisyyden suhdetta värähtelynopeuteen tutkittiin, mutta näillä ei löydetty olevan selkeää yhteyttä. Myös staattorin virran suhdetta ominaistajuuksiin tutkittiin. Kun staattorin virta kasvoi, ominaistajuuksien huomattiin laskevan. Tämän tutkimuksen mukaan sähkömagneettiset voimat on syytä ottaa huomioon määrittäessä integroidulla moottorilla varustetun pumpun kriittisiä nopeuksia.

ABSTRACT

Lappeenranta University of Technology
LUT School of Energy Systems
LUT Mechanical Engineering

Atte Posa

Vibration behavior of a centrifugal pump with integrated permanent magnet motor

Master's thesis

2016

88 pages, 59 figures, 12 tables and 4 appendices

Examiner: Professor Jussi Sopenen
D.Sc (Tech) Janne Heikkinen

Keywords: Electromagnetic force, Unbalanced Magnetic Pull, UMP, Air gap eccentricity, Permanent Magnet Motor, Vibration, Simulation, vibration measurement

In this research, nature of electromagnetic forces which couples rotor and stator together and their relation to engine structure is discussed. Simulation model of a centrifugal pump with integrated permanent magnet motor is constructed in order to investigate the effect of electromagnetic forces to system vibration behavior. Simulation model is verified by comparing results to experimental measurements with a prototype. Current simulation methods do not take into account the unbalanced magnetic pull caused by electromagnetic forces between rotor and stator giving false limits to safe engine operation range.

Unbalanced magnetic pull is simulated by introducing linear spring elements with negative spring constant between rotor and stator. The attractive force between rotor and stator in radial direction is adjusted based on the spring length. Modal and Harmonic analyses are performed using ANSYS Mechanical software to inspect natural frequencies and vibration velocities with variable air gap eccentricities. The vibration behavior is inspected by applying equal size unbalanced mass as an excitation source for the simulation model and prototype, after which the vibration velocities are measured with air gap eccentricities of 0, 10 and 20 %.

Simulation results showed how natural frequency of first four vibration modes decreased significantly when the electromagnetic forces were taken into account. Natural frequency of the first mode decreased from 137 Hz to 34 Hz and second from 144 Hz to 50 Hz. Since the engine speed of the prototype was up to 68 Hz, two critical speeds could be discovered in the operating speed range by using this method. Vibration velocity with variable air gap length was inspected, but clear relation between air gap eccentricity and vibration velocity could not be found. Also stator current relation to natural frequencies was investigated. It was found that by increasing stator current the natural frequencies decreased. According to this research the electromagnetic forces need to be taken into account when determining critical speeds of an integrated pump-motor assembly.

ACKNOWLEDGEMENTS

First of all, I would like to thank Sulzer Pumps Finland Oy for providing me the most interesting topic for my Master's thesis. Special thanks to Kalle Tarhonen for the guidance and discussions during the process. I would also like to show my gratitude to Professor Jussi Sopenen and Doctor of Science Janne Heikkinen for the encouraging comments during this work.

I would like to thank my family for the support and encouragement throughout my studies. Most of all, I will always be grateful for the friends I made during my studies in Lappeenranta University of Technology. They provided crucial balance for my studies by making sure the time between and after lectures was never boring.

Atte Posa

In Kotka, 1st of December 2016

TABLE OF CONTENTS

TIIVISTELMÄ

ABSTRACT

ACKNOWLEDGEMENTS

TABLE OF CONTENTS

LIST OF SYMBOLS AND ABBREVIATIONS

1	INTRODUCTION	9
1.1	Research problem	9
1.2	Definition of research frames	11
2	EXCITATIONS IN PERMANENT MAGNET MACHINES	12
2.1	Recent development of permanent magnet motors.....	12
2.1.1	Radial flux motors	15
2.2	New phenomena, requirements and benefits brought by an integrated motor	18
2.2.1	Bearing and shaft requirements	19
2.3	Basic concept of vibration	19
2.4	General sources of vibration	22
2.5	Electromagnetic sources of vibration	25
2.5.1	Radial excitation	25
2.5.2	Tangential excitation.....	32
2.6	Mechanical sources of vibration	33
2.6.1	Gyroscopic effect.....	36
3	MODELING AND VERIFICATION OF EXCITATIONS.....	38
3.1	Geometry	39
3.2	Material properties	42
3.3	Finite Element Mesh.....	42
3.4	Constraints	44

3.5	Joints and contacts	44
3.6	Modeling of electromagnetic force	45
3.7	Modal Analysis	47
3.7.1	Modal analysis with varying motor load	49
3.7.2	Modal analysis with variable air gap	51
3.7.3	Gyroscopic effect with variable air gap	53
3.8	Harmonic response analysis.....	54
3.9	Experimental tests.....	56
3.9.1	Static eccentricity.....	59
3.9.2	Measurement results	60
3.10	Verification of the simulation model	65
4	COMPARISON OF SIMULATION MODEL AND PROTOTYPE	68
4.1	Comparison with static 10 % eccentricity error.....	68
4.2	Effect of unequally distributed air gap to vibration velocities.....	70
4.3	Effect of stator current on system behavior	74
4.4	Discussion.....	77
4.4.1	Simulation model accuracy compared to prototype	77
4.4.2	Possible errors in the simulation model.....	78
5	CONCLUSIONS	81
5.1	Further research	84
	REFERENCE.....	85

APPENDICES

Appendix I: Simulation model contact pairs

Appendix II: Natural frequencies and mode shapes for concentric rotor/stator

Appendix III: ANSYS Commands

Appendix IV: Measurement results

LIST OF SYMBOLS AND ABBREVIATIONS

A	Amplitude
A_1	Coefficient for initial condition of undamped system
A_2	Coefficient for initial condition of undamped system
B	Magnetic flux density
B_r	Remnant magnetic flux density
BH_{max}	Theoretical maximum energy product
e	Air gap length of static eccentricity in measurement cases
F	Force
F_r	Radial force between rotor and stator in spring rate calculation
f_0	Externally applied force divided by mass
F_0	Externally applied force
F_{Fn}	Normal force acting between rotor and stator
$F_{m\ dyn}$	Dynamic radial force
$F_{m\ stat}$	Static radial force
H	Magnetic field intensity
J_p	Polar mass moment of inertia of the rotor
k	Spring rate
l_s	Spring length
m	Mass
M_G	Gyroscopic moment
n	Rotating speed of a motor
p	Number of pole pairs
S	Air gap area
t	Time in seconds
X	Amplitude of the forced response
x	Displacement
\ddot{x}	Acceleration
x_p	Particular solution
α	Angular misalignment of stator

β	Angle of motor frame / rotor deflection
ε_{stat}	Static eccentricity
ε_{dyn}	Dynamic eccentricity
Δg	Whirling radius of rotor
$\dot{\theta}$	Angular velocity of change of orientation of the rotating axis
θ_e	Electrical rotor angular position
μ	Permeability of a specific material
μ_0	Permeability in vacuum
σ_F	Maxwell's stress tensor
σ_{Fn}	Normal component of Maxwell's stress tensor
δ_{max}	Maximum air gap length
δ_{min}	Minimum air gap length
ϕ	Phase angle / magnetic flux calculated over a surface perpendicular to its direction of magnetization
Ω	Angular velocity of the rotor
ω	Frequency of externally applied force
ω_n	Natural frequency
ω_w	Whirling direction
1X	Once-rotation speed excitation
2X	Twice-rotation speed excitation
DC	Direct current
FFT	Fast Fourier Transform
IM	Induction Motor
MPC	Multi-Point Constraint
PM	Permanent Magnet
SRM	Switched Reluctance Motor
UMP	Unbalanced Magnetic Pull

1 INTRODUCTION

Centrifugal pumps are based on centrifugal effect which is used to transform rotational energy into hydraulic energy of the fluid. Centrifugal pumps are used in industry in several different applications to pump for example clean or viscous liquids and fluids containing large particles or gas. Centrifugal pumps are often driven with electric motors. Traditionally electric motors have been driven with induction motors coupled to the pump through a coupling. Development of electric motors has brought integrated equipment as an important part of centrifugal pumps. Flange motors with an adapter and a coupling are being replaced by permanent magnet (PM) motors with axial and radial flux. The PM motor makes it possible to integrate the motor to a same shaft with a pump without need of own bearing unit. Usage of the same shaft and bearing unit brings up new dynamic phenomena which should be taken in to account already in product development process to be able to predict vibration behavior of the whole pump assembly. Also effect of defects during the installation and manufacturing of the components should be possible to predict.

1.1 Research problem

Traditionally electric motor has its own bearing unit, so the static load from motor mass and dynamic load due to high rotational speed is divided to several different supports. Structure of the pump assembly changes substantially when an electric motor is integrated to a same bearing unit with a pump. In this case one bearing unit takes all the static and dynamic load of the motor. Absence of one bearing unit lets the rotor hang inside of the stator without proper support, making the assembly more prone to vibrations. However, PM motors make it possible to run the assembly without a second bearing unit. Usage of just one bearing unit brings new benefits such as reduced materials, components and losses. Figure 1 shows an example of a centrifugal pump with an integrated electric motor.

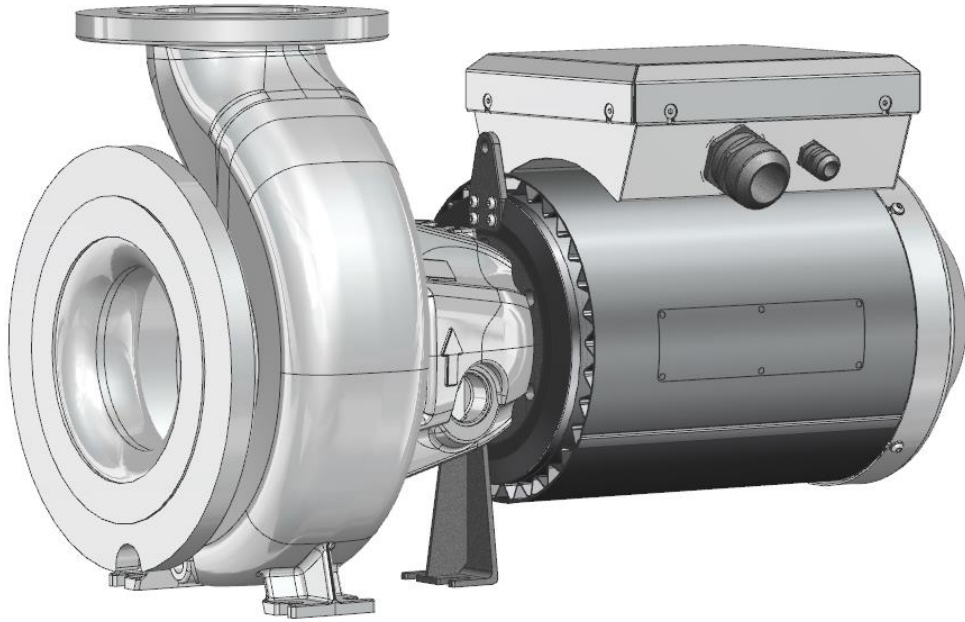


Figure 1. Centrifugal pump with integrated electric motor.

Use of the same bearing unit and shaft for the pump and motor has also its drawbacks. Experimental tests have shown unwanted vibration behavior especially on twice-rotation speed (2X) frequency, which is a realistic operation area in applications where integrated electric motor could be used. The occurring resonance effects even the balancing of the electric motor making it complex and time consuming process. Due to errors in the manufacturing or assembling stage the rotor might be left misaligned with respect to stator. The misaligned rotor is then prone to unbalanced magnetic pull (UMP). Together with bearing clearance, bearing installation errors and shaft alignment the vibration amplitudes can grow so high that in worst case the rotor makes contact with stator during operation and causes failure of the electric motor.

In order to avoid harmful behavior, differences in design, assembling and electromagnetic force distribution should be possible to simulate during the product development process. In order to explore the vibration behavior, a simulation model of a centrifugal pump with integrated radial flux PM motor is constructed. Possible errors which increase the UMP are forced in to the physical prototype and vibration levels are measured with accelerometers. After this the same error is introduced to the simulation model. Modal and harmonic analyses are performed to inspect the simulation model behavior and finally simulation

results are compared to the physical measurements in order to verify the simulation model accuracy.

1.2 Definition of research frames

This Master's Thesis is done for Sulzer Pumps Finland into department of product development in co-operations with Lappeenranta University of Technology. In this work research is limited to permanent magnet motors with radial flux. In the simulation model vibration sources are described in terms of mechanics without going too much into details in electrical engineering. This meaning that for example magnetic forces inside the electric motor are modeled as linearized spring forces acting in elements in the radial direction. In this way an understandable approach to vibration behavior of integrated electric motors is tried to give for designers who are mainly from the field of Mechanical Engineering.

Main research questions in this work are:

- How are the electromagnetic forces coupled with engine vibrations?
- How do the electromagnetic forces depend on motor structure?
- How can the electromagnetic forces be simulated during the design process?

2 EXCITATIONS IN PERMANENT MAGNET MACHINES

To be able to describe vibration sources in integrated pump-motor assembly, the theory behind the components needs to be discussed. In this section recent development of motors, reasons for the usage of PM motors and use of mutual shaft and bearing unit is discussed to find out the reasons behind this kind of new design approach. Also vibration phenomena occurred due to this new approach and reasons to it are discussed based on literature.

2.1 Recent development of permanent magnet motors

One of the most recent topics in electric motors is the development of permanent magnet motors. PM motors have been truly studied since beginning 20th century, but they became more common in 1980's when discovering of new magnetic materials made it possible to produce cheap PM motors with high energy production.

Traditionally induction motors have been used widely in industry. In Sulzer Pumps still over 90 % of the used motors are induction motors (Virtanen 2016). However, during the last 20 years PM motors have developed to compete with the traditional motor options mainly because of magnetic material development. PM materials have been studied since 19th century. First big development in magnetic materials was discovering of Alnico, after which ferrite magnet materials were discovered in the 1960s. They dominated the magnet industry until year 1983 when neodymium-iron-boron ($\text{Nd}_2\text{Fe}_{14}\text{B}$) magnets were developed by General Motors and Sumimoto. Driving factor in development of permanent magnets was the rapidly developing automotive industry which required small size, high energy and low cost magnets for electric motor applications. (Overshott 1991, p. 22–28.) Recently also Nanocomposites (combination of hard and soft magnetic materials) have been studied to produce very high-energy products. Nanocomposites have potential to reach theoretical maximum energy product (BH_{max}) values of ~90 MGOe which is 37 % more powerful compared to best reported sintered NdFeB magnet (56.7 MGOe). As the energy in magnets increases, it makes possible to get more power from the existing size motors or reduce the motor size with more powerful magnets. The magnetic field produced by a permanent magnet can be characterized with remnant magnetic flux density (B_r). When the permanent

magnets get more powerful, also the remnant flux density increases. If B_r is increased with 23 %, the output power increases by 20 % or the engine size can be reduced by 20 %. (Deshpande 2003, p. 510–514.)

Induction motors are widely used in industry because of their simple structure and good adjustability with the help of frequency converters. The main components of an induction motor are rotor which rotates inside a stator, which stays stationary. Operation of an induction motor is based on rotating magnetic field in the rotor. In industry the rotating magnetic field is often developed with the help of symmetrical three-phase winding. The winding is distributed equally in segments around the rotor and excited by an alternating current. Three-phase current is guided to the windings with equal phase differences and thus the voltage (and magnetic field) status becomes identical as it was in the previous segment. This occurs as a physical rotation of the magnetic field around the stator. (Aura & Tonteri 1996, p. 305–307.)

PM motors are synchronous machines in which the magnetization of the rotating rotor is produced by permanent magnets. By using permanent magnets the efficiency of the motor increases since they do not require extra current to produce the magnetic field unlike the magnetization produced by winding. When current is used, there are always some current losses. Torque is developed by placing permanent magnets on the rotor yoke and sequentially energizing the phase windings in stator. Figure 2 illustrates a structure of a PM motor with four poles and 12 slots. (Hanselman 2006, p. 4, 9–10.)

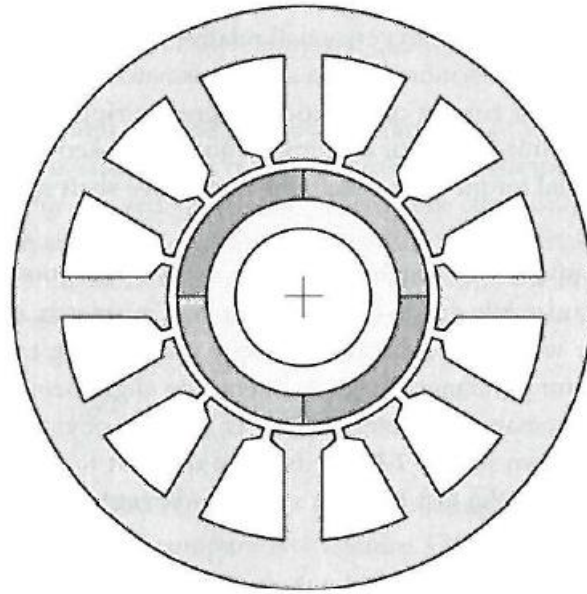


Figure 2. Cross section of a four pole, 12 slot motor (Hanselman 2006, p. 112).

Zeraoulia, Benbouzid & Diallo (2006) have compared in their research Direct Current (DC), Induction (IM), Permanent magnet and Switched Reluctance Motors (SRM). They were trying to find possible motor options for hybrid electric vehicles but the same motors are used in pump industry as well. Table 1 presents comparison they have made in terms of power density, efficiency, controllability, reliability, technological maturity and cost. Noticeable is the clearly highest values for PM motor power density and efficiency compared to competitors, which has been the driven factors to replace induction motors. (Zeraoulia, Benbouzid & Diallo 2006, p. 1756–1764.)

Table 1. Motor comparison (Zeraoulia, Benbouzid & Diallo 2006, p. 1761).

Characteristics	DC	IM	PM	SRM
Power Density	2.5	3.5	5	3.5
Efficiency	2.5	3.5	5	3.5
Controllability	5	5	4	3
Reliability	3	5	4	5
Technological maturity	5	5	4	4
Cost	4	5	3	4
Σ Total	22	27	25	23

Induction motors have been widely used in industry because of their reliability, low maintenance requirement, low cost and ability to operate in hostile environments. However their power density is considerably lower compared to PM motors especially in high-speed range. Higher power density means that the overall weight is much less compared to output power. (Zeraoulia, Benbouzid & Diallo 2006, p. 1759.) In addition, induction motors are not as efficient as PM motors: according to Puranen (2006, p. 29) “The biggest drawback of the induction machine is the always lagging power factor, because the machine is magnetized from the stator, in other words, there is a magnetizing current flowing in the stator winding even at no-load conditions.” This results as decreased torque with equal current (Puranen 2006, p. 29).

PM motors are more efficient, they have higher power density and their heat is efficiently dissipated to surroundings, but there is a risk of permanent magnet demagnetization making the PM motor not as reliable as an induction motor. They have also relatively short development lifetime since they have been efficiently developed since 1983 and induction motors from the beginning of 1900’s making the induction motor technology better known and one of the reasons for its wide spread in industry. Traditionally induction motors have been also cheaper to manufacture. One other interesting motor option is the SRM since it provides cost-effective and reliable option, but its efficiency does not reach the values of PM motors. (Zeraoulia, Benbouzid & Diallo 2006, p. 1760–1762.)

2.1.1 Radial flux motors

Most often used PM motors are axial and radial flux motors. Of these two the radial flux being the most common. Radial flux means that the magnetic flux crosses from the rotor to

stator in radial direction. The rotor can be internal or external, but in this case only internal rotors are investigated. Structure of a radial flux motor varies a lot depending on the magnetization type. The permanent magnets can be surface mounted or interior magnets. Both magnet positioning have their advantages and drawbacks but the surface magnets are significantly more often used option. Figure 3a presents surface mounted radial flux motor and Figure 3b a radial flux motor with interior magnets. These are just two options of several different surface and interior magnet assembling possibilities.

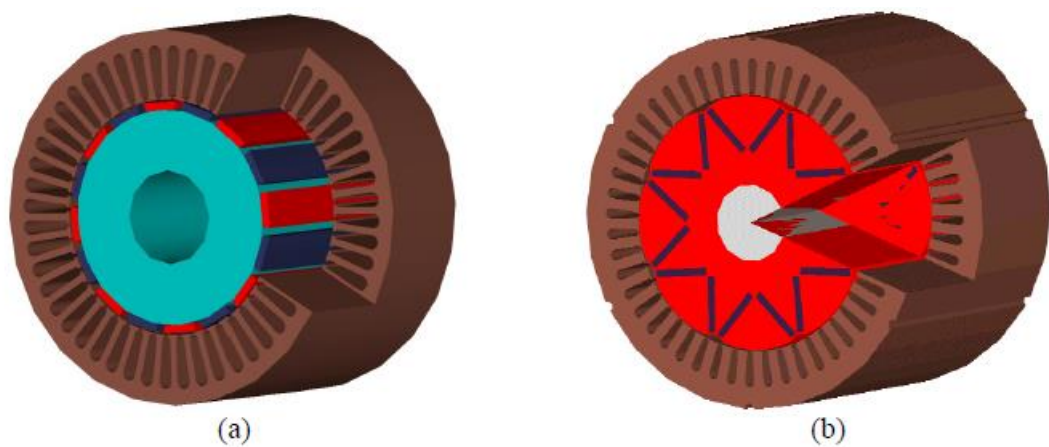


Figure 3. Surface mounted permanent magnets (a) and interior permanent magnets (b) (Modified: Parviainen 2005, p. 24).

The surface mounting structure is easier to manufacture and assemble since the magnets can be often glued on the surface of the rotor. However, the drawback in this method is the high centrifugal forces in high-speed applications breaking easily the glue joint. Reinforcing belts can be used to reduce the centrifugal force, but they also come with drawbacks such as cooling or electrical conduction problems. (Parviainen 2005, p. 24–25.) Surface mounted magnets come in various forms of which radial and breadloaf shapes (Figure 4b–c) are the most convenient ones since they provide uniform air gap and thus uniform flux density (Krishnan 2010, p. 22).

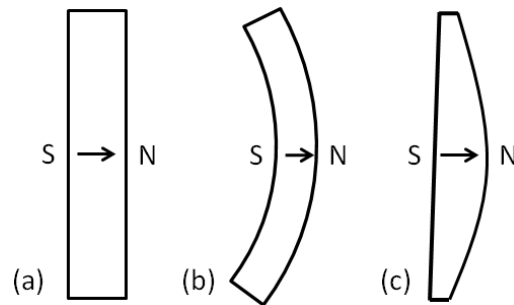


Figure 4. Various types of magnets: (a) rectangular; (b) radial; and (c) breadloaf (Modified: Krishnan 2010, p. 22).

Interior magnet arrangement is more complex to manufacture, but it has some benefits: rectangular shaped magnets (Figure 4a) can be used which are easier to manufacture compared to the breadloaf shaped magnets used in surface mounting. The problematic centrifugal effect in surface magnets is reduced and thus higher rotation speeds are allowed. Internal assembling also protects magnets from mechanical impacts, wear, corrosion and demagnetization. It also reduces unwanted cogging torque and provides almost sinusoidal air-gap flux density waveform. (Parviainen 2005, p. 25.)

Compared to axial flux machines, the radial flux structure is more commonly used option mainly because of the well-established manufacturing process. The manufacturing process of radial flux motors reminds a lot of the same procedure used for induction motors. Components and installation procedure for both motors are basically the same and because induction motors have been dominating the motor types used in industry, the know-how gained from their manufacturing can be used in manufacturing process of radial flux PM motors as well. Axial flux machines are not so commonly used and that is why they have been also manufactured less. This reflects directly to the optimization of design and manufacturing process of the axial flux motors making it more difficult and less cost effective. However, they provide good alternative to radial flux motors especially in directly driven applications where axial length of the motor is limited. (Parviainen 2005, p. 14.)

2.2 New phenomena, requirements and benefits brought by an integrated motor

As discussed before, PM motors come with good efficiency and power density. In addition to these they offer more compact design with less components compared to traditional motor solution. Components, such as gearbox and mechanical drive to the coupling between the induction motor and machine section, can be reduced. When using PM motors also rotor pole windings, slip rings, brushes, excitation power supply and control unit can be eliminated. This means less possible sources for losses and thus better efficiency. Space savings, component reduction and simpler structure leads to significant savings in machine-side footprint and lower life-cycle costs. (Haring et al. 2003, p. 171, 178.) Figure 5 illustrates same pump with traditional (a) and integrated motor (b). Motors are presented in same scale and as it can be seen, the difference in physical size of the assembly is clear: the integrated version requires 48 % less space in horizontal direction. In the figure it can also be seen how the traditional version require two different shafts and a coupling to couple them while the integrated option requires only one shaft and no coupling unit at all.

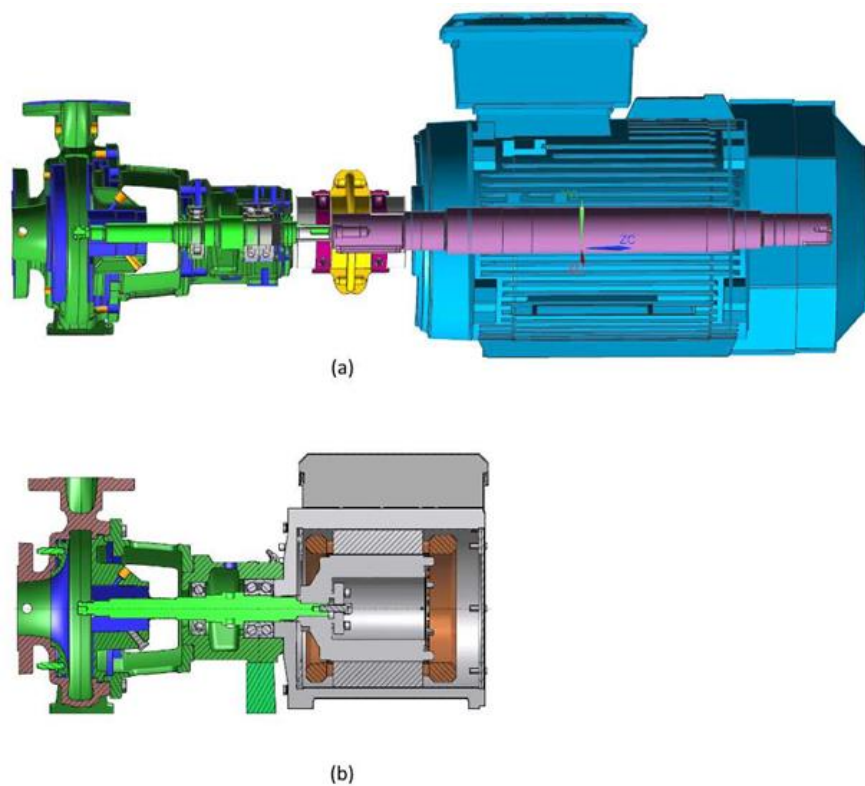


Figure 5. Structural and physical difference between traditional (a) and integrated (b) solution (Tarhonen 2016a).

2.2.1 Bearing and shaft requirements

Because of fewer bearings, the structure is not as well supported as in the traditional motor. The new structure makes the whole rotor-stator package more unstable and thus more prone to vibration. As the rotor movement is less restricted, it leads to variation of air gap between the rotor and stator. This leads to unbalanced magnetic force distribution, which will be discussed later. In order to keep the rotor dynamically and statically balanced the shaft and bearings need to be able to carry the load of the rotor and keep it concentric with respect to stator. This leads to stricter shaft and bearing design requirements, since the normal manufacturing tolerances might not be enough. However, true source of vibration behavior in an assembly including an integrated motor is a combination of mechanical and electrical excitation. The combination of these two vibration sources should be taken into account already during the designing phase to reduce the costly modifications in prototype testing phase.

2.3 Basic concept of vibration

Vibration means repetitive motion of objects with respect to stationary position. In many structures vibration is harmful since it can cause unwanted movement of the structures and eventually cause system failure. Goal in vibration analysis is to try to predict the motion of a vibrating system. (Inman 2001, p. 2.) In integrated motor assemblies the harmful vibration can occur as contact between the rotor and stator. To be able to predict the vibration behavior, basic equations of vibration need to be established.

In an undamped system, if the motion is considered to be linear, the vibrating system can be considered as a simple mass-spring system and expressed as follows:

$$m\ddot{x}(t) = -kx(t), \quad (1)$$

where m is mass, \ddot{x} is acceleration, k is spring constant and x displacement in function of time. (Inman 2001, p. 4.)

Since the motion of vibration is periodic, an equation of motion can be written for the structure as follows:

$$x(t) = A \sin(\omega_n t + \phi), \quad (2)$$

where A is the amplitude of the motion, ω_n is the angular natural frequency which determines the time interval in which the function repeats itself, t is time in seconds and phase angle ϕ is the initial value for the sine function. (Inman 2001, p. 5.)

Every object and structure has its own natural frequency, which tells the frequency in which the structure starts to oscillate. A natural frequency can be calculated with the help of equations 1 and 2. By differentiating the equation of motion twice, it is possible to solve the acceleration of the vibrating object (Inman 2001, p. 5):

$$\ddot{x}(t) = -\omega_n^2 A \sin(\omega_n t + \phi) \quad (3)$$

By substituting equation 3 to equation 1 and reducing the common terms it is possible to determine the natural frequency of a system (Inman 2001, p. 6):

$$-m\omega_n^2 A \sin(\omega_n t + \phi) = -kA \sin(\omega_n t + \phi) \quad (4)$$

$$\omega_n = \sqrt{\frac{k}{m}} \quad (5)$$

If a periodic external force is introduced to the system with a certain frequency, and if that frequency matches system's natural frequency, it will cause resonance. Resonance will cause large deflections to the system which might lead to system failure. (Inman 2001, p. 89.) This kind of external periodic force comes from a rotating part such as a pump impeller or a rotor of an electric motor. If the excitation force is harmonic, it has the form of sine or cosine and can be written as function of single frequency:

$$F(t) = F_0 \cos \omega t, \quad (6)$$

where F_0 is magnitude of applied force and ω is the frequency of the applied force. (Inman 2001, p. 90.) The forced response equation must satisfy equation 1. It is also convenient to divide the equation by m , which leads it into following form:

$$m\ddot{x}(t) + kx(t) = F_0 \cos \omega t, \quad (7)$$

$$\ddot{x}(t) + \omega_n^2 x(t) = f_0 \cos \omega t, \quad (8)$$

where f_0 is the externally applied force (F_0) divided by mass (m). (Inman 2001, p. 91.) A particular solution for the equation 8 can be found by assuming it has the same function as the forcing function:

$$x_p = X \cos \omega t, \quad (9)$$

where X is the amplitude of the forced response. By placing the particular solution to equation 8, it can be written as follows (Inman 2001, p. 91.):

$$-\omega^2 X \cos \omega t + \omega_n^2 X \cos \omega t = f_0 \cos \omega t, \quad (10)$$

From equation 10, X can be solved and thus express the particular solution as follows (Inman 2001, p. 92):

$$x_p(t) = \frac{f_0}{\omega_n^2 - \omega^2} \cos \omega t \quad (11)$$

Since the described system is linear, the particular solution is only half of the complete solution. Also a homogenous part needs to be taken into account by considering equation 2. With some trigonometric manipulation the total solution for the response of an undamped system can be expressed as follows:

$$x(t) = A_1 \sin \omega_n t + A_2 \cos \omega_n t + \frac{f_0}{\omega_n^2 - \omega^2} \cos \omega t, \quad (12)$$

where A_1 and A_2 are determined by initial conditions. (Inman 2001, p. 92.) Presented model is applicable for linear undamped system. If the system frequency corresponds the system natural frequency ($\omega = \omega_n$), the system will be in resonance and amplitude of the vibration $x(t)$ will increase boundlessly as Figure 6 depicts (Inman 2001, p. 96). In case of electric motor this means eventually that the rotor (rotating component) makes contact with the stator (stationary component). In real situation material, connections and structures are elastic adding damping to the system.

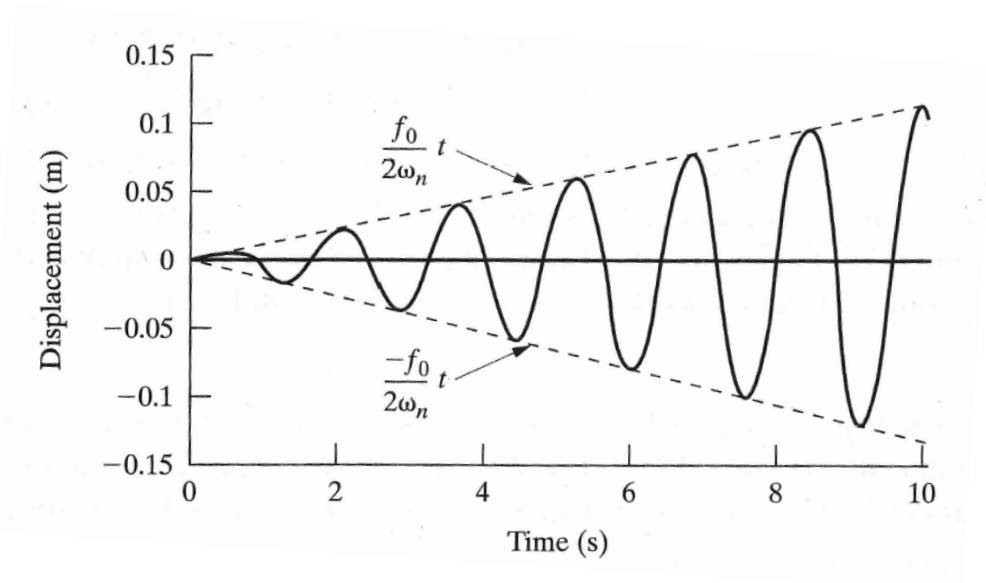


Figure 6. Forced response of a spring-mass system driven harmonically at its natural frequency (Inman 2001, p. 96).

2.4 General sources of vibration

The forced vibration can develop from several different sources. In PSK standard 5707 (2011) vibration measuring in condition monitoring of rotating machinery have been investigated. The standard divides different vibration sources into several categories, which are presented in table 2. Some vibration sources such as gears, sliding bearings and belt drives are neglected from the table since they are not relevant in this work. In the table n presents rotating speed of the machine.

Table 2. Vibration sources according to standard PSK 5707 (PSK 5707 2011, p. 8–22, 28–32).

Vibration source	Main occurrence frequency	Main direction
Unbalance		
static		Radial
couple	1xn	Radial/Axial
dynamic		Radial/Axial
overhung rotor		Radial/Axial
Eccentricity	1xn ₁ , 1xn ₂	Radial
Bent shaft	1xn, 2xn	Radial, Axial
Shaft misalignment		
angular	1xn, 2xn, 3xn	Axial (angular misalignment)
radial	1xn, 2xn	Radial (radial misalignment)
Mechanical looseness	0.5xn, 1xn, 1.5xn... Nxn	Direction of the looseness
Incorrect machine mounting	1xn	
Rolling Bearings		
Metal contact	1xn, 2xn, 3xn (high frequencies)	Radial
Component fault	n +/- passing frequency	Radial
Race wear	n + Ball pass frequency	Radial
Cocked bearing	1xn, 2xn, 3xn	Axial
Rotor rub	0.5xn, 1xn, 2xn... Nxn	Radial
Rotor crack	1xn, 2xn, 3xn	Radial
Hydraulic and aerodynamic disturbances	1xn, 2xn, blade pass frequency (and its harmonics)	Random

Table 2 continues. *Vibration sources according to standard PSK 5707 (PSK 5707 2011, p. 8–22, 28–32).*

Vibration source	Main occurrence frequency	Main direction
Faults in electric motors		
Electromagnetic attractive force	2 x line frequency (inevitable)	Radial and axial in all cases
Air gap eccentricity	1xn, 2xn, 2 x line frequency	
Local heating	2 x line frequency	
Rotor faults	Nxn +/- harmonics	
Loose connections	1 x line frequency	
Loose stator windings	2 x line frequency, slot passing frequency	

Even though all the vibration sources presented in table 2 should be investigated, in order to keep this work compact, only part of the vibration sources are discussed more thoroughly. Some early measurements done in Sulzer Pumps Finland have been showing harmful vibration behavior especially on the twice-rotation speed area (Tarhonen 2016b). This limits the possibilities to bent and misaligned shaft, mechanical looseness, bearing defects, rotor rub, rotor crack, hydraulic and aerodynamic disturbances and air gap eccentricity between the rotor and stator. Rotor crack has usually increasing effect on the fault and because measurements have shown immediate oscillation the possibility of crack can be ignored. Rotor rub is usually consequence from improper assembly of components or misalignment which results in this case as uneven air gap between the rotor and stator. Also the hydraulic and aerodynamic disturbances are neglected since the measurements are performed without any fluid or an impeller. This leaves five possible sources of vibration:

1. Bent shaft
2. Misaligned shaft
3. Mechanical looseness
4. Bearing defects
5. Air gap eccentricity

Shaft, looseness and bearing induced vibrations are purely mechanical. Air gap eccentricity is due to assembling defects and manufacturing tolerances of rotor and stator. In electric

motors there also occurs an electromagnetic force in the air gap, which needs to be taken into account.

2.5 Electromagnetic sources of vibration

In an ideal situation the rotor and stator are perfectly concentric with respect to each other's. In this case radial forces would cancel each other out. However, due to manufacturing tolerances and imperfections there is always eccentricity and runout included. In addition to this the motor assembling has its own tolerances causing irregular air gap between the rotor and stator.

2.5.1 Radial excitation

Irregular air gap between rotor and stator appears as eccentric movement. There occur two types of eccentric movement of the rotor: cylindrical whirling motion and symmetric conical whirling motion. According to Tenhunen et al. (2003, p. 563) "The cylindrical whirling motion of the rotor means that the rotor remains aligned with the stator but the geometrical centerline of the rotor travels around the geometrical centerline of the stator in a circular orbit with a certain frequency known as a whirling frequency, and with a certain radius, known as the whirling radius." In symmetric conical whirling motion the whirling frequency stays constant, but the whirling radius in both ends is equal in size but in opposite direction. These two whirling modes can also combine during the rotation. Figure 7 illustrates all three cases. (Tenhunen et al. 2003, p. 563.)

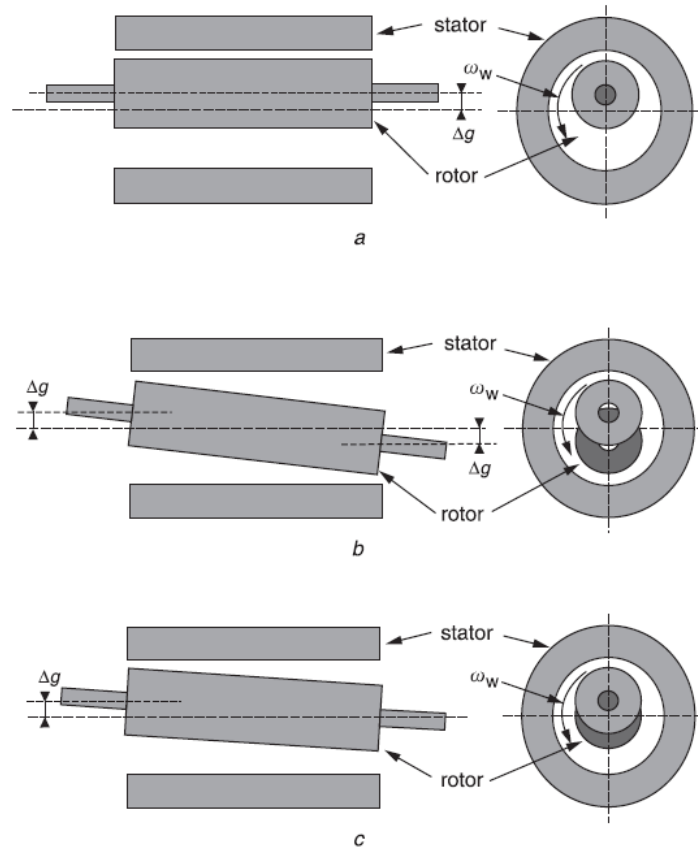


Figure 7. Different types of whirling rotor: Cylindrical whirling motion (a), symmetrical conical whirling motion (b) and combination of the two whirling motions (c). In the figure ω_w is whirling direction and Δg whirling radius of the rotor. (Tenhunen et al. 2003, p. 563.)

Eccentric rotor creates an asymmetric magnetic flux distribution that causes radial forces. This phenomenon is known as unbalanced magnetic pull. (Arkkio et al. 2000, p. 354–358). Arkkio et al. (2000) have been researching the effect of unbalanced magnetic pull in induction machines and discussed about analytical model developed to estimate radial force with respect to eccentricity. In their research they found out that the radial force increases linearly with respect to whirling radius as Figure 8 depicts. Lines in the figure present calculated results and symbols measured results with different supply voltage: 150, 200 and 250 V. From these results it can be said that radial force increases as the exciting voltage increases. Also Zhu and Li (2015, p. 4931) found out how winding current increases the radial force in bearingless PM motors (Figure 9). Kim, Hwang & Park (2000, p. 1350) have been also researching mechanical and magnetic coupling through air gap on a rotor-bearing system and found out similar kind of results as Arkkio et al. (2000, p. 354–

358): magnetic forces in air gap are linear with respect to air gap length and magnetic forces have influence on the vibration behavior of the rotor bearing system.

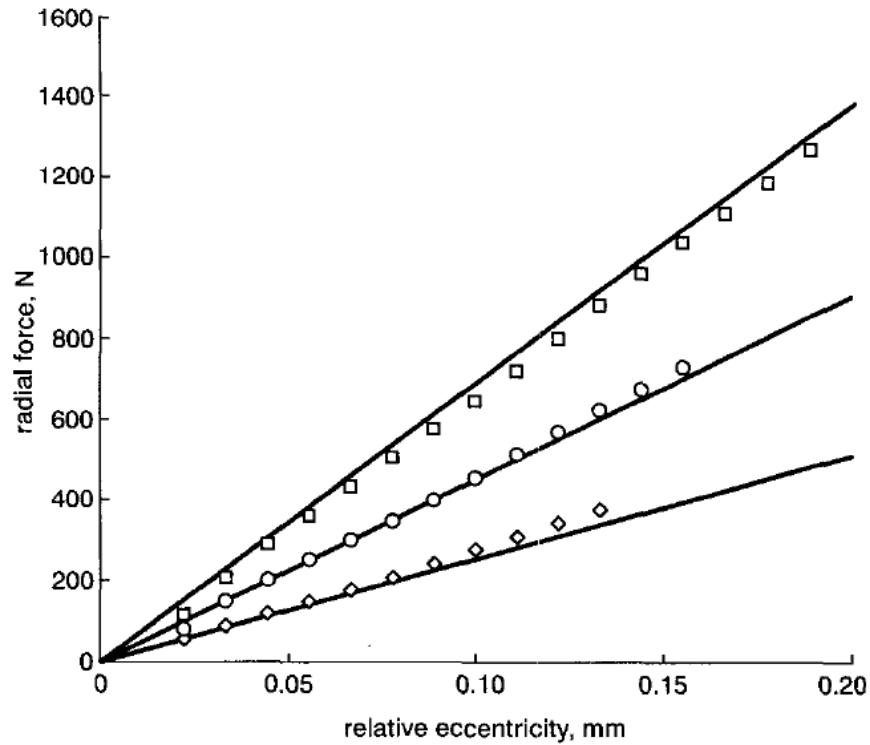


Figure 8. Effect of eccentricity on radial force between rotor and stator in cage induction motor (Arkkio et al. 2000, p. 358).

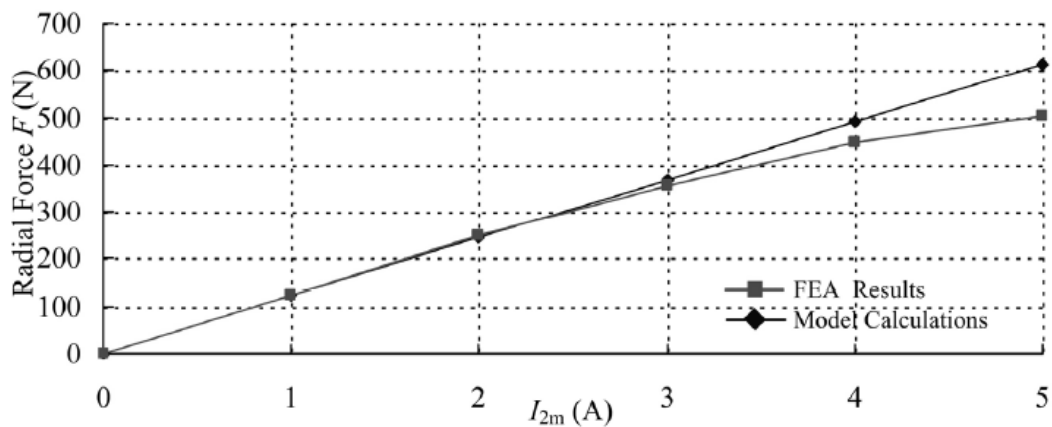


Figure 9. Effect of winding current on radial force between rotor and stator in bearingless PM motor (Zhu & Li 2015, p. 4931).

The magnetic field occurring between the rotor and stator can be described with magnetic flux density B and magnetic field intensity H . Flux density can be thought as the density of

magnetic field flowing through material and field intensity as resulting change in the intensity of magnetic field. For many materials relation of B and H is linear, and can be written as follows (Hanselman 2006, p. 16):

$$B = \mu H , \quad (13)$$

where μ is the permeability of a specific material. It tells the degree of magnetization that the material obtains when a magnetic field is applied.

In order to present magnetic stresses, forces and torque between two objects, a theory called Maxwell's Stress Tensor can be used. According to Maxwell's stress theory, the magnetic field strength between objects in a vacuum creates a stress σ_F on the object surface as follows (Pyrhönen, Jokinen & Hrabovcova 2007, p. 33):

$$\sigma_F = \frac{1}{2} \mu_0 H^2 , \quad (14)$$

where μ_0 is the permeability in vacuum. Normal force (F_{Fn}) acting between the two surfaces can be approximated as follows (Pyrhönen, Jokinen & Hrabovcova 2007, p. 36):

$$F_{Fn} = S \sigma_{Fn} , \quad (15)$$

where σ_{Fn} is normal component of the Maxwell's stress tensor and S is specific area of the air gap. When flux density presented in equation 13 and Maxwell's stress tensor are applied to the equation of normal force, it can be written in the following form (Pyrhönen, Jokinen & Hrabovcova 2007, p. 36):

$$F_{Fn} = \frac{B^2 S}{2\mu_0} \quad (16)$$

Noticeable is that equation 16 gives just a rough estimation of the radial force between the rotor and stator. More sophisticated models have been also investigated for example by Anwar & Husain (2000, p. 1595–1596).

Static eccentricity of the rotor causes static radial forces ($F_{m\ stat}$), since the air gap stays constant during one rotation. Dynamic eccentricity on the other hand causes dynamic radial forces ($F_{m\ dyn}$) since the air gap is constantly varying during one rotation. The dynamic force also rotates along rotor. Figure 10 illustrates static and dynamic loads.

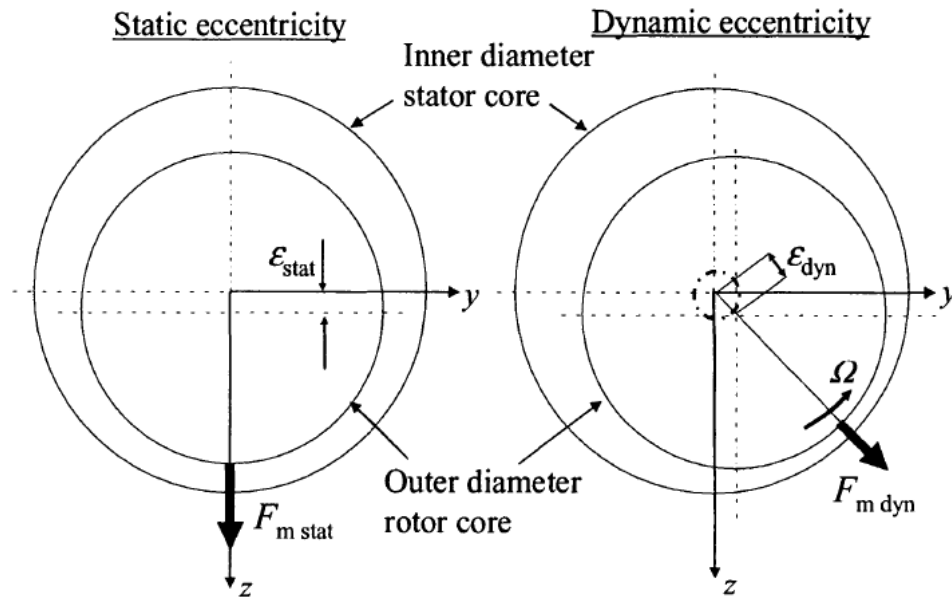


Figure 10. Static (ϵ_{stat}) and dynamic (ϵ_{dyn}) eccentricity (Werner & Binder 2005, p. 1).

In the Figure 10, $F_{m\ stat}$ and $F_{m\ dyn}$ are in direction of the affecting magnetic force. As the force increases on one side of rotor to the direction of $F_{m\ stat}$ or $F_{m\ dyn}$, it reduces at the same time on the other side since the force is directly related to air gap length as it was stated before. (Werner & Binder 2005, p. 1.)

Dynamic eccentricity of the rotor causes dynamically changing magnetic flux density which makes the radial force vary during one rotation of the rotor. Figure 11 presents relative radial force with 89 % displaced air gap length during one rotation. (Chin et al. 2009, p. 3.)

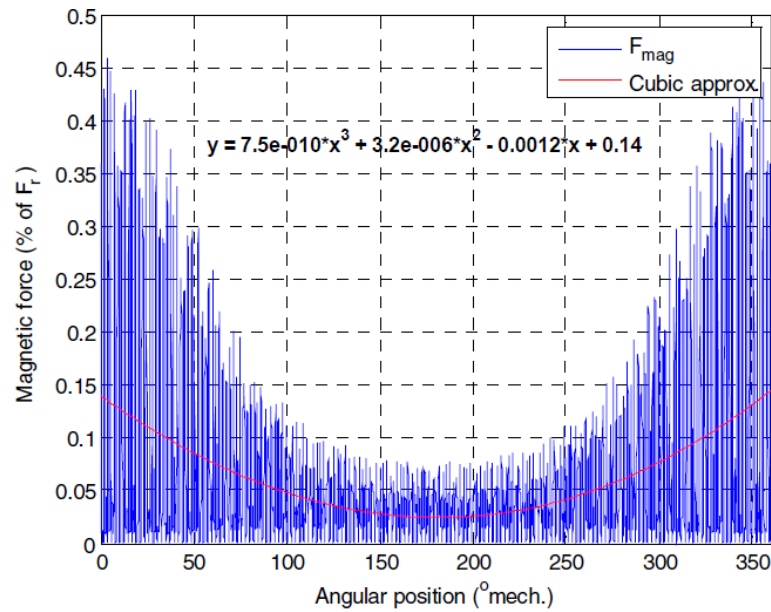


Figure 11. Radial force distribution during one rotation with 89 % eccentricity (Chin et al. 2009, p. 4).

Chen, Yuan & Peng (2015, p. 548) have been also investigating the effect of variable magnetic flux density to system behavior. In the research they discovered how variable flux density and relative eccentricity between rotor and stator decreased the natural frequency of a rotor system as Figure 12 depicts.

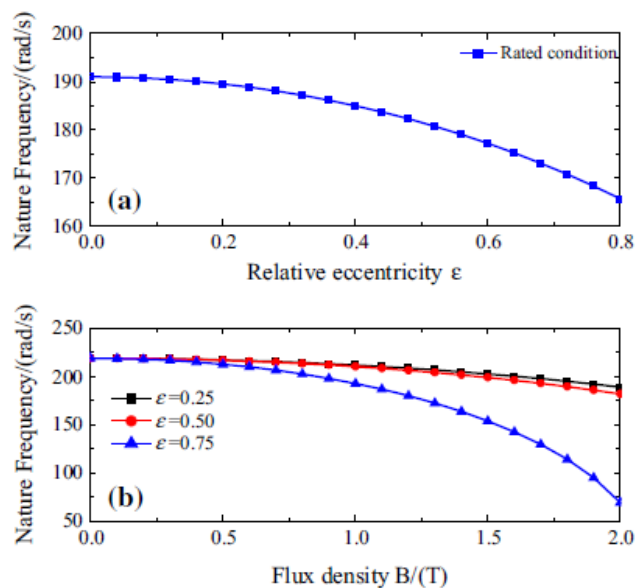


Figure 12. Variation of natural frequency (Chen, Yuan & Peng 2015, p. 548).

As the rotor can be placed eccentric to the stator, also stator can be installed eccentrically with respect to rotor. There might occur also imperfections during the stator manufacturing causing elliptic form of the stator cross section. Stator asymmetries may cause non-uniform magnetic field distribution in stator core and introduce high localized magnetic saturation. (Zhu et al. 2008, p. 3851.) This leads to asymmetric force distribution between rotor and stator. If the rotor rotates around its own centerline which is not aligned with stator centerline, it causes constant static force where air gap is narrowest. Figure 13 illustrates situation where static electromagnetic force develops due to elliptic stator. In this situation rotor rotates centrally around its own centerline.

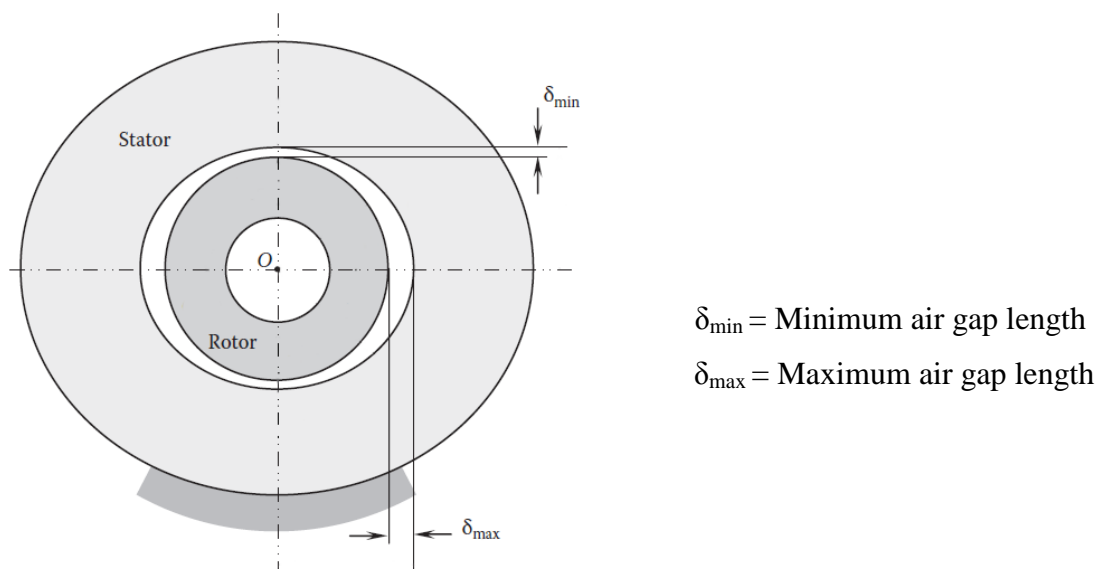


Figure 13. Asymmetric force distribution due to elliptic stator (modified: Tong 2014, p. 505).

Certain amount of tolerance is also allowed in installation. In pump assemblies pump is connected to motor via bearing housing. In case of interior rotor PM motors the motor frame is connected to the bearing housing. Because stator is attached to frame, it will be misaligned if the motor frame is not properly connected or tolerance limit is set big. Possible case is angular (Figure 14a) or radial (Figure 14b) misalignment due to improper fastening of the bolts or eccentric connection face (Tarhonen 2016b).

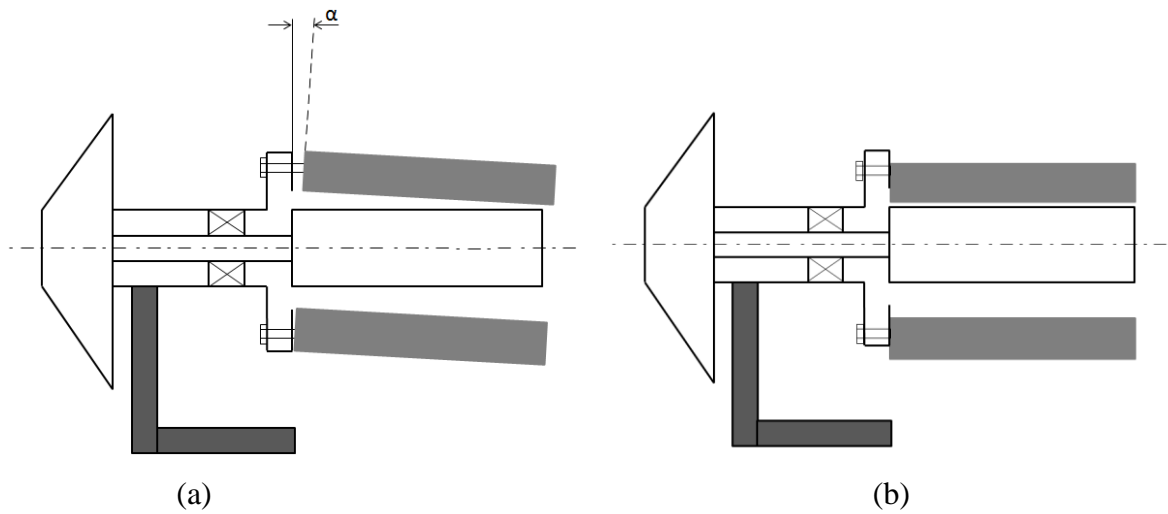


Figure 14. Stator angular (a) and vertical (b) misalignment. Stator angular misalignment is presented with symbol α .

In order to reduce the vibration behavior due to asymmetric magnetic field, the uneven radial forces should be reduced or balanced. For reduction of radial forces, Islam's research state that with modification of the following features the radial forces can be reduced (Islam 2009, p. 48):

- Increasing air gap
- Reducing magnet strength
- Improving shaft alignment or rotor eccentricity
- Use of balanced winding
- Increasing resonant frequency by changing lamination dimensions

Air gap increase or magnet strength reduce are not recommended options, since they also reduce the effective torque of the machine. Winding balancing and lamination dimension variation are related to more profound electric motor design, which is not discussed in this research. The shaft alignment and rotor eccentricity however can be influenced with proper manufacturing of components and careful assembling. (Islam 2009, p. 48.)

2.5.2 Tangential excitation

In addition to the radially affecting electromagnetic forces, there is also present force fluctuation in tangential direction. As the permanent magnet rotor spins, it is constantly trying to align the magnets with the stator poles. As the physical distance between the

magnet and stator pole decreases, the aligning force increases. When rotor spins, it successively passes stator teeth and open slots. This causes periodically changing magnetic field. Every time the magnet passes a stator tooth and moves towards a slot, the magnetic force tries to pull the magnet back to tooth direction or towards the next tooth causing force component in tangential direction. This effect is called cogging torque, which is highly undesirable especially in low speed applications. (Tong 2014, p. 8.) Cogging torque can be influenced with several design parameters of which one often used is skewing of magnets or stator slots (Islam et al. 2012, p. 4–5). In addition to Islam’s research cogging torque has been investigated a lot by other researcher as well. For example Srisiriwanna & Konghirun (2012, p. 4) have found out that the most effective method to reduce cogging torque is to decrease the width of stator slot opening. They have also stated how the increase of air gap length or reduction of magnet flux density can reduce the cogging torque, but at the same time they reduce the performance of the motor. Puranen (2006, p. 24) has stated in his doctoral dissertation how ”Chamfering of the magnets, however, is a very effective and common method to decrease the cogging torque. Magnets with chamfered edges will produce a more sinusoidal air gap flux density distribution.” However, cogging torque excitation frequency is considered to be very high compared to radial excitations and thus excluded from the scope of this work.

2.6 Mechanical sources of vibration

The main sources of vibration in rotor-bearing systems are bearing faults and shaft misalignment. Usually shaft misalignment is caused by non-collinear coupling of the electric motor shaft and driven machine shaft. In this case when the pump and motor are placed on the same shaft there is no problem with the coupling. However, other problems may occur due to bearing unit installation process or used components, such as:

- Manufacturing error in rolling elements
- Horizontal rotor and bent shaft
- Clearance between the inner or outer ring of the bearing
- Asymmetric bearing housing

All the rolling elements have manufacturing errors in their dimension, which are taken into account by allowing certain tolerance for them. However, these tolerances allow new sources of vibration to arise. For example in rotor-bearing system with double row ball

bearing there are two common types of resonance sources: Shaft eccentricity and directional difference in stiffness. Shaft eccentricity is result of irregular ball size making the shaft deviate from the bearing centerline. Figure 15a illustrates angular misalignment in the shaft. If one of the balls is bigger compared to the others (Figure 15b), it might cause a shrink fit between the bearing inner and outer ring causing difference in directional stiffness which then rotates at certain angular velocity. (Yamamoto & Ishida 2001, p. 183–184.) In rotor-bearing systems misalignment and tightness causes usually excitations in the range between two and three multiples of running speed (Taplak, Erkaya & Uzmay 2013, p. 341).

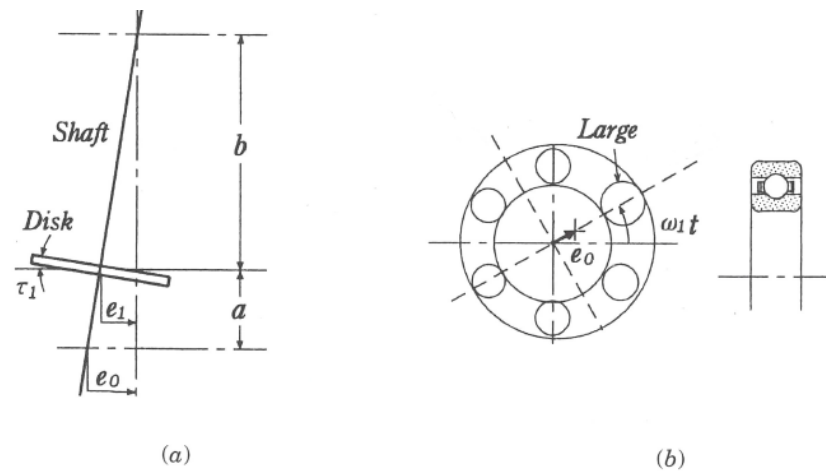


Figure 15. Misaligned shaft due to bearing faults (modified: Yamamoto & Ishida 2001, p. 183).

If the rotor is placed horizontally, which it usually is in electric motors, the load of the shaft and rotor is placed on the bearing balls which makes them deform. Size and number of the balls have effect on the deformation, but even the bearing would be manufactured without any errors there would still be resonance. This happens because gravitational force vector is pointing downwards and each ball passes it at certain frequency. The shaft itself can also be initially bent due to misaligned bearings or manufacturing error. (Yamamoto & Ishida 2001, p. 185–186.) All the shafts are measured in case of bending, but again tolerances allow difference in eccentricity between the shaft end and bearing installation point.

When a bearing is installed on the shaft, it might be left loose. This causes resonance on two different levels, one on the nominal speed of the shaft and other one on the speed at which the inner race of the bearing is turning, which is usually lower than the nominal speed. The bearing might as well be loose in the bearing housing causing resonance in the fourth harmonic of the rotor speed. Excessive clearance between shaft and bearing inner ring can be detected during the installation and excessive clearance in the bearing housing can be pointed out with vibration measurements. (Taylor 1994, p. 125–126.) Tiwari, Gupta & Prakash (2000, p. 775) have been investigating the effect of radial internal clearance in rotor-bearing system supported with ball bearings. They found out that increase in internal radial clearance increases non-linearity in the system, especially in the twice-rotation (2X) excitation frequency area. They compared two different types of SKF deep groove single row ball bearings with radial clearances of 2.5 μm and 20 μm . Figure 16 shows frequency response plots from the measurements. According to the results the bigger the clearance is, the bigger the vibration amplitude is.

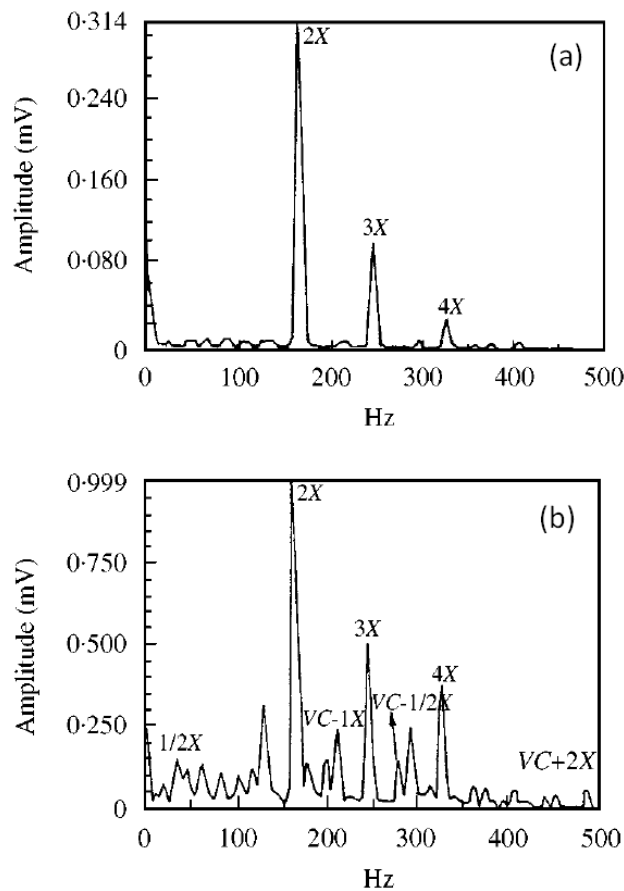


Figure 16. Vibration levels in vertical direction with 2.5 μm (a) and 20 μm (b) internal radial clearances (modified: Tiwari, Gupta & Prakash 2000, p. 778).

All the bearing housings are measured in case of eccentricity, but there is always some tolerance allowed which causes static eccentricity inside the electric motor. When all the allowed tolerances are taken into account, together they can lead to harmful deviation especially in rotor-bearing systems where the rotor structure is not supported from the other end. Figure 17 presents this kind of overhang structure in which the rotor is not supported in the motor rear side. Additional mass from the rotor together with big lever causes bending in the shaft. Together with combination of manufacturing tolerances of the parts it might lead to considerable narrowing of the air gap length between the rotor and stator. As it was stated before, the air gap length is directly proportional to the electromagnetic forces causing unbalanced magnetic pull.

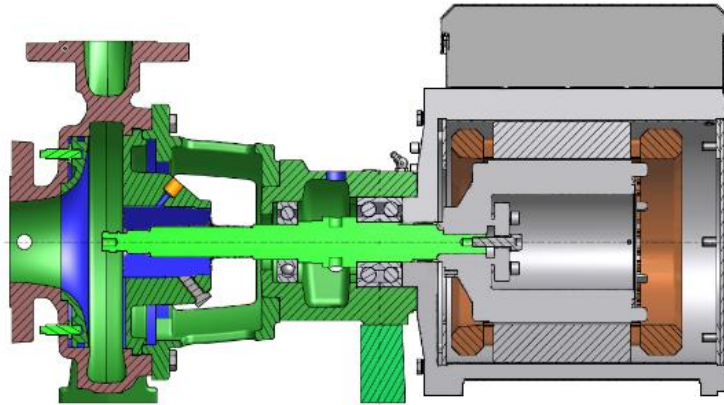


Figure 17. Overhang rotor structure (Tarhonen 2016a).

2.6.1 Gyroscopic effect

In the rotating machinery unequal distribution of mass in axial direction causes gyroscopic moment to the system. It is defined as rate of change of angular momentum. Especially in overhung type rotor bearing systems, like in Figure 17, gyroscopic effect needs to be taken into account when determining critical speeds of the system. Gyroscopic moment is defined as follows:

$$M_G = J_p \Omega \dot{\theta}, \quad (17)$$

where J_p is polar mass moment of inertia of the rotor, Ω is the angular velocity of the rotor and $\dot{\theta}$ is the angular velocity of change of orientation of the rotating axis (Sopanen 2015).

The gyroscopic moment affects the natural frequencies in such a way that they either increase or decrease as the rotation speed increases. Increasing natural frequencies are called forward whirling modes and they rotate in the same direction as the rotor. Decreasing natural frequencies are called backward whirling modes and they rotate into opposite direction with respect to the rotation direction of the rotor (Sopanen 2015).

Jahromi, Bhat & Xie (2015, p. 879–887) have been investigating gyroscopic effect in a simple Jeffcott rotor with bearings in the both ends and a disk located in the middle of the shaft. They created an analytical and FEM model for the system and verified the results with experimental test. Figure 18 illustrates a Campbell diagram based on the FEM model, which tells the critical frequencies of the system as function of rotating speed.

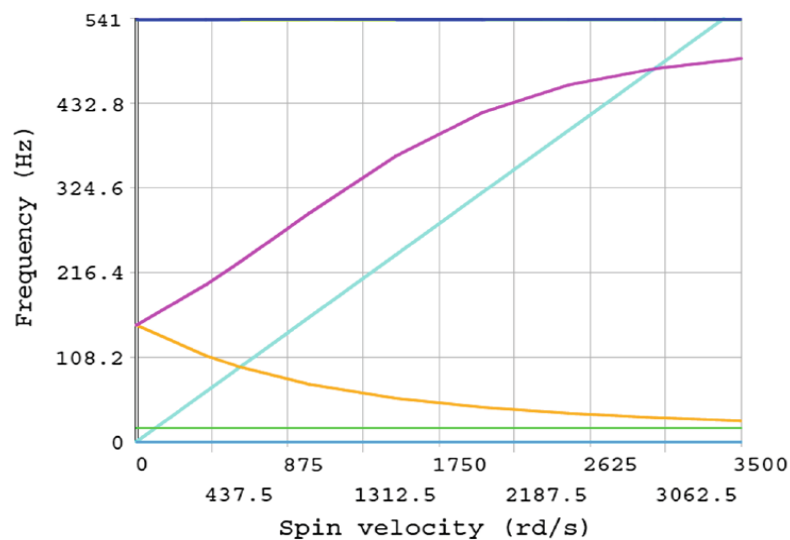


Figure 18. Representation of backward whirling mode (non-linearly decreasing line) and forward whirling mode (non-linearly increasing line). Linearly growing line represents the rotating speed of the shaft. (Jahromi, Bhat & Xie 2015, p. 885.)

From this diagram it is possible to see the effect of gyroscopic moment. Because of the system structure, the gyroscopic effect does not affect the first mode at 17.16 Hz but in the second mode the natural frequency separates into two branches: forward and backward. Critical speed for the forward mode is 458.4 Hz and for backward mode 97.2 Hz. (Jahromi, Bhat & Xie 2015, p. 884.) The figure illustrates that the gyroscopic effect should be taken into account when designing rotating machines especially with overhung- type structure, since it has a clear influence on the resonance area.

3 MODELING AND VERIFICATION OF EXCITATIONS

Simulation can be used as a tool to improve efficiency of the whole product development process. It can provide big advantages on virtual testing and optimization of the systems especially in cases where different customers have different kind of needs. With simulation, costly prototypes and long iteration processes can be reduced making the whole product development process more cost-efficient.

The magnetic pull caused by electromagnetic forces is possible to simulate by introducing “magnetic spring” with a negative spring constant between the rotor and stator. (Werner & binder 2005, p. 1.) According to Werner & Binder (2005, p. 1) the magnetic spring depends on following parameters:

- “Amplitude of the air gap induction
- Inner diameter of the stator core
- Stack length of the stator core
- Air gap width
- Opening of the slots
- Saturation of iron parts
- Damping of the eccentric magnetic field”

In this section a simulation model of the centrifugal pump with an integrated permanent magnet motor is created. The geometry is constructed from already existing components to correspond the actual prototype and electromagnetic force is introduced as springs with negative spring constant. Pre-processing is performed in order to simplify the model for the solver after which modal and harmonic analyses are performed. In post-processing phase the simulation results are presented. Goal is to achieve a model which is reliable to use in simulation of a centrifugal pump with a permanent magnet motor.

Geometry of the system was constructed with Siemens NX 8.5 3D-modeling software from which the model was exported to ANSYS Workbench 16.2. Preprocessing was performed with ANSYS DesignModeler 16.2. Meshing and post-processing was performed with

ANSYS Mechanical 16.2. The model was solved with remote solver using ANSYS Mechanical Enterprise Solver license. During the solution eight cores were utilized.

3.1 Geometry

After the model was imported to ANSYS Workbench the geometry needed to be simplified in order to receive a mesh with good quality. Pre-processing was performed with ANSYS Design modeler. In the pre-processing phase, excessive parts and surface features which are not relevant for an accurate model were removed. For example connection box for the electrical connections was deleted and later on pictured as a point mass attached to the system. Also all the bolts and washers were removed and later on taken into account when setting connections between different parts. Also most of the edge blends, chamfers and holes created in the 3D modeling phase were deleted in order to improve the mesh continuity. The pre-processing was mainly performed for the PM motor since it is the most complicated part of the structure and also the most interesting part in this research. Figure 19 presents the model before (a) and after (b) pre-processing.

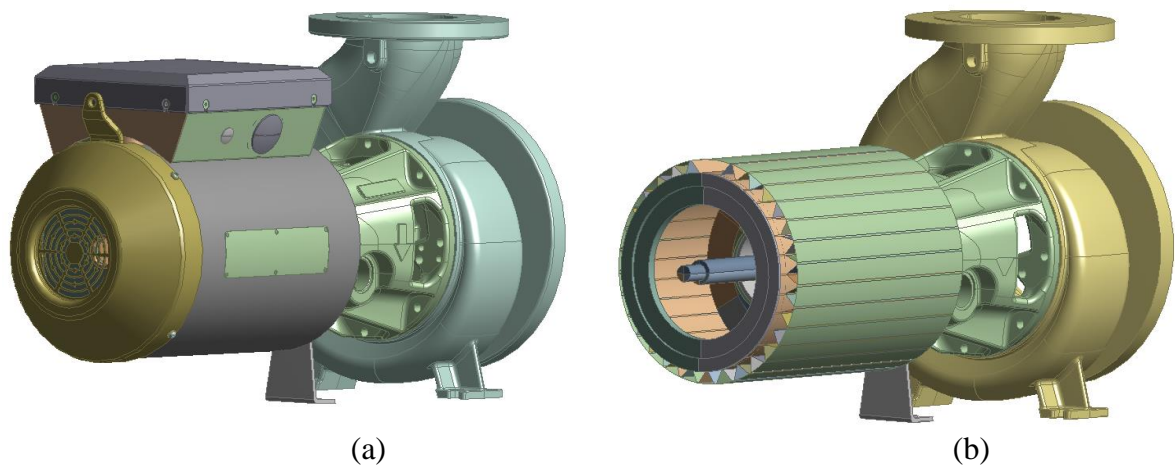


Figure 19. Simulation model before (a) and after (b) pre-processing.

The casing structure was modified very little since it provided already smooth large surfaces without any accurate sections. Also the casing itself was not so relevant part for the investigation. In the bearing unit all the edge blends, surface marks, sealing components and bearing unit casing cover were removed. Also the bearings were removed and later on modeled as general joints. Figure 20 presents the bearing unit before (a) and after (b) pre-processing.

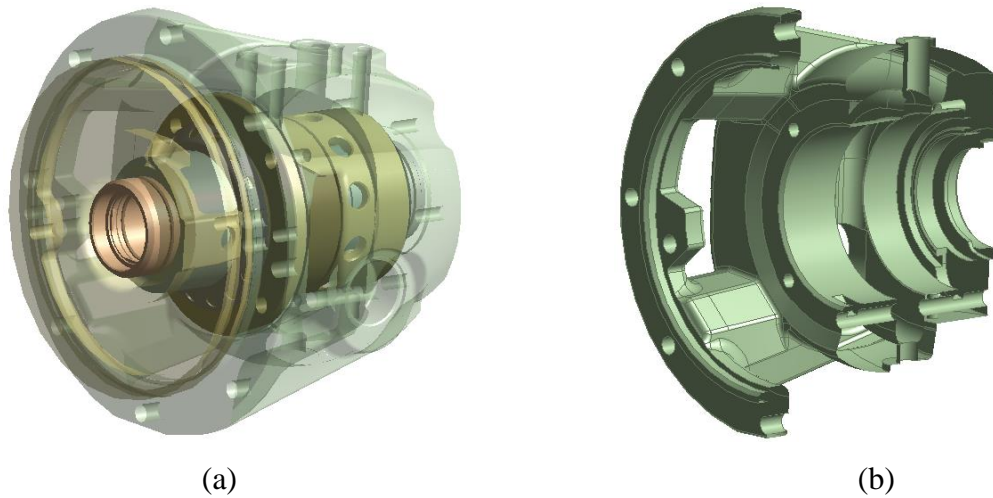


Figure 20. Bearing unit before (a) and after (b) pre-processing.

In the shaft edge blends and retaining ring grooves were removed. The ball bearing contact line was imprinted from the bearing to the shaft surface for both bearings. After this 10 mm wide area was created around the bearing contact line to represent the bearing contact area (Figure 21). Taper bushing connection bolts were removed as well.

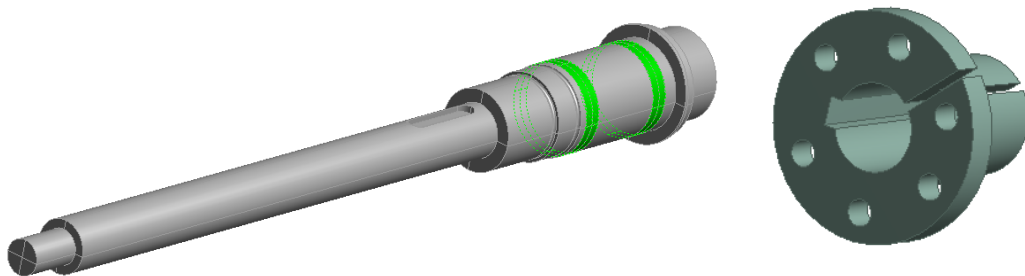


Figure 21. Shaft and taper bushing after pre-processing. Ball bearing contact areas are highlighted as green.

The permanent magnet motor was modified the most because of its complex structure. The connection box and rear cover were replaced with point mass since they were not found to have large effect on the system stiffness. Shield plate was removed because of its small mass and minor effect on the system stiffness. The motor frame and cooling plate were modeled as a mid-surface structure as Figure 22 presents. The mid-surface structure enables the use of shell elements in the meshing phase.

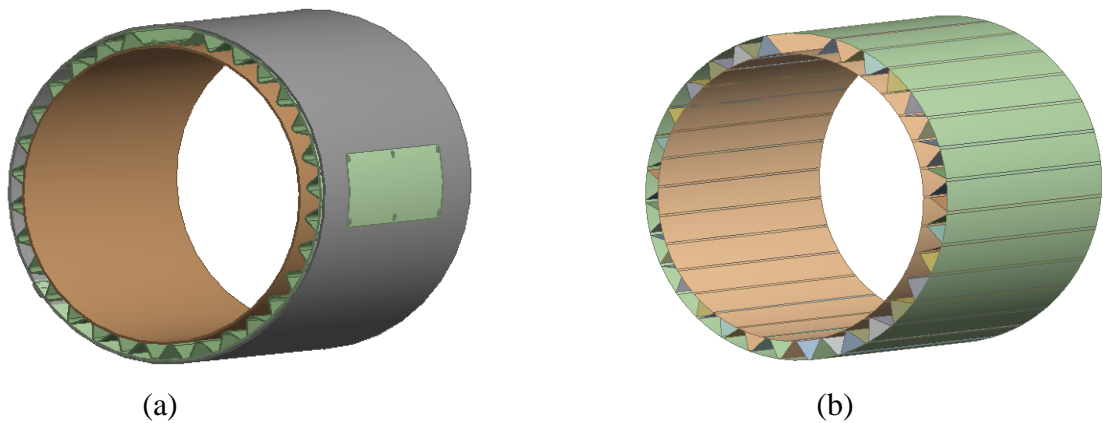


Figure 22. Original (a) and mid-surface structure (b) of the motor frame.

According to the PM motor manufacturer, simple structure of the motor is sufficient for vibration analysis purposes. In the real structure rotor consist of several 2 mm plates which are glued together through magnet holes. According to the manufacturer, the rotor can be modeled as a uniform part and the magnets can be neglected without losing much accuracy. Stator consists of several 0.35 mm plates which are glued together, but it can be as well modeled as a uniform structure. Also stator windings are neglected. In order to model the motor more accurately, permanent magnets and stator windings should be taken into account because of their mass, which again affects to natural frequencies. As the electromagnetic force was modeled using springs, the rotor and stator needed to be divided into equally distributed segments in order to find connection points for the springs. Figure 23 shows the segmented rotor (a) and stator (b).

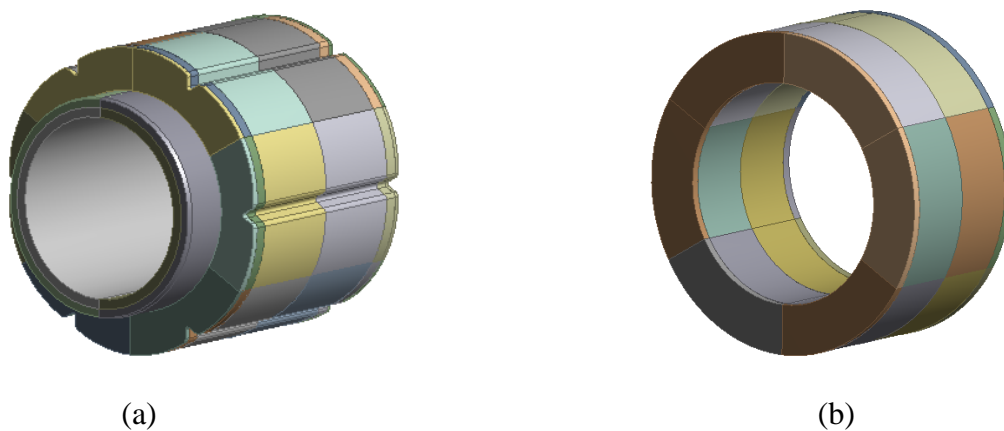


Figure 23. Rotor (a) and stator (b) were divided into segments in order to find equally distributed connection points for the springs.

3.2 Material properties

All components were modeled with linear material properties. Material properties for different components are presented in table 3. For electric motor components the manufacturer suggested to use structural steel even though the motor consist of several different materials. Since some of the motor components are neglected (i.e. stator winding and rotor magnets) in the simulation model, by using structural steel's density the mass of the components corresponds the one with all the specific components and materials.

Table 3. Material properties of the simulation model. Temperature is assumed to be 20 °C.

Component	Material	Specified marking	Standard	Density [kg/m³]	Young's modulus [MPa]	Poisson's ratio
Volute case	Duplex steel	A890 3A	ASTM A890	7680	$2.2 \cdot 10^5$	0.3
Bearing housing	Grey cast iron	A48 CL 35 B	ASTM A48	7200	$1.69 \cdot 10^5$	0.28
Shaft	Duplex steel	SS 2324	SS142324	7800	$2 \cdot 10^5$	0.3
Support foot	Structural Steel	S235JRG2	EN10025	7850	$2 \cdot 10^5$	0.3
Motor carrier	Structural Steel	S355J2G3	EN10025	7850	$2 \cdot 10^5$	0.3
Electric Motor components: - casing - rotor - stator - taper bushing - front plate - rear plate	Structural steel	Ansys material library		7850	$2 \cdot 10^5$	0.3

3.3 Finite Element Mesh

Solid and shell elements were used in creating the finite element mesh. Mesh for the complete model consists of 350553 nodes and 184770 elements. Figure 24 presents the meshed structure. More specific meshing details for different components are presented in table 4.

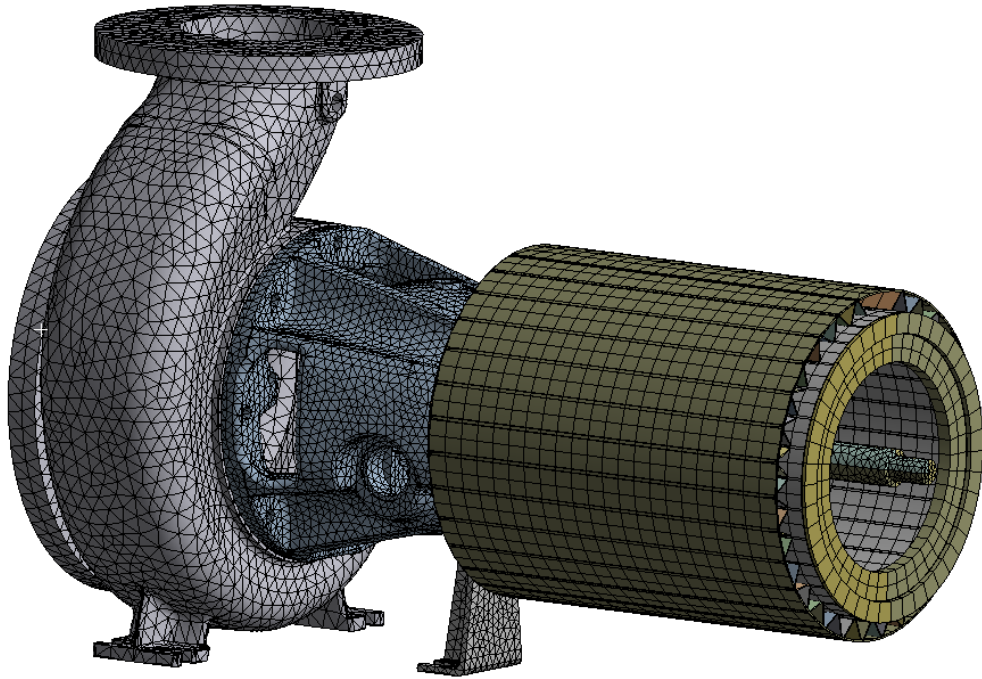


Figure 24. Meshed simulation model.

Table 4. Mesh properties.

Component	Element type	Number of elements	Number of nodes
Volute case	SOLID186/SOLID187	24790	47567
Bearing housing	SOLID186/SOLID187	48458	80887
Shaft	SOLID186/SOLID187	73471	128771
Support foot	SOLID186/SOLID187	1859	3969
Motor carrier	SOLID186/SOLID187	5287	9949
Electric motor			
casing	SHELL181	6014	7563
rotor	SOLID186/SOLID187	12964	40264
stator	SOLID186/SOLID187	1440	10140
taper bushing	SOLID186/SOLID187	1063	2286
front plate	SOLID186/SOLID187	5287	9949
rear plate	SOLID186/SOLID187	352	2362

Used element types were SOLID186, SOLID187 and SHELL181. SOLID186 and SOLID187 are solid 3D elements with three degrees of freedom per node: translation in the nodal x, y and z directions. Their difference is that SOLID186 is a 20-node brick element and SOLID187 is a 10-node tetra element. Shell elements are suitable for analyzing thin structures, such as the motor casing in this case. SHELL181 elements were used to model the electric motor casing. It is a four-node element with six degrees of freedom at each node: translations in x, y and z directions, and rotations about the x, y and z-axes (ANSYS 2015).

3.4 Constraints

Structure was constrained from points A–F (Figure 25). In all points translation in x, y and z direction and rotation around x- and z-axis were fixed. Only rotation around y-axis was allowed.

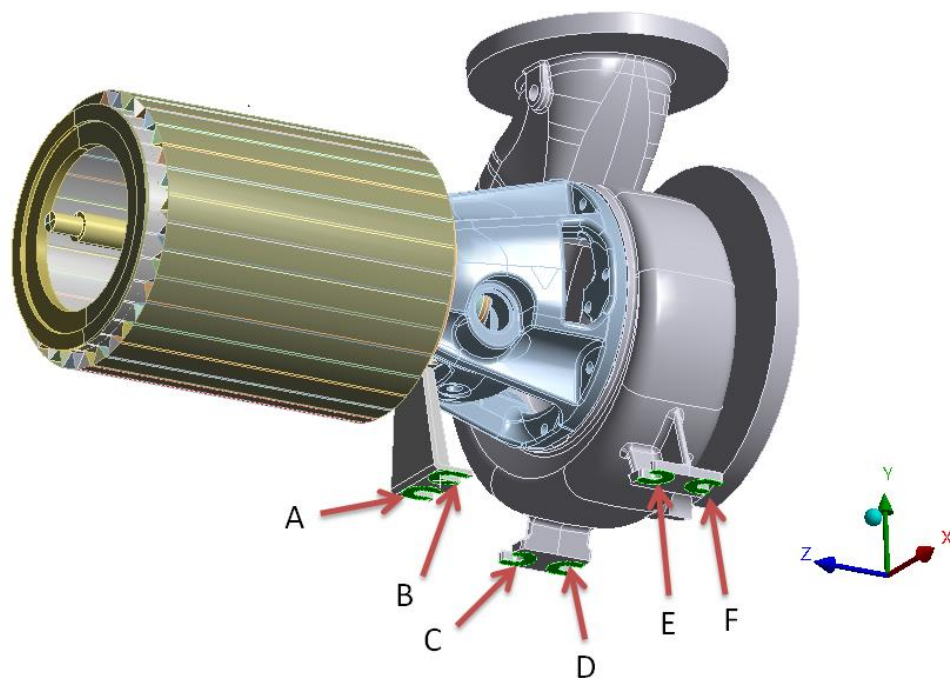


Figure 25. Constraint points for the volute case and support foot.

3.5 Joints and contacts

Two general joints were introduced to the model to represent bearings. In general joint degrees of freedom can be set from zero to six. In this case rotation around z-axis and translation in x- and y-directions were allowed. Rotation around z-axis was set free.

Translational degrees of freedom were given stiffness according to bearing properties. General joints were set as body-body connection between shaft and bearing unit. Figure 26 presents the joint locations.

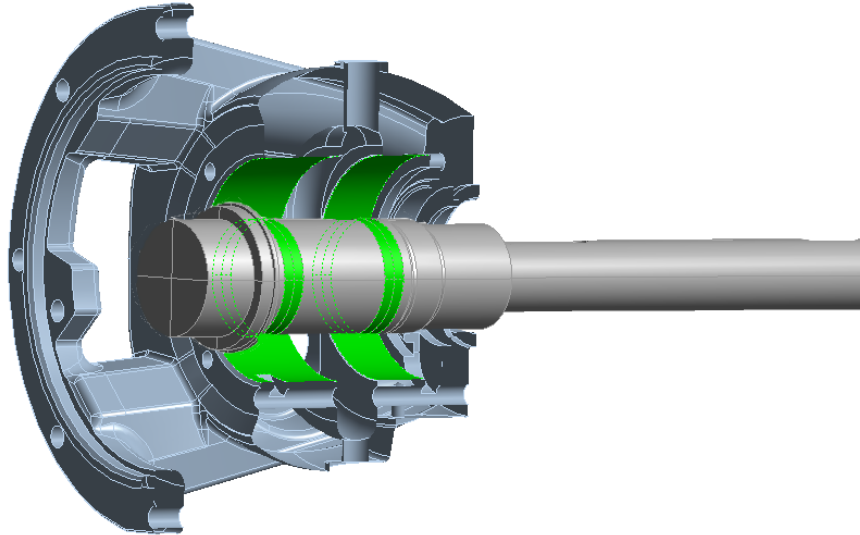


Figure 26. Bearings were modeled as general joints between the shaft and the bearing unit. Bearing contact surfaces are presented green in the figure.

All bolt connections were modelled with imprinted surfaces of two times the bolt head diameter in order to ensure accurate stiffness transfer between bolt-connected parts. The imprinted connection surface was then used to connect the two parts with bonded contact. (Sulzer 2016.) This type of connection is illustrated in Appendix I, cases 4–7.

All other contacts between parts were defined as bonded contacts. Formulation method was set to Multi-Point Constraint (MPC) and contact detection as program controlled. Contact pairs are presented in Appendix I.

3.6 Modeling of electromagnetic force

As it was stated in the theory section, attractive force in the air gap can be considered to be linear with respect to air gap length. It was also stated that because of the linear behavior of the force, it can be described as linear spring with negative spring rate. In the simulation model COMBIN14 element type was used as spring element. Total of 18 springs were equally distributed around the air gap: three in parallel and six on the rotor ring (Figure 27).

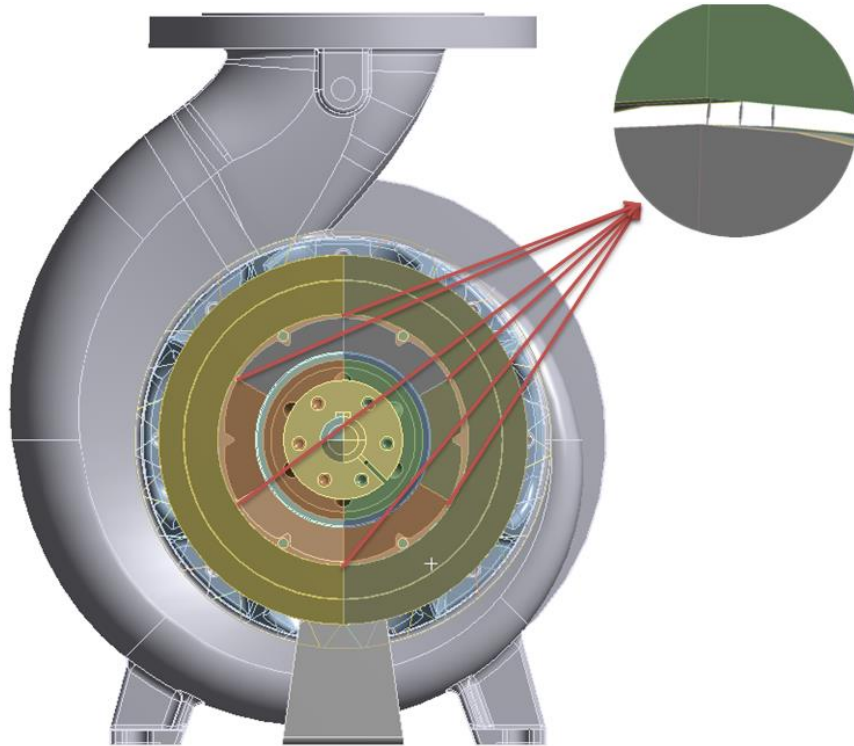


Figure 27. Spring distribution in the air gap.

Spring rate was determined based on calculations made by the PM motor manufacturer. In their calculations, radial forces were measured with 2D FEM by dividing the rotor into 10 equal size segments and deflecting each segment different amount in radial direction when electromagnetic field was present. By deflecting segments different amount it was possible to create situation where there occurred unequally distributed air gap. The segments were deflected in such a way that error of air gap eccentricity was 0.075 mm in the beginning and 0.3 mm in the end of the rotor. By dividing the radial force F_r in each segment with the displacement x , it was possible to calculate spring rate k for each segment according to $k = -F_r/x$. By taking into account spring rate for all 10 segments and multiplying it with the rotor length it was possible to determine spring rate for the whole rotor. Figure 28 presents a principal picture of the radial force measurement. In the figure F_r represents the radial force which grows linearly as the air gap gets smaller. According to PM motor manufacturer, spring rate for 126 mm long rotor was found to be $-1.025 \cdot 10^6$ N/m by following the previously explained method.

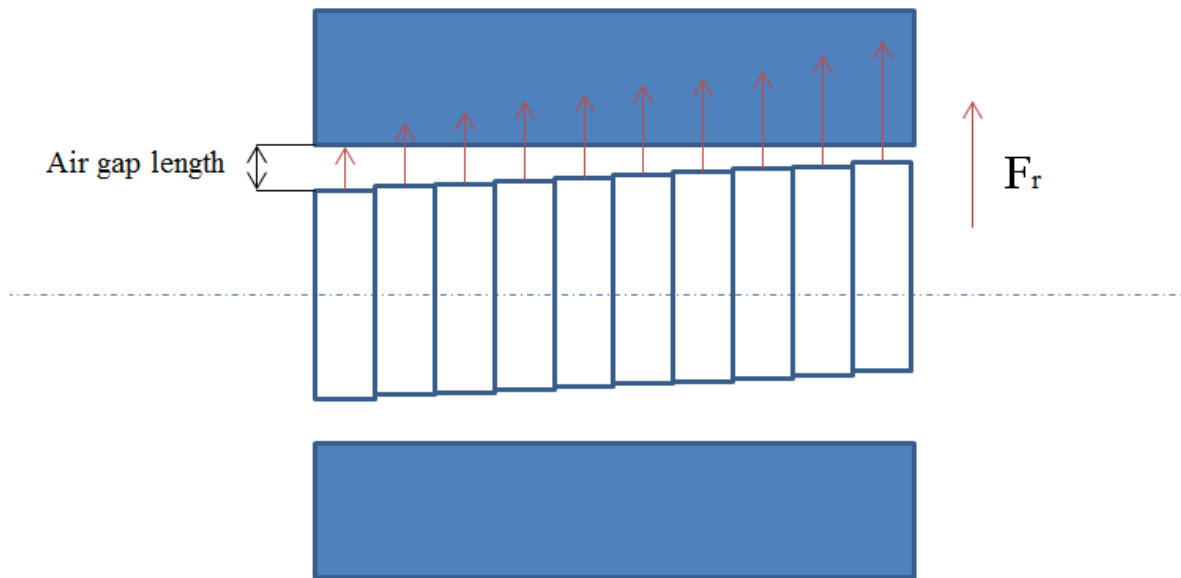


Figure 28. Principal picture of the radial force calculation.

3.7 Modal Analysis

In order to examine the system behavior modal and harmonic analyses were performed with ANSYS Mechanical. The results are later on compared with experimental measurements. Experimental measurements done at Sulzer Pumps Finland are performed without fluid or an impeller. This means that the torque is not required as much as in real case and thus also the stator current is lower than in fully loaded case. The radial force distribution provided by the electric motor manufacturer was performed on a stator without current. When the motor is fully loaded, the radial force is approximately 1.5 times the force without loading. This is due to the fact that required current grows linearly with respect to motor torque and radial force is directly related to stator current (Huurinainen 2016). As the correct amount of torque (and stator current) in the measurement setup was unknown, the spring rate could be optimized by comparing the natural frequencies of the simulation model with different spring rates to natural frequencies obtained from the measurements. Iteratively the spring rate was found to be $-1.365 \cdot 10^6$ N/m.

Modal analysis was performed for the structure in order to find natural frequencies and mode shapes of the system. In analysis settings search range was set to $1-10^7$ Hz from which ten first occurring modes were searched. Lower limit was set above zero in order to avoid rigid body modes. Coriolis Effect was turned on, solver type was set to Program Controlled and damping was taken into account. Table 5 presents first four natural

frequencies with 10 % eccentric air gap and Figure 29 presents the corresponding mode shapes. 10 first natural frequencies and corresponding mode shapes with 10 % eccentric air gap can be found in appendix II.

Table 5. First four natural frequencies.

Mode	Natural frequency [Hz]	Direction
1	33.99	X
2	49.69	Y
3	81.19	X
4	95.49	Y

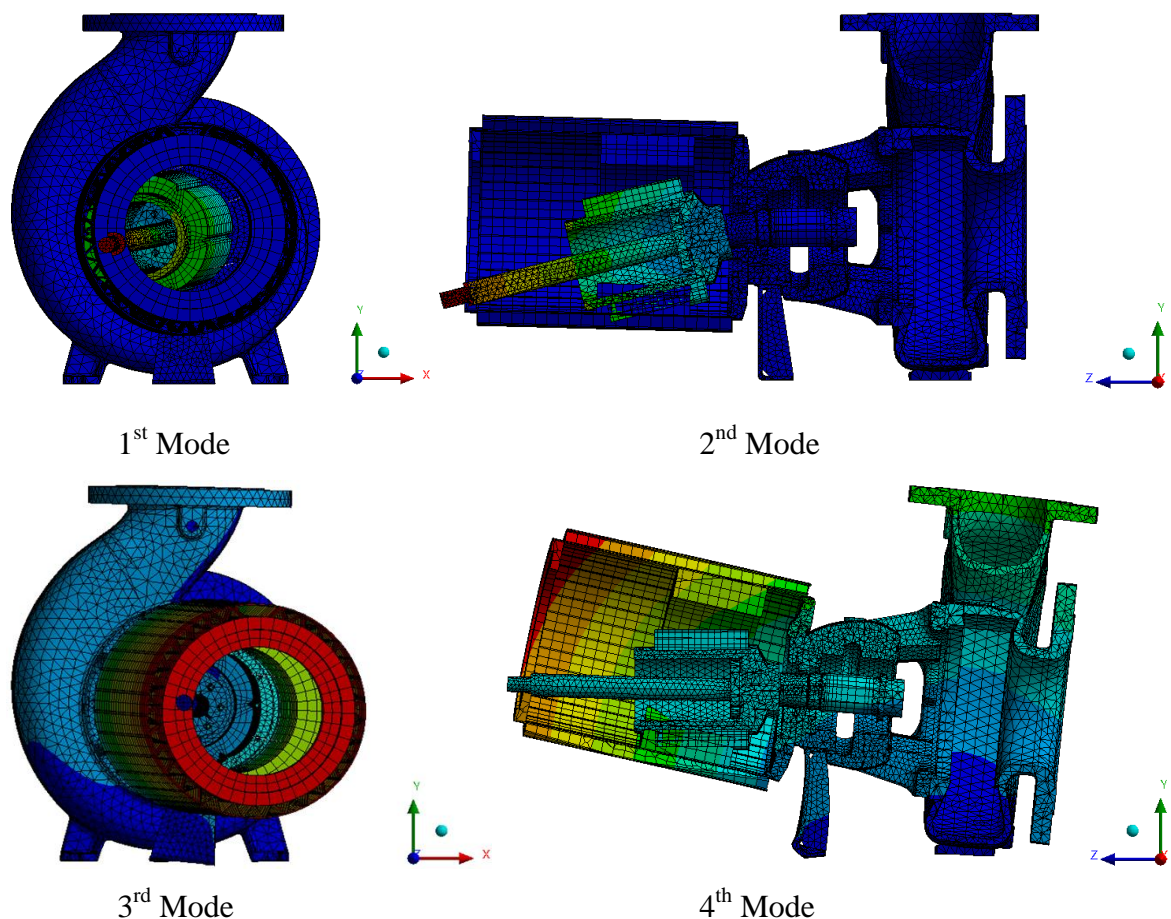


Figure 29. First, second, third and fourth mode shape.

As it can be seen from Figure 29 the first two mode shapes are rotor dominated modes. Modes three and four are motor casing dominated modes. What is common for all these

modes is that their behavior narrows the air gap. Noticeable is also that two of these modes are in the operation range of the motor (0–4200 rpm) as it can be seen in the Campbell diagram (Figure 30). All four modes are excited if twice-rotation speed (2X) excitation is considered.

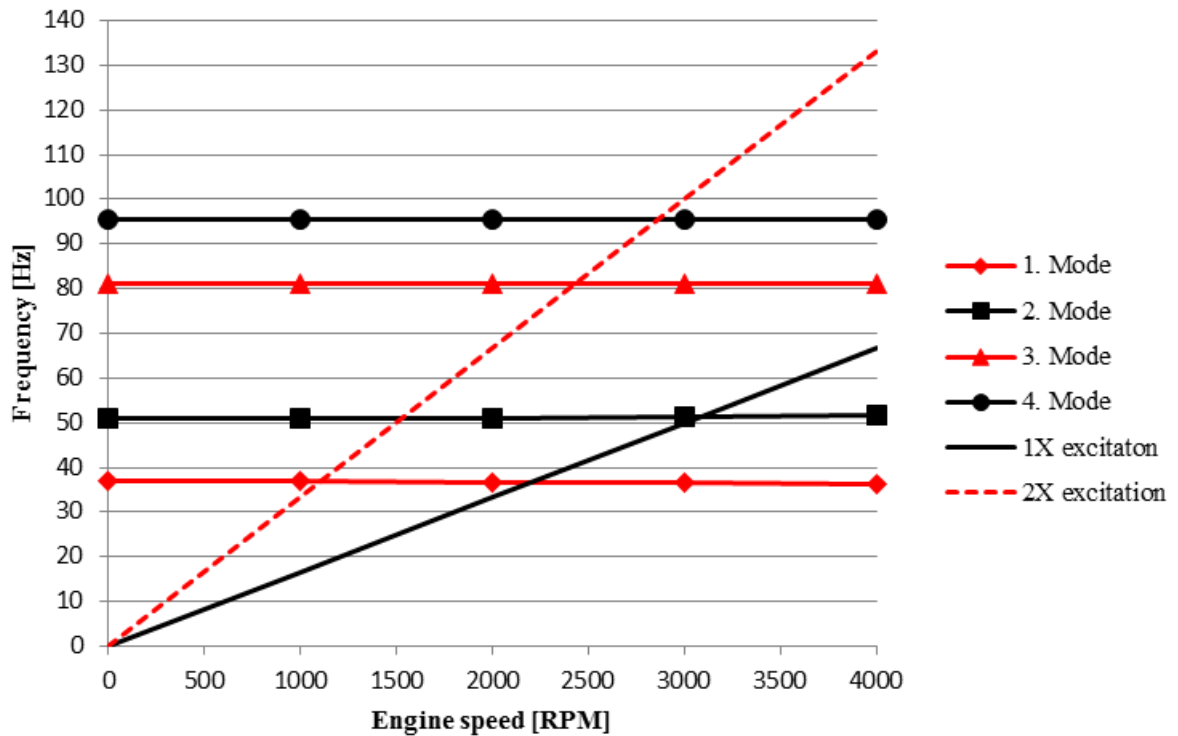


Figure 30. Campbell diagram in speed range of 0–4000 rpm.

3.7.1 Modal analysis with varying motor load

As it was stated before, the magnetic force increases linearly with respect to stator current. It was also said that stator current increases almost linearly with respect to required motor torque. This can be taken into account by increasing the spring rate of the springs between stator and rotor. Table 6 presents different motor loading cases where the spring rate varies. In the table are presented following cases: a case when no current is led to stator, a case when motors are tested and balanced (no fluid or impeller is involved in the pump side) and a case where motor is under full loading.

Table 6. Different motor loading cases where the spring rate varies.

Case	Spring rate [N/mm]
Stator without current (Calculated)	-1025
Casing without impeller or fluid	-1365
Full loading	-1537

Figure 31 presents a diagram which shows how the spring rate variation affects to six first vibration modes. In all cases air gap length was kept at 2.5 mm and bearings were modelled as rigid in order to inspect only the influence of the radial forces.

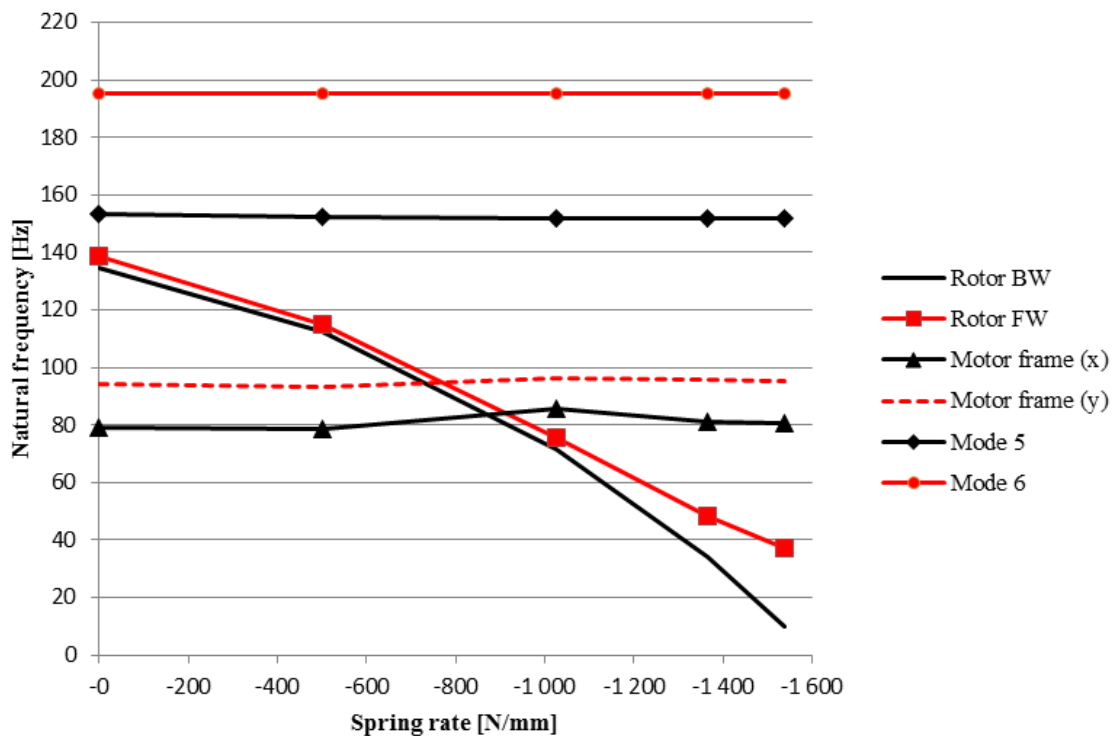


Figure 31. Natural frequencies of 6 first modes with variable spring rate.

As it can be seen from Figure 31, if spring rate is increased the rotor dominated natural frequencies decreases. When the spring rate is approximately 900 N/mm the rotor modes start to occur at lower frequencies than the motor frame dominated modes. Noticeable is that the spring rate does not have influence on higher vibration modes. In the figure are included modes 5 and 6 which represent the non-air gap related modes and it can be seen how the spring rate does not have any effect on them. This diagram indicates how

important it is to take the electromagnetic force into account when simulating electric motors, since the natural frequencies of the rotor dominated modes decrease substantially.

3.7.2 Modal analysis with variable air gap

In order to inspect the system with springs attached between the rotor and stator behavior more thoroughly, modal analysis was performed with varying air gap length. Figure 32 depicts how the motor frame was first rotated from the bearing housing end around y-axis amount of β .

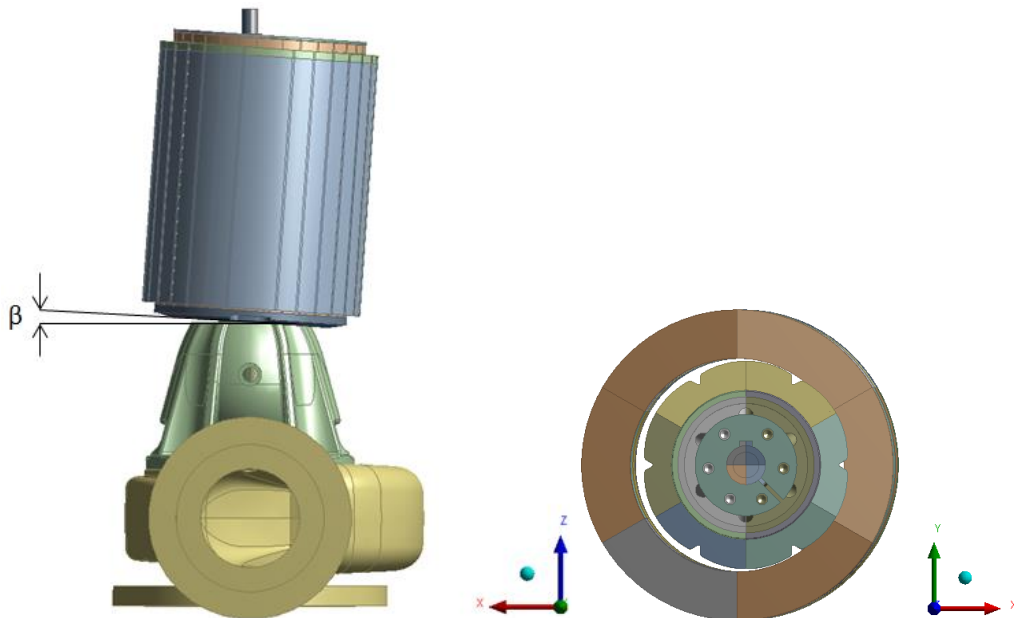


Figure 32. Motor frame was rotated around y-axis amount of β to change the air gap length.

Rotation was performed with different β values and the effect of air gap variation to natural frequencies was investigated. Rotation amounts were calculated as percentage of the error in eccentricity. Figure 33 shows the effect of varying air gap with rotated stator at 3000 rpm. In the analysis settings damping was set to program controlled and Coriolis Effect on.

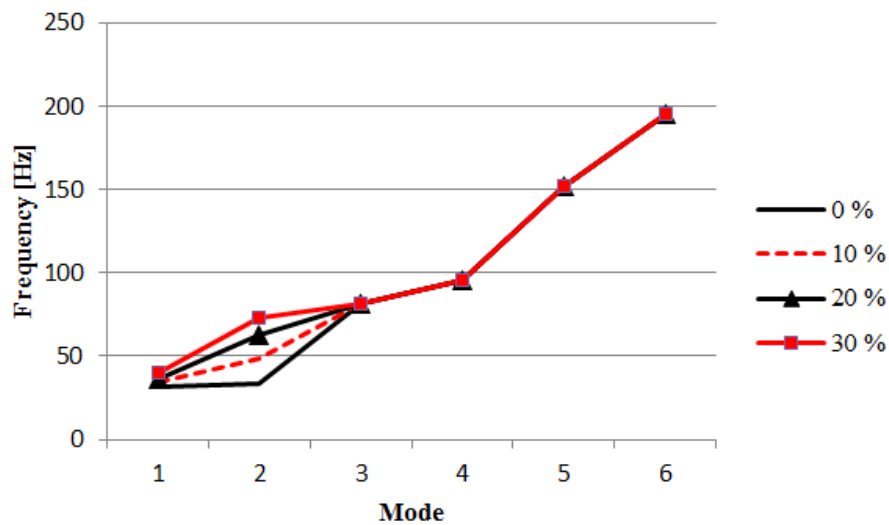


Figure 33. Natural frequencies with varying motor frame angle. 10 % equals 0.25 mm error and 30 % 0.75 mm error in air gap eccentricity.

When the motor frame is aligned in order to change the air gap length the first two natural frequencies appear to increase. First natural frequency increases by 8 Hz and second by 24 Hz when air gap length changes from 0 % to 30 % error.

Same procedure was performed for the rotor. Figure 34 illustrates the rotor rotation around x-axis amount of β .

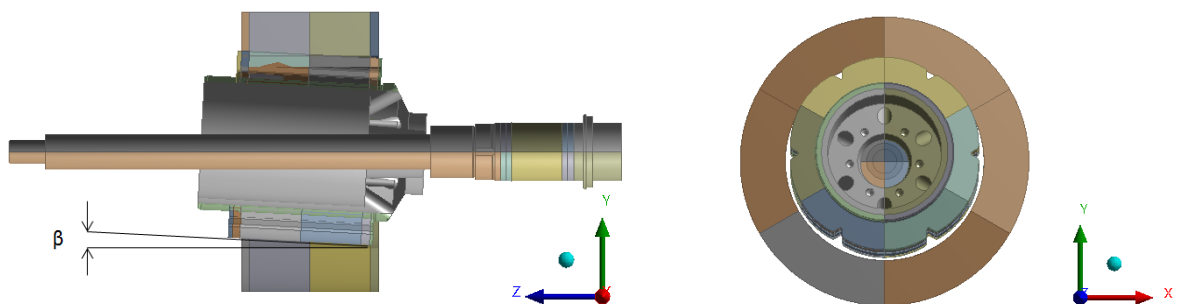


Figure 34. Rotor was rotated around x-axis amount of β in order to change the air gap length.

Also in rotor deflection the rotation was performed with different β values and the effect of air gap variation to natural frequencies was investigated. Rotation amounts were calculated as percentage of the error in eccentricity. Figure 35 illustrates the effect of varying air gap

with rotated rotor at 3000 rpm. In the analysis settings damping and Coriolis Effect were turned on.

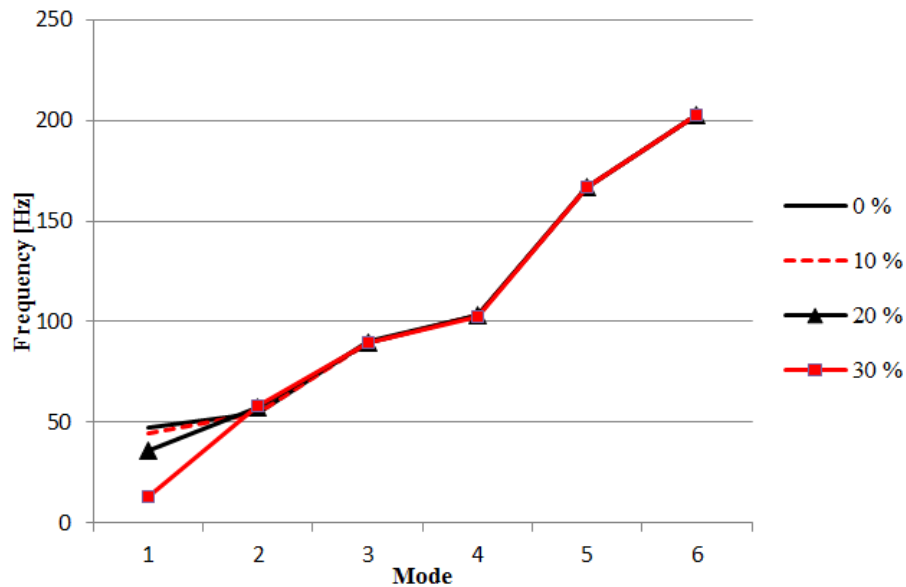


Figure 35. Natural frequencies with varying rotor angle. 10 % equals 0.25 mm error and 30 % 0.75 mm error in air gap eccentricity.

Unlike in the case of eccentric stator, with eccentric rotor the first natural frequency decreases by 34 Hz and second increases by 4 Hz when air gap length error increases from 0 % to 30 %.

3.7.3 Gyroscopic effect with variable air gap

Relation between air gap length and intensity of gyroscopic effect was investigated on eccentric motor frame. Figure 36 presents first (a) and second (b) mode with varying motor frame eccentricity on speed range of 0–5000 rpm. With completely concentric frame the first mode natural frequency rises by 3.5 Hz and second by 4.3 Hz when the rotor velocity is increased from 0 to 5000 rpm. In case with 30 % error in eccentricity the difference on the first mode was 0.3 Hz and in second 0.5 Hz. From the diagrams it can be concluded that by increasing the error in eccentricity, the gyroscopic effect decreases. However, less than 5 Hz difference indicates that gyroscopic effect does not have big influence on the system behavior on its operating speed range. Gyroscopic effect was inspected only on the first two modes since they are the rotor dominated modes.

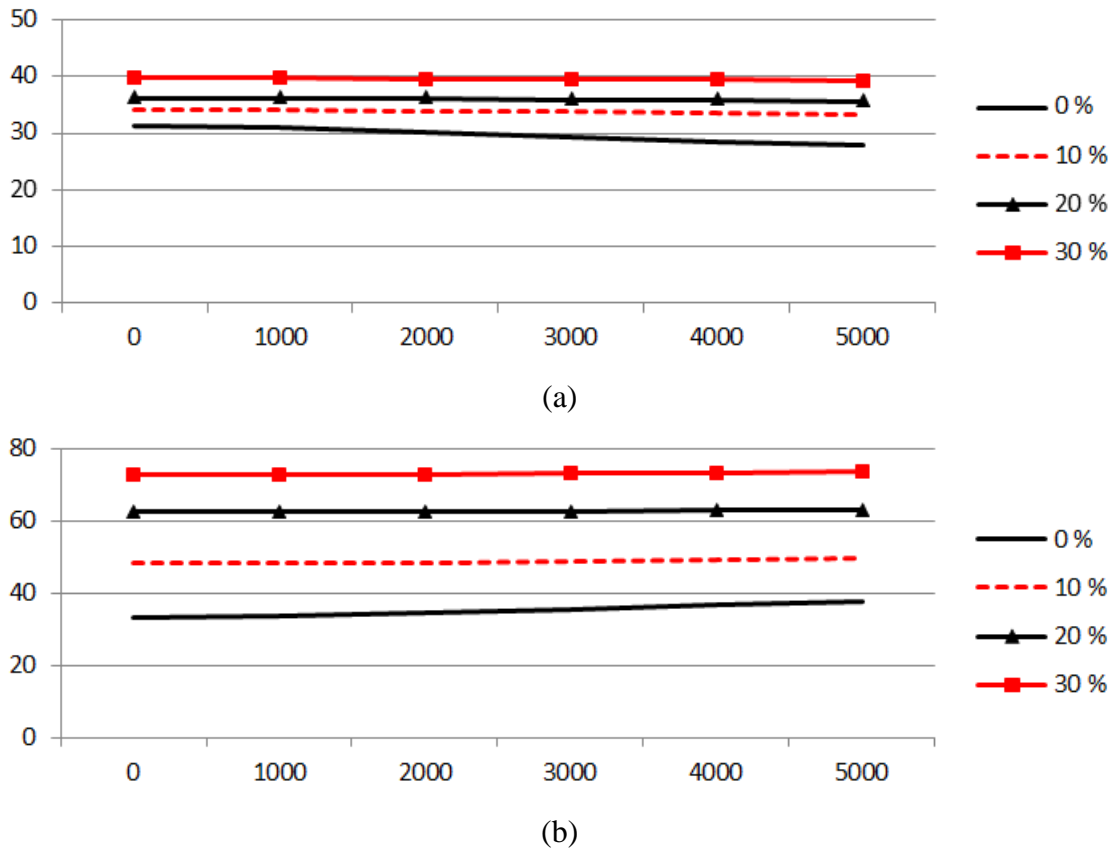


Figure 36. Gyroscopic effect with varying air gap introduced by deflecting motor frame.

3.8 Harmonic response analysis

Harmonic response analysis was performed for the model with unbalance mass of 2.1 Gramm. Rotating force produced by the unbalance mass was set on a node which is located on 52.5 mm radius. On this specific radius there are locations where mass is applied during the motor balancing process. 2.1 g mass on 52.5 mm radius creates rotating force of $1.1025 \cdot 10^{-4}$ kgm. The force was applied using Ansys commands (Appendix III). Figure 37 illustrates how oscillation velocity was measured from motor end. Figure 38 depicts harmonic response of the system with 10 % motor frame and 5 % rotor eccentricity.

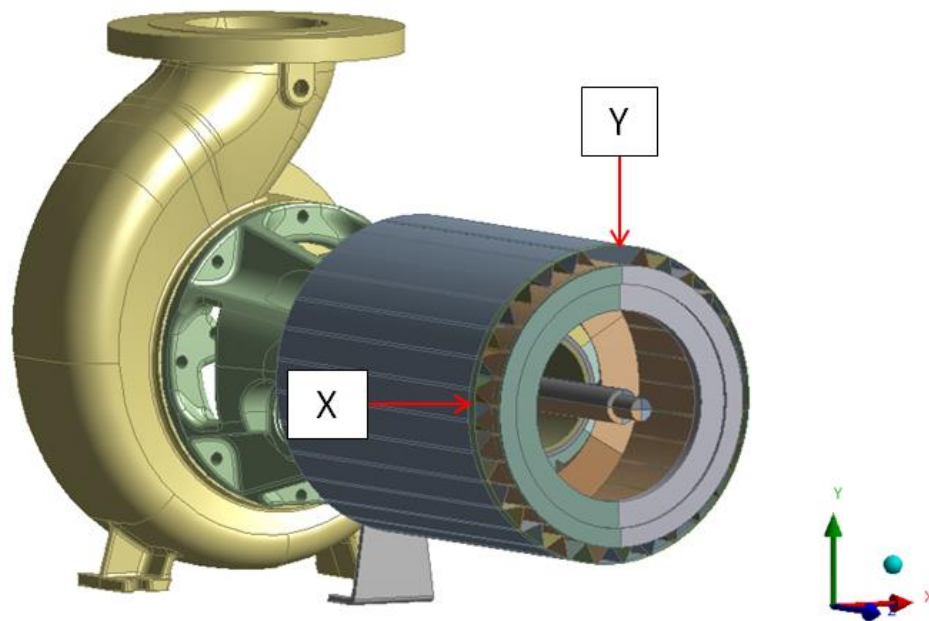


Figure 37. Measuring point for oscillation velocity in x- and y-direction.

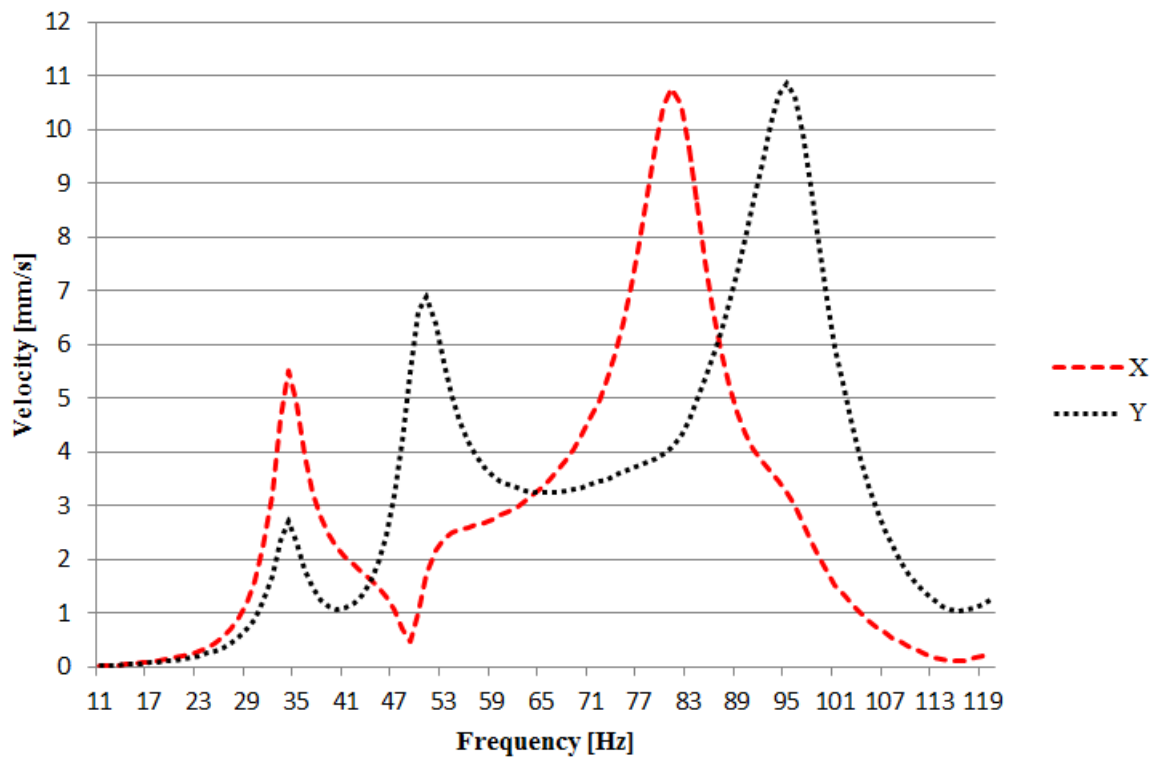


Figure 38. Harmonic response of the simulation model in x- and y-direction.

As it can be seen from Figure 38 the peak velocity values can be found at same frequencies as the natural frequencies. Since the rotor dominated modes (first and second mode) are

whirling modes, they can be both seen in x- and y-direction. Motor frame dominated modes are directional bending modes so they appear only in the particular direction.

3.9 Experimental tests

In order to verify the simulation model, experimental measurements were performed. The setup for the measurements consists of the prototype, a laptop, four piezoelectric accelerometers (IMI VO-622) and a data acquisition device (National Instruments NI-9234). The setup is illustrated in Figure 39.

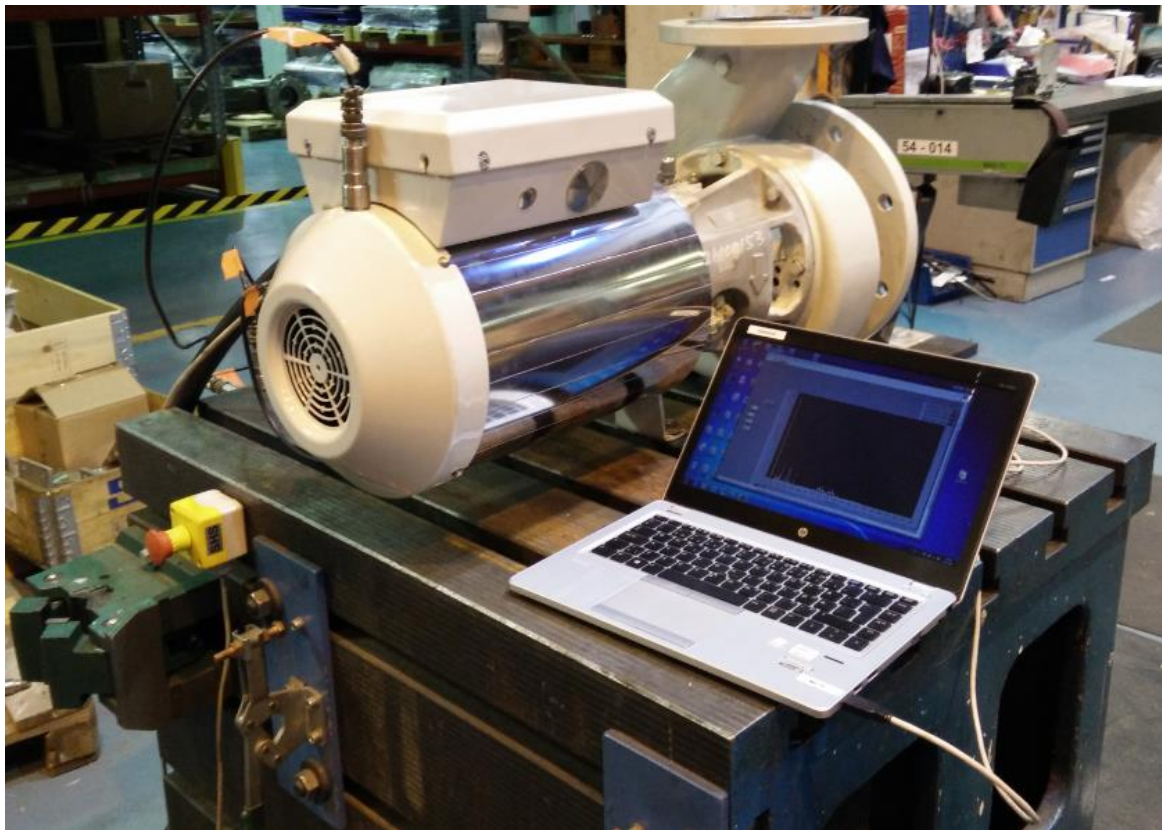


Figure 39. Measurement setup.

Two accelerometers were attached to motor end in x- and y-direction as illustrated in Figure 40. Two other sensors were attached on the table in x- and y-direction to find out the influence of the foundation. Accelerometers were connected to the data acquisition device which was again attached to USB-port on the laptop. Data was measured in interval of one hertz and LabView 2009 program was used to convert the measurement data from time domain to frequency domain by perform Fast Fourier Transform (FFT). In FFT Flat

Top was used as a window function. LabView was also used to integrate the acceleration values into velocity and record the data.

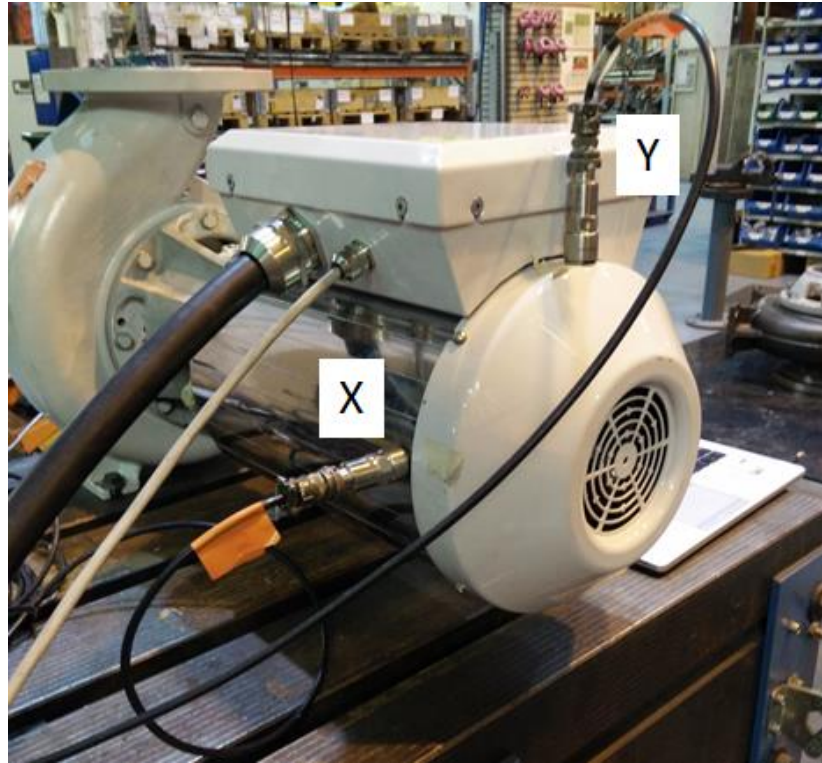


Figure 40. Vibration velocities were measured in x- and y-directions from the motor end.

In optimal situation the air gap is 2.5 mm in all directions. In order to find out the effect of variable air gap length, the motor frame was installed eccentric with respect to rotor. Eccentricity was introduced by applying shimming plate between the bearing housing and motor carrier (Figure 41). In such a way air gap could be adjusted in a similar way as it was adjusted in the simulation model (Figure 32). 0.1 mm thick shimming plates were added so that air gap eccentricity could be set to 0, 10 and 20 % in horizontal direction in the motor end. Air gap length was measured with a customized feeler gauge in which measuring limits were set with 0.25 mm increments.

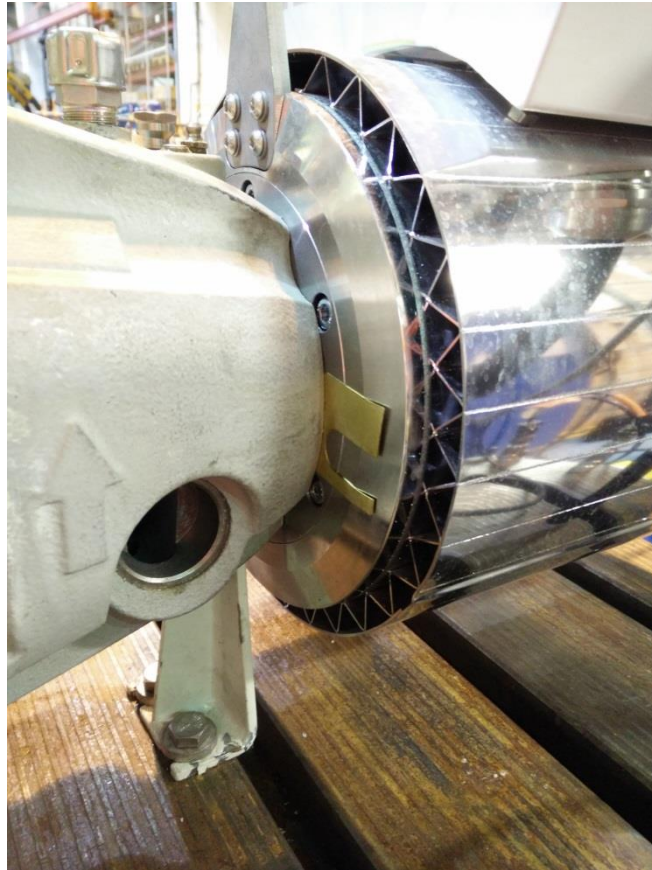


Figure 41. Air gap length was adjusted by applying 0.1mm thick shimming plates between the bearing unit and motor carrier.

In all eccentricity cases the measurements were performed at operating speeds of 1000, 2000, 3000 and 4000 rpm. Also a ramp from 0 to 4100 rpm in 70 seconds was driven in every case. Stable operating speeds indicate if a natural frequency is near that specific speed as the oscillation velocity rises if the pump is operated near a natural frequency. The ramp is needed to be able to plot a spectral map. The spectral map can be used to discover natural frequencies and engine speed lines at whole operating speed range.

After the motor was accelerated to 4100 rpm, power was shut down from the frequency converter. During the engine shutdown a separate spectral map was recorded in order to observe the effect of stator current to natural frequencies (chapter 3.8.1).

The pump-motor assembly was mounted on a steel base plate. The base plate was attached to a wooden support (Figure 42). As the stiffness of wood is considerably lower compared to steel, its influence needs to be taken into account when analyzing the results.



Figure 42. Wooden support below the base plate.

3.9.1 Static eccentricity

Before any measurements were performed, the air gap was measured around the rotor from the motor end. Because of the motor structure, it was not possible to measure the air gap length in front end of the motor. In the rear end a static eccentricity of 0.25 mm was found in horizontal direction. As the 0.25 mm error corresponds to 10 % eccentricity error, the first set of measurements was performed without adding any shimming plates between the motor frame and bearing unit. Second case was performed with 20 % (0.5 mm) error and third with 0 % error. In all cases the rotor was assumed to be centered, even though unbalanced mass is always present because of manufacturing tolerances. Figure 43 illustrates the static air gap difference and table 7 presents the air gap length e in different cases.

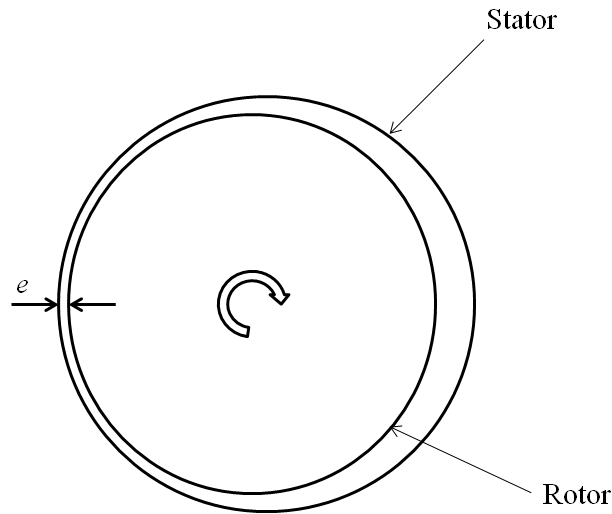


Figure 43. Air gap length e in rear end of the rotor was modified in different cases.

Table 7. Static eccentricity cases.

Case	e [mm]	Error in eccentricity [%]
1	2.25	10
2	2.00	20
3	2.50	0

Originally it was planned to perform vibration measurements for eccentric rotor as well, in order to find out the vibration behavior with dynamic eccentricity. However, the rotor could not be installed during the measurements in a way where the dynamic eccentricity could be observed.

3.9.2 Measurement results

Microsoft Excel 2010 was used to create spectral maps from the measurement data. Figure 44 and 45 present spectral maps with 10 % eccentric stator from x- and y-direction respectively. In spectral map natural frequencies can be seen as horizontal lines (marked with red arrows). Linearly rising lines shows the excitation frequency. In this case resonance occurs mainly on the once-rotation and twice-rotation excitation frequency. These two lines are marked on the figures as 1X and 2X respectively.

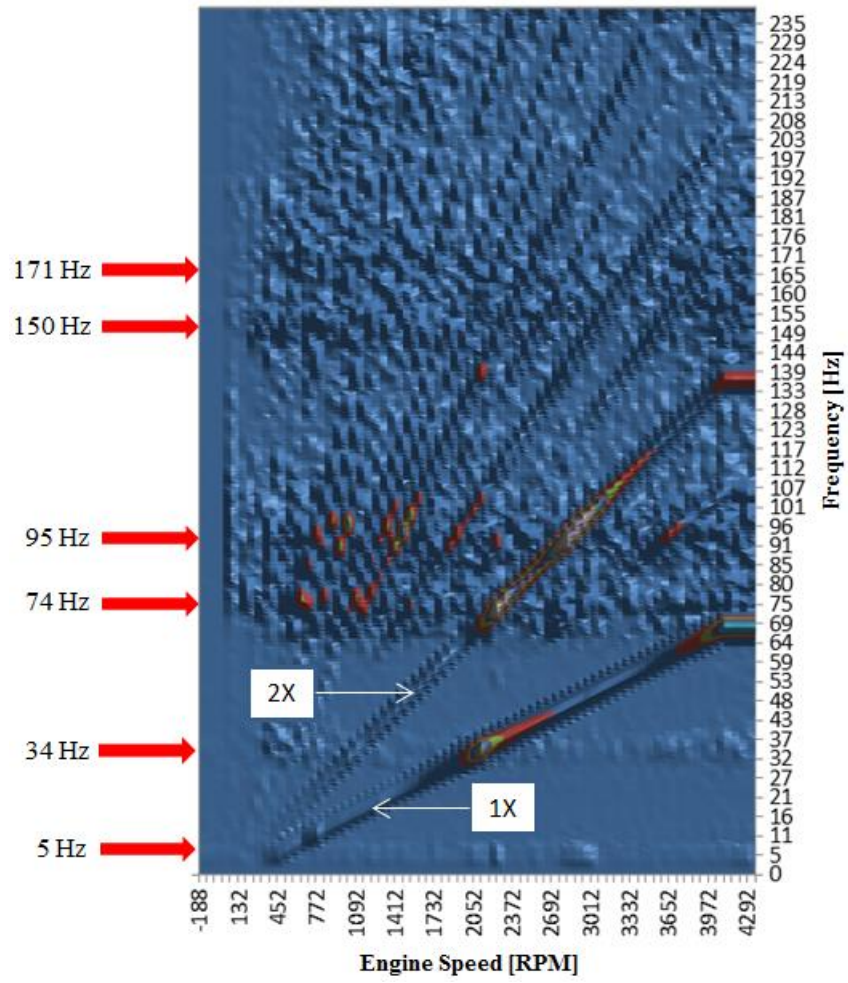


Figure 44. Spectral map from x-direction in motor rear end.

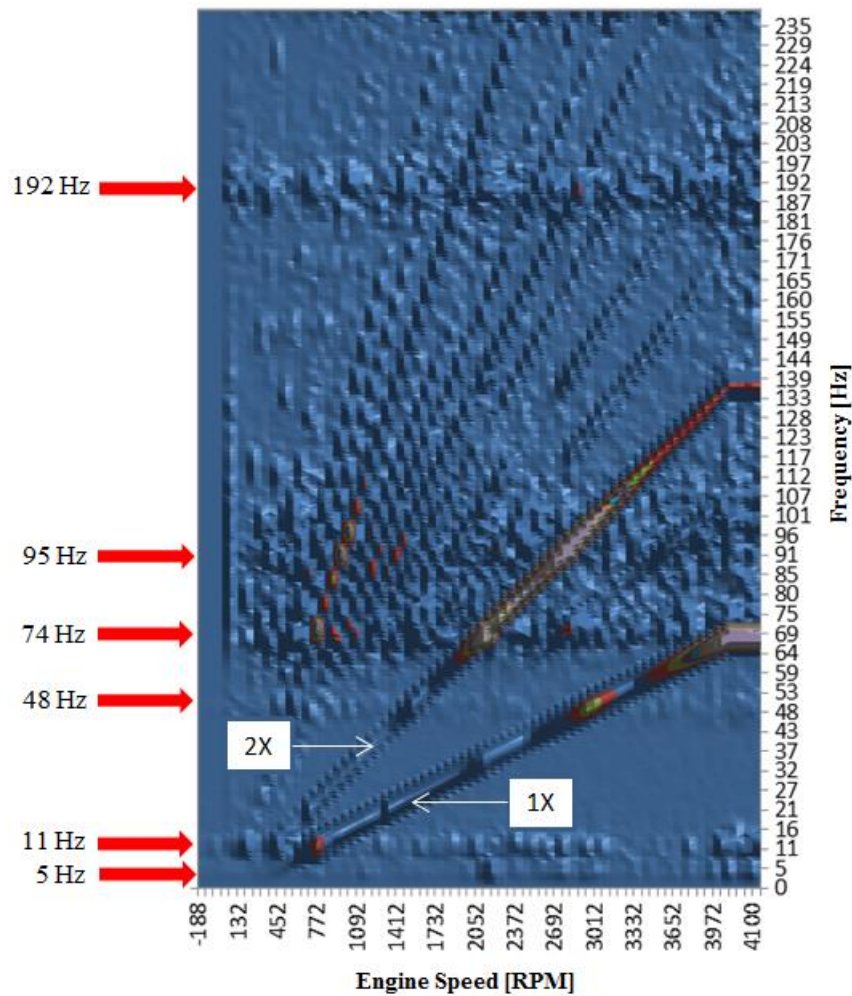


Figure 45. Spectral map from y-direction in motor rear end.

From Figure 44 and 45 natural frequencies can be seen at 5, 11, 34, 48, 74, 95, 150, 171 and 192 Hz. First two natural frequencies which can be seen around 10 Hz can be neglected as they can be assumed to be from the foundation. Figure 46 presents spectral map measured from the table x-direction. In this figure the natural frequency near 10 Hz can be clearly seen as the others faded or disappeared. Natural frequencies at 34 Hz and 49 Hz can be considered as rotor dominated modes. Frequencies at 74 Hz and 95 Hz are assumed to be motor frame dominated modes. Last three natural frequencies do not occur on the first or second multiple of the engine speed so they are not under interest.

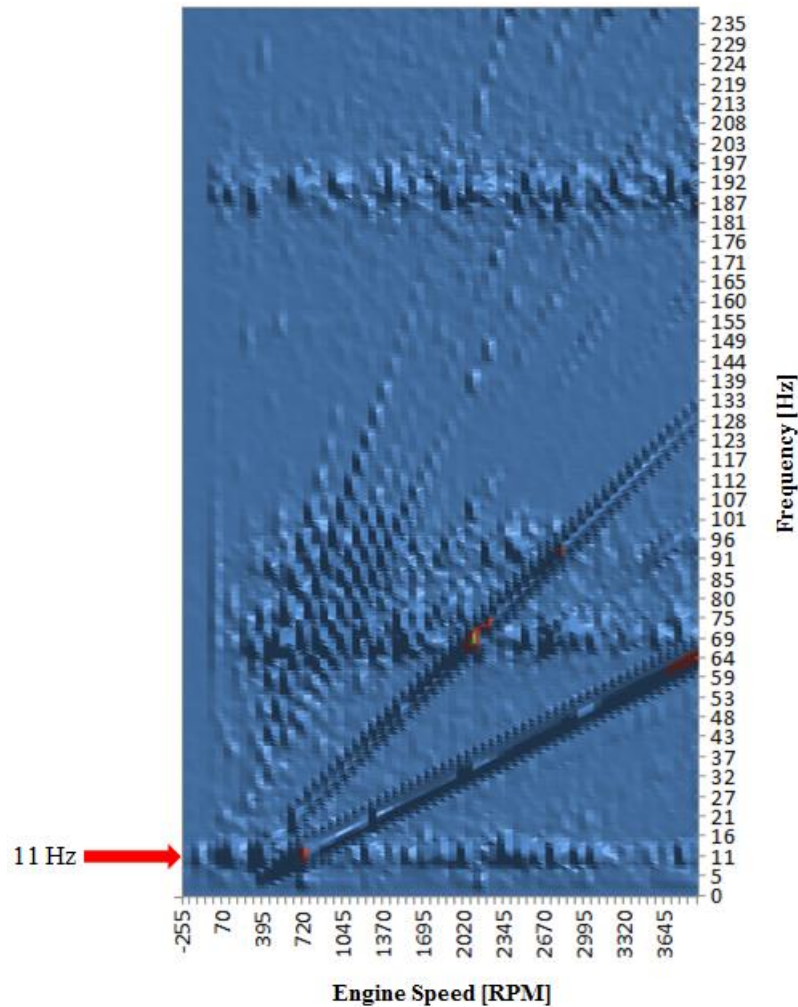


Figure 46. Spectral map measured from the foundation in x-direction.

If the measurement data is inspected in 3D-view from y-direction, two separate peaks can be seen near the first motor frame mode. The peaks can be seen more clearly as the motor frame eccentricity increases. Figure 47 shows 3D spectral map from a measurement with 20 % eccentricity error. First peak can be seen at 68 Hz and second at 74 Hz. The first peak occurring at 2X line is assumed to be multiple of the first vibration mode at 34 Hz. It can be seen also on the first rotation speed line which is excited at a point where motor achieves constant rotating speed. The second peak at 74 Hz is assumed to be first bending mode of the motor frame since on that specific frequency also a natural frequency can be seen.

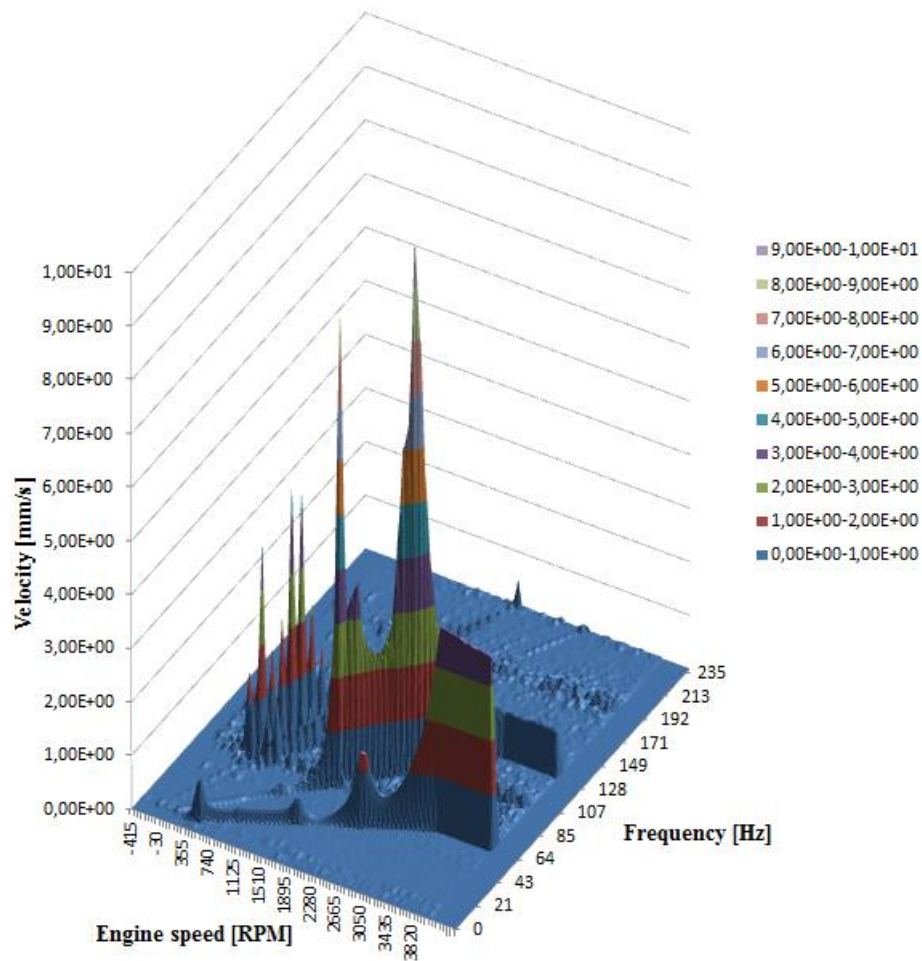


Figure 47. 3D spectral map of 20 % eccentric motor frame (y-direction).

If the same case is inspected from the data in x-direction there can be seen also two separate peaks around the second motor frame dominated vibration mode. This can be also seen more clearly with increased eccentricity than in the more concentric cases. Figure 48 shows 3D spectral map with 20 % eccentricity measured from the x-direction. In this figure two separate peaks can be seen at 2X line at frequencies of 94 Hz and 99 Hz. Since the motor bending modes are directional bending modes, they can be seen only in the data measured from the corresponding direction.

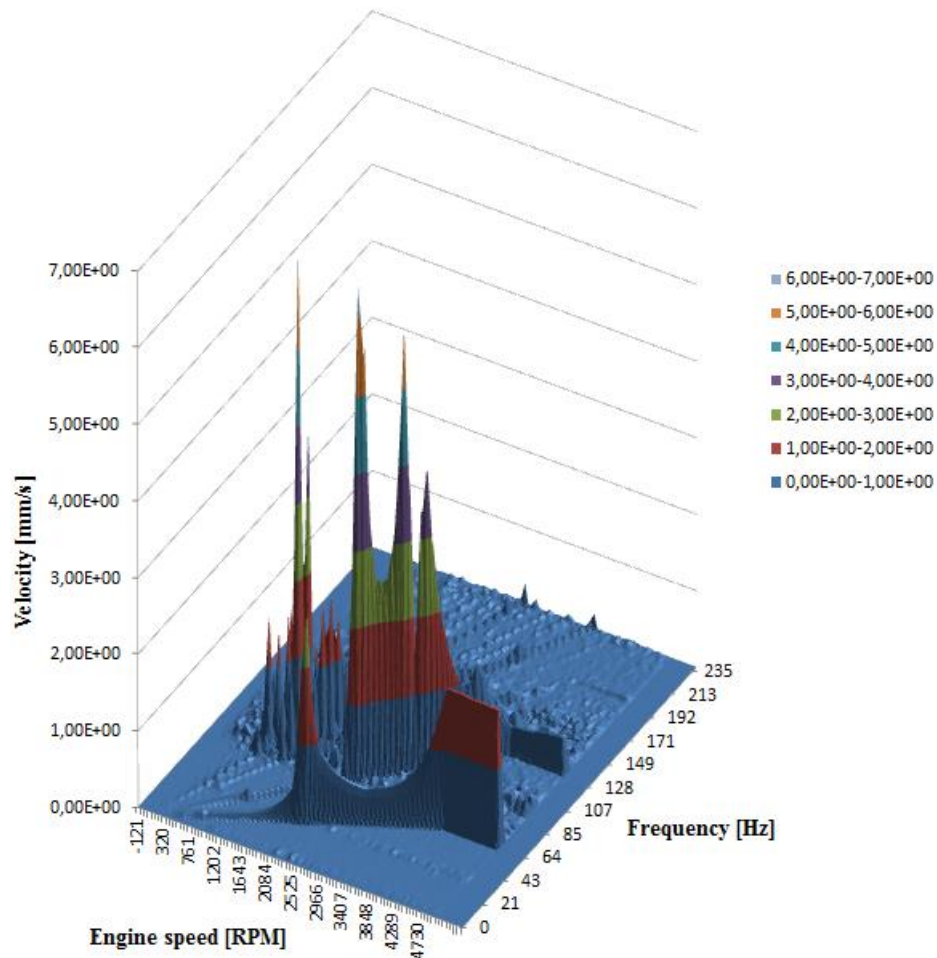


Figure 48. 3D spectral map of 20 % eccentric motor frame (x-direction).

3.10 Verification of the simulation model

After the measurements were performed, the simulation model was tuned according to the measurement results. In section 3.8.1 it was stated how the spring rate of the springs between rotor and stator has significant effect on the first two natural frequencies: as the spring rate is increased (i.e. unbalanced magnetic pull increases) the first two natural frequencies decrease. As the rotor is supported with radial angular contact ball bearings, also their radial stiffness has influence on the rotor dominated natural frequencies. Figure 49 presents bearing stiffness with respect to natural frequency of four lowest vibration modes. In this Figure first and second modes are rotor forward and backward whirling modes. Third and fourth modes are motor frame directional vibration modes.

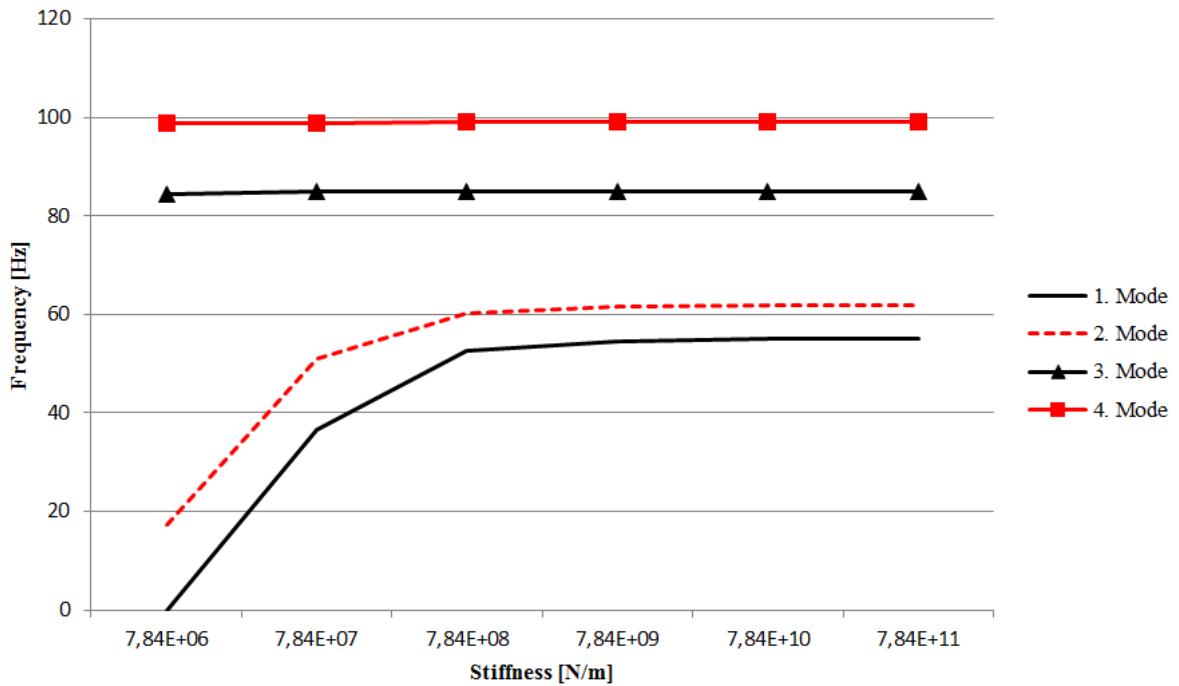


Figure 49. Effect of bearing stiffness to natural frequencies of the whole structure.

As it can be seen in Figure 49 the natural frequency of rotor dominated modes rise until certain point as the bearing radial stiffness rises. After this point bearings act as rigid. The bearing stiffness does not have effect on the motor frame dominated modes.

Verification of the simulation model was done by comparing the natural frequencies to measurement results. In order to find good correlation between the simulation model and measurement results the spring rate was set to $-1.365 \cdot 10^6$ N/m and bearing stiffness to $7.84 \cdot 10^7$ N/m. The values were chosen by comparing situation where the motor frame was set 10 % eccentric with respect to rotor and 2.1 g unbalanced mass was applied. Damping was determined iteratively based on the vibration velocities. Structural damping for the whole system was set to 5 %. In table 9 are compared first seven natural frequencies from the measurements and the ones obtained with simulation model. In addition to frequencies presented in table 9, resonance occurs also at 68 Hz and 96–99 Hz. First one is caused by once-rotation speed (1X) excitation and second twice-rotation speed (2X) excitation frequency and they occur at second multiples of the rotor dominated modes (34 Hz and 48 Hz). However the simulation model does not take into account the 2X harmonic excitation, or multiples of the natural frequencies so these do not occur in the simulation results.

Table 9. Natural frequencies from measurement data and simulation model.

Mode	Measurement [Hz]	Simulation model [Hz]	Difference [Hz]
1	34	34	0
2	48	50	2
3	74	81	7
4	91–94	95	1-4
5	150	151	1
6	171	-	-
7	192	195	3

According to the natural frequency comparison, a good correlation between the simulation model and actual prototype can be found. Vibration velocities at resonant points can be seen in Appendix IV.

4 COMPARISON OF SIMULATION MODEL AND PROTOTYPE

To be able to make adjustments to the structure based on the simulation model the model has to be reliable and behave like the actual structure. In previous section natural frequencies of the simulation model were confirmed to match the ones obtained with laboratory measurements. In this section simulation results are compared more thoroughly to measurement results by inspecting the effect of varying air gap length and stator current.

4.1 Comparison with static 10 % eccentricity error

As it was stated before, natural frequencies of the simulation model depends on bearing stiffness and spring rate of the electromagnetic springs. These two values were modified based on the natural frequencies of the prototype which were obtained from the measurements. In Figures 50 and 51 harmonic response of the simulation model is compared to measurement data in x- and y-direction respectively. In the figures measurement data is presented as black line and simulation result as red dashed line.

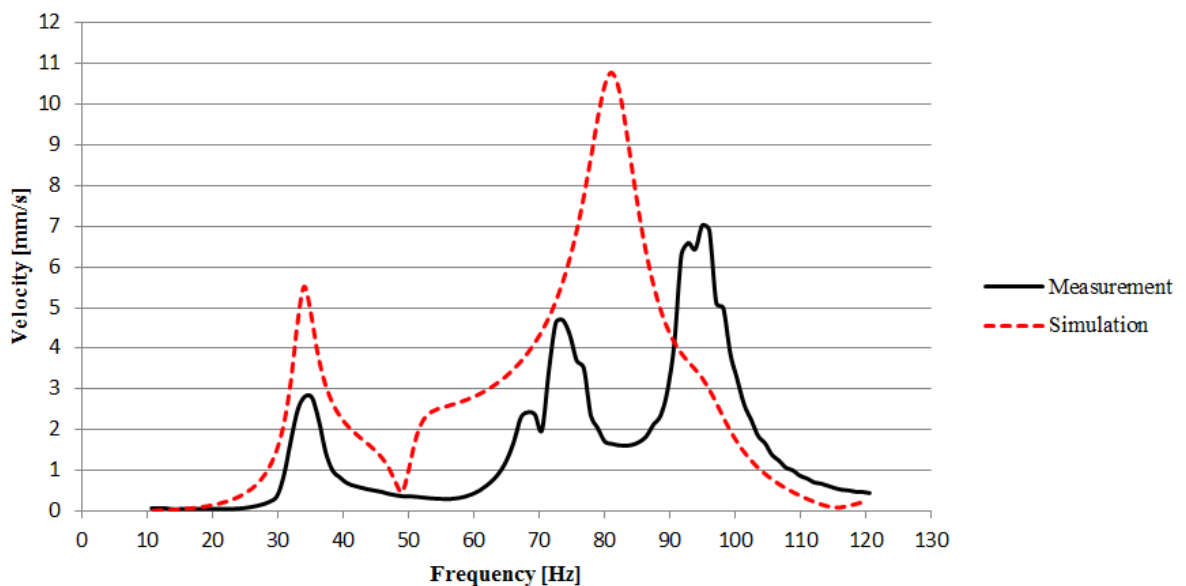


Figure 50. Vibration velocity with respect to frequency in motor end x-direction with 10 % eccentric motor frame and 2.1 g unbalanced mass. Simulation model is presented with red dashed line and measurement data as black line.

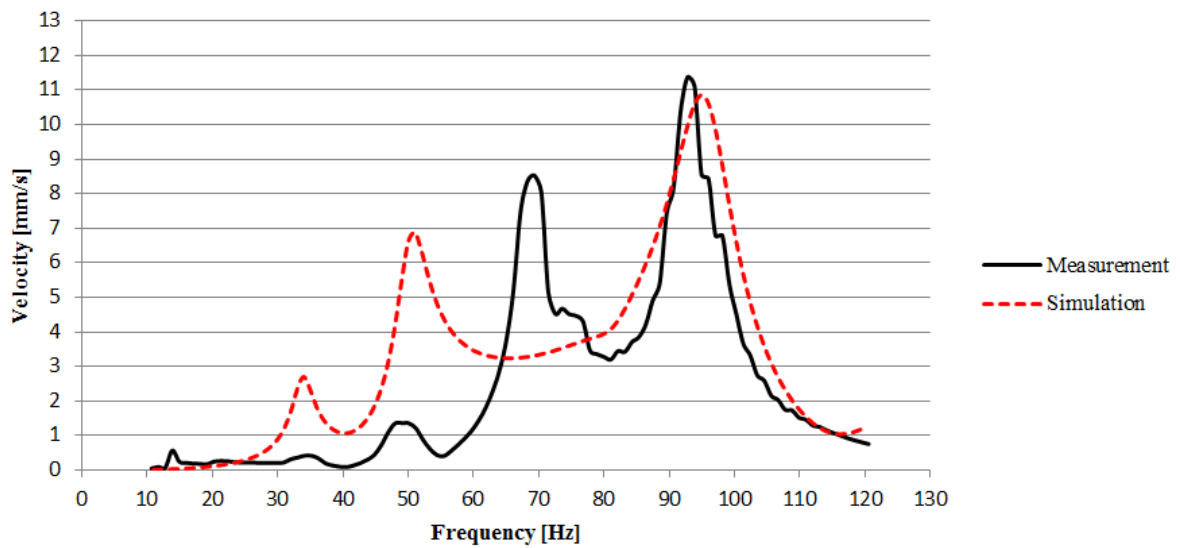


Figure 51. Vibration velocity with respect to frequency in motor end y-direction with 10 % eccentric motor frame and 2.1 g unbalanced mass. Simulation model is presented with red dashed line and measurement data as black line.

In Figure 50 first natural frequency can be seen as a peak at 34 Hz in both the simulation and measurement data. This vibration mode is first rotor dominated mode. In Figure 51 it can be seen also as a smaller peak at same frequency. Second rotor dominated mode can be seen in Figure 51 at 48 Hz. In measurement data this peak is considerably smaller compared to the simulation model which is assumed to be because of inaccurate damping characteristics.

If the measurement data is inspected in both figures, two peaks can be seen near 70 Hz. The first peak at 68 Hz is caused by once-rotation speed excitation when it intersects with second multiple of the first rotor mode. The second peak at 74 Hz is first bending mode of the motor frame reacting in horizontal direction. This mode can be seen also in the simulation results at 81 Hz. In Figure 50 two separate peaks can be seen weakly close to 95 Hz. In Figure 51 two separate peaks cannot be recognized. Close to this point affect two frequencies. Depending on the measurement set the first occurs at 91–94 Hz and second between 96–99 Hz. The first frequency is motor frame dominated mode reacting in vertical direction. This mode can be seen also in the simulation results at 95 Hz. The second peak between 96–99 Hz is caused by the twice-rotation speed excitation when it intersects with second multiple of the rotor dominated mode at 48 Hz. These twice-rotation speed excited frequencies do not occur in the simulation model since only once-rotation speed excitation

is modelled. Figure 52 illustrates the 1X and 2X induced resonance areas. As it can be seen, the 1X excitation ends close to 69 Hz when the motor reaches its constant rotating speed (4100 rpm).

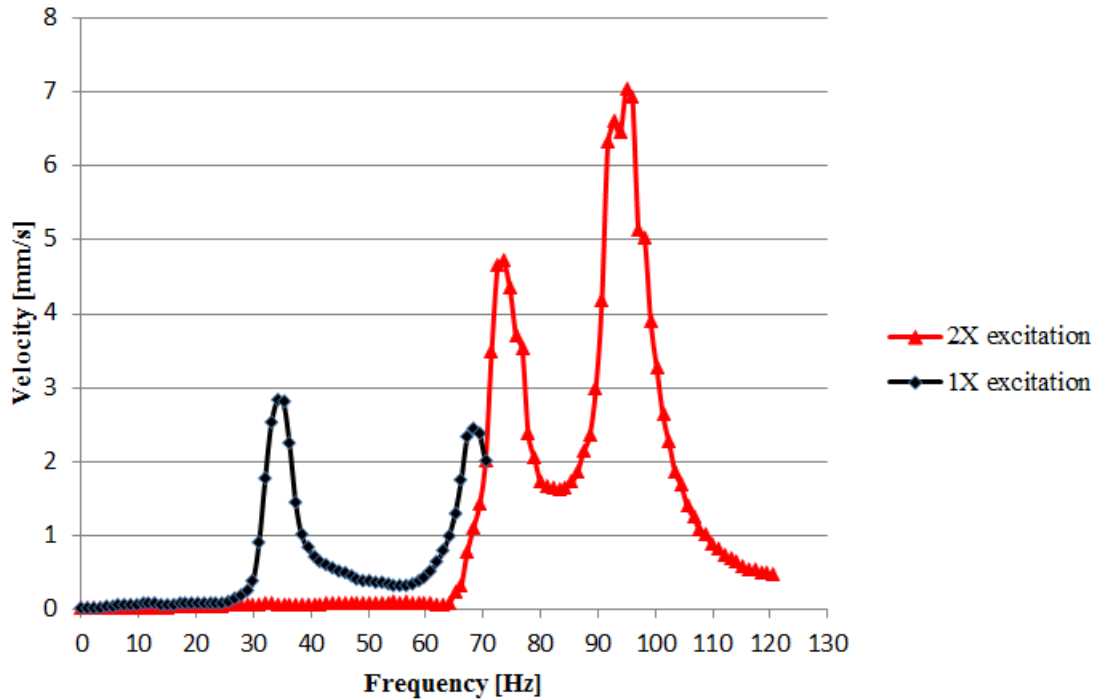


Figure 52. 1X and 2X excitation induced resonance areas from motor end x-direction.

4.2 Effect of unequally distributed air gap to vibration velocities

In theory section it was stated how unbalanced magnetic pull increased as the air gap length decreased. Since the air gap is never equally distributed between rotor and stator it is necessary to inspect its effect to vibration velocities. Figure 53 presents vibration velocities with 0 % and 20 % eccentric motor frame, measured from the motor end horizontal direction.

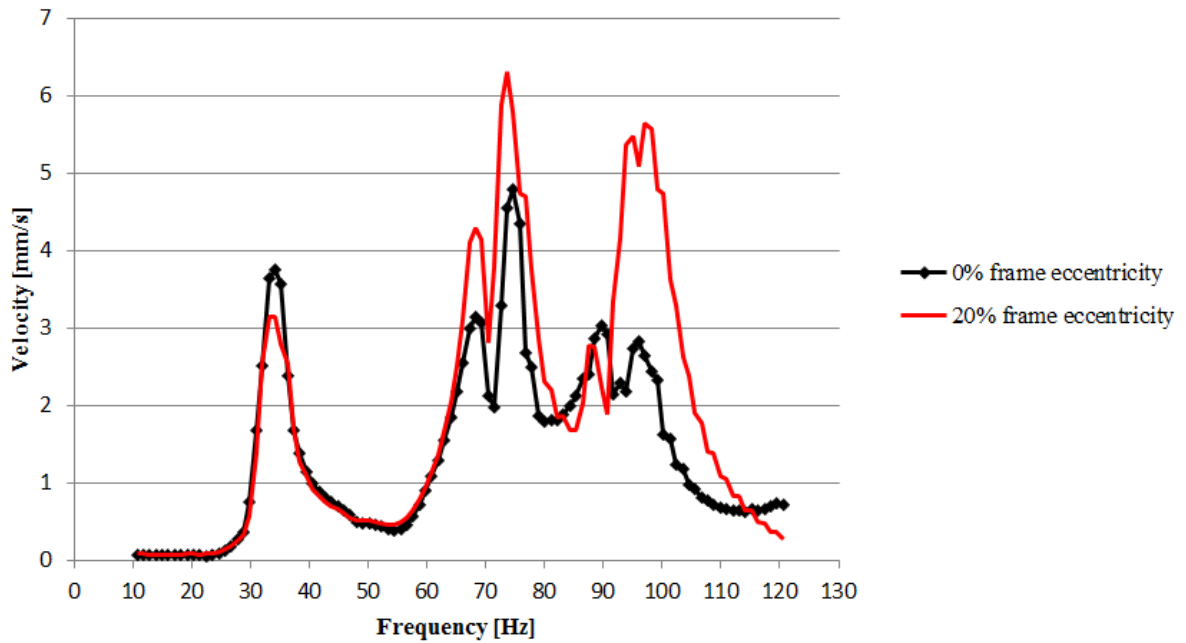


Figure 53. Vibration velocities from experimental measurements in motor end x-direction with 0 % (black line) and 20 % (red line) eccentric motor frame. 2.1 g unbalanced mass was used.

At 34 Hz vibration velocity of the first mode damps as the air gap length decreases. At 68 Hz can be seen resonance caused by the twice-rotation speed of the first vibration mode, which increases as the air gap length decreases. At 74 Hz can be seen the first vibration mode of the motor frame and at 91 Hz the second. Vibration velocity of the first motor frame mode increases as the air gap length decreases but the second decreases slightly. At 96 Hz can be seen the resonance caused by twice-rotation speed of the second rotor dominated mode. At this point vibration velocity increases significantly (99 %) as the air gap length decreases. Table 10 presents the vibration velocities at each point.

Table 10. Vibration velocities with 0 % and 20 % eccentricity from x-direction. In both cases 2.1 g unbalanced mass was applied.

Frequency [Hz]	0 % [mm/s]	20 % [mm/s]
34	3.76	3.15
68	3.15	4.29
74	4.74	6.32
91	3.04	2.77
96	2.84	5.65

Same motor frame rotation from 0 % to 20 % was inspected with the simulation model (Figure 54). As it can be seen in Figure 54 the vibration velocity of the first rotor dominated mode increases from 5.75 mm/s to 6.34 mm/s. In addition the corresponding natural frequency occurs at 40 Hz with 0 % eccentricity and at 36 Hz with 20 % eccentricity. The first vibration mode of the motor frame occurs at 81 Hz and the vibration velocity stays at 10.8 mm/s when the frame is rotated.

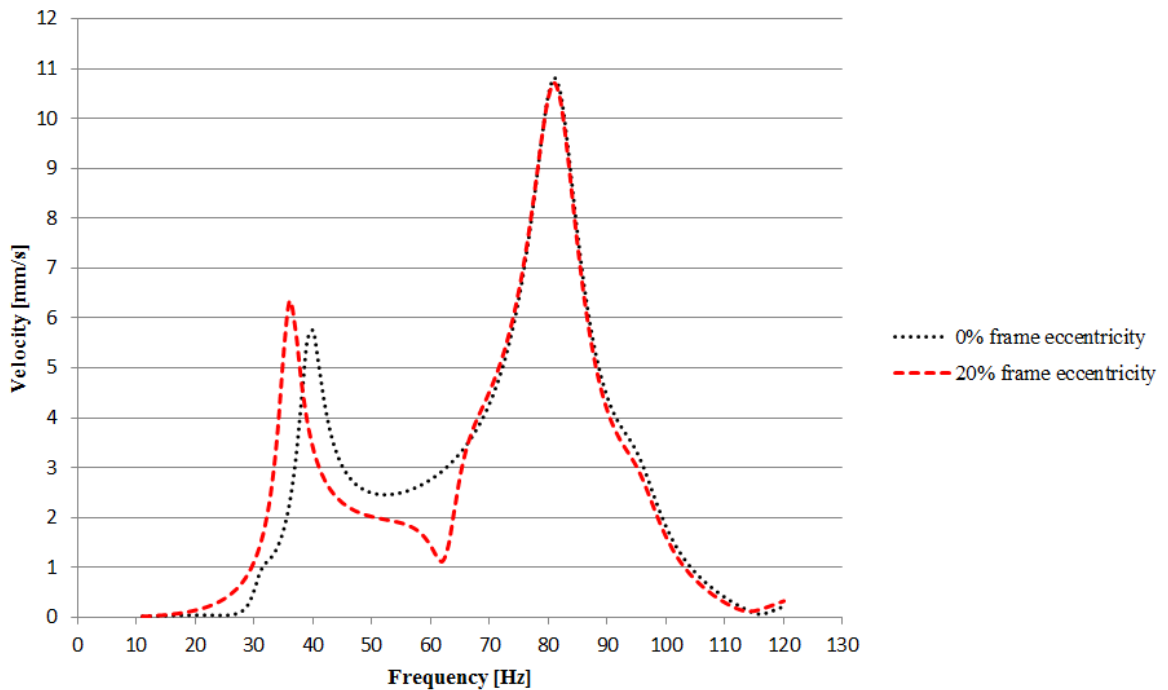


Figure 54. Vibration velocities from simulation model in x-direction with 0 % (black line) and 20 % (red line) eccentric motor. 2.1 g unbalanced mass was used.

When the vibration velocities are inspected from motor end y-direction (Figure 55) the first rotor dominated mode can be seen as a much smaller peak at 34 Hz compared to the measurement data obtained from x-direction. From this measurement direction also the second rotor dominated mode can be seen at 48 Hz. However, vibration velocity of this mode does not vary as the air gap length is decreased. Highest vibration velocity from the measurements was found on second multiple of the first vibration mode at 68 Hz. In this direction the vibration velocity at 68 Hz decreased as the air gap length decreased. With concentric motor frame the first vibration mode of the frame can be barely seen at 74 Hz but with 20 % eccentricity the vibration velocity at this point increases noticeably. The second motor frame mode cannot be easily recognized at 91 Hz with the concentric frame

but with 20 % eccentricity it can be found. With 20 % eccentricity the twice rotation-speed resonance of the second rotor mode can be separated at 97 Hz. With 0 % eccentricity error the motor frame vibration mode and twice-rotation speed resonance appears as one large peak (91–94 Hz) from which the two different frequencies is hard to recognize. Table 11 presents vibration velocities at each occurring frequency measured from y-direction.

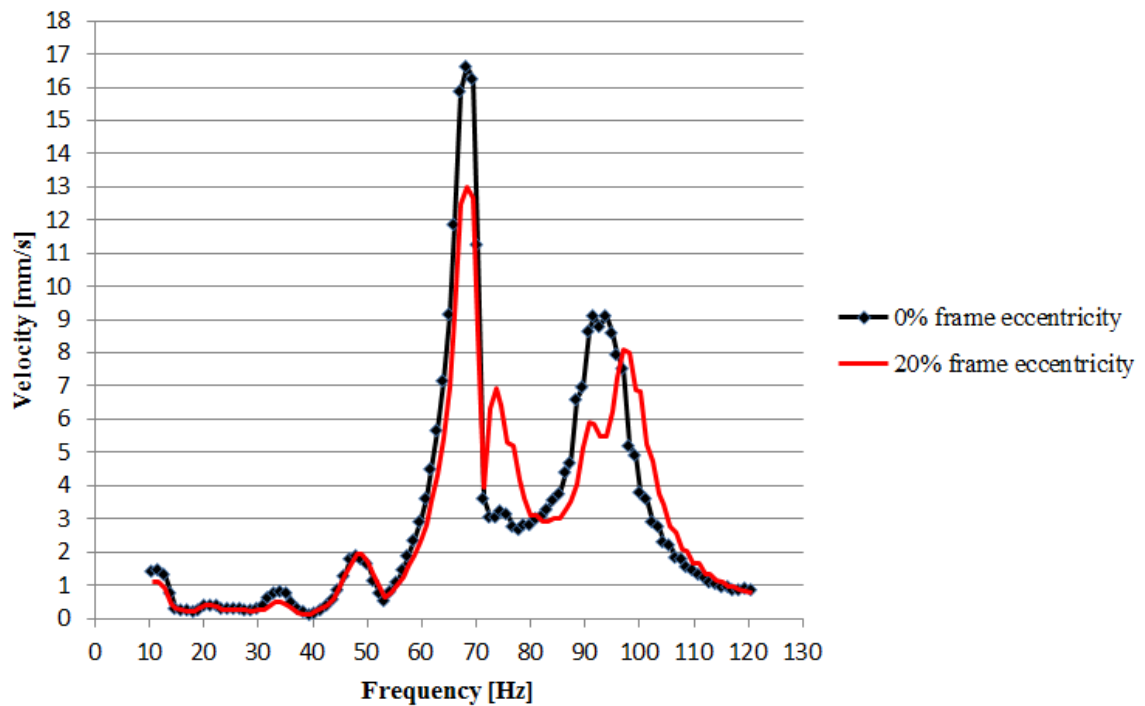


Figure 55. Vibration velocities from experimental measurements in motor end y-direction with 0 % (black line) and 20 % (red line) eccentric motor frame. 2.1 g unbalanced mass was used.

Table 11. Vibration velocities with 0 % and 20 % eccentricity from y-direction. In both cases 2.1 g unbalanced mass was applied.

Frequency [Hz]	0 % [mm/s]	20 % [mm/s]
34	0.81	0.47
48	1.88	1.93
68	16.64	13.01
74	3.26	6.92
91	9.14	5.89
94–97	9.14	8.10

Figure 56 presents harmonic response of the simulation model in y-direction. The simulation results show how the vibration velocity of the first mode decrease from 5.23 mm/s to 1.46 mm/s as the air gap length decreases. Also frequency of this mode increase from 31 Hz to 36 Hz. In case of second vibration mode the natural frequency increases considerably as the air gap narrows. Similar kind of behavior cannot be recognized from the measurements so it is assumed to result from the spring elements which were used in modelling of electromagnetic force. At 95 Hz can be seen second motor frame mode. At this point vibration velocity decreases as the air gap length decreases.

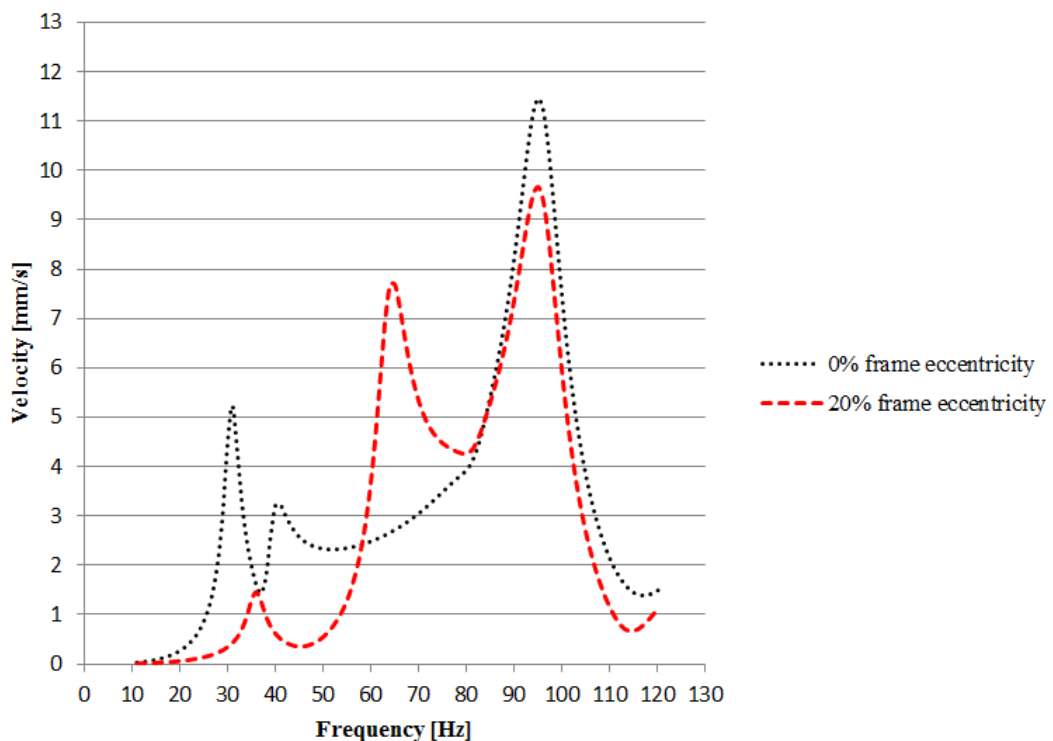


Figure 56. Vibration velocities from simulation model in y-direction with 0 % (black line) and 20 % (red line) eccentric motor. 2.1 g unbalanced mass was used.

4.3 Effect of stator current on system behavior

In section 3.8.1 motor load (and stator current) relation to magnetic pull was discussed. In Figure 31 it could be seen how the natural frequencies appeared to decrease as the spring rate (i.e. magnetic pull) was increased. This phenomenon was inspected by comparing measurement data while the engine was accelerated up to 4100 rpm, to data obtained when engine was let run down from 4100 rpm to 0 rpm without any current. Engine reached stationary position in approximately 20 seconds. Figure 57 and 58 show vibration

measurements from x- and y-direction respectively. In the figures ramp up correspond the data obtained with power on and ramp down the one without power.

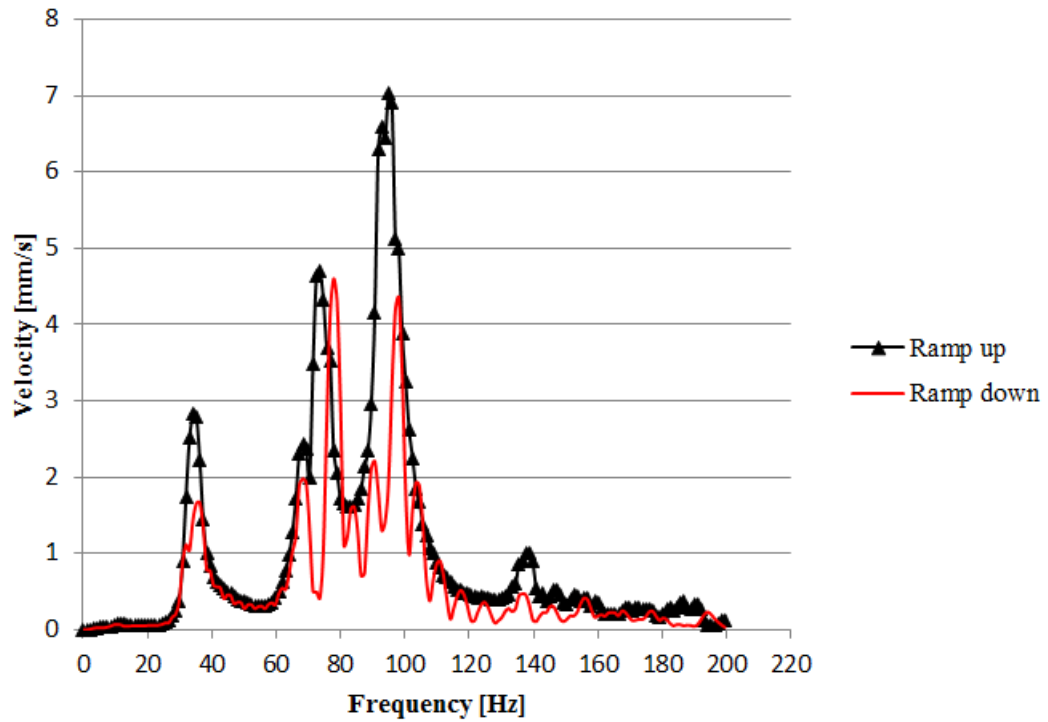


Figure 57. Ramp up with current and down without current in motor end x-direction.

In Figure 57 it can be seen as the natural frequency of the first rotor mode increases by two hertz from 34 Hz to 36 Hz when power is turned off. First motor frame mode increases from 74 Hz to 78 Hz and the second from 93 Hz to 98 Hz.

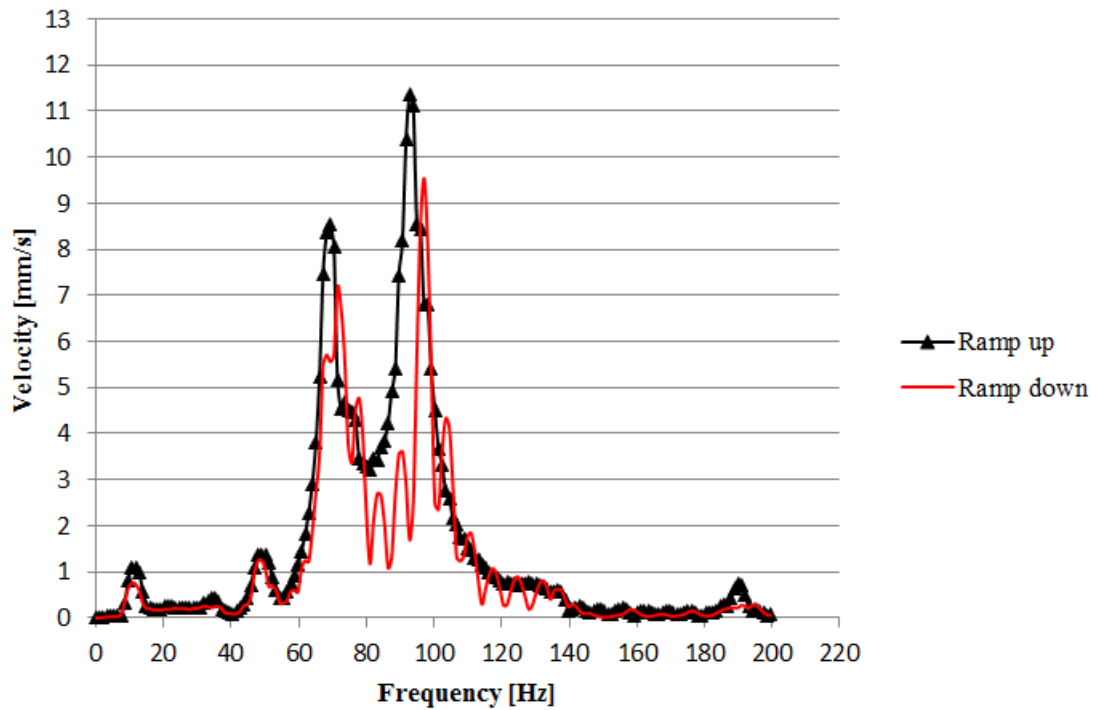


Figure 58. Ramp up with current and down without current in motor end y-direction.

In Figure 58, clear rise in natural frequency can be seen only in the second motor frame dominated mode. The first frame mode mixes with second multiple of the rotor mode and clear shift in natural frequency cannot be discovered. The second frame mode however shifts from 93 Hz to 97 Hz.

According to electric motor manufacturer difference in radial force is small without current and in the case where load consists only from inertia of the rotor and friction. Only these two cases could be tested during the measurements. However, according to these results the current does have effect on the system natural frequencies. The effect is assumed to increase when motor is under full load. As the motor load increases, the magnetic pull increases and the natural frequencies would decrease as it was found out with simulation model.

4.4 Discussion

In chapters 3 and 4 results between simulation model and prototype were compared. First the comparison was performed based on natural frequencies and later on vibration velocities with variable air gap length in the end on the motor. Since electromagnetic force is modelled in a very simple way by using linear springs, the model does not correspond perfectly the prototype. In this chapter simulation model accuracy and possible error sources for inaccuracy are discussed.

4.4.1 Simulation model accuracy compared to prototype

If the accuracy is compared by looking natural frequencies the model seems to correspond well the actual prototype. At first mode the difference is $< 1\%$ and in second mode 4% . Biggest difference occurs at third mode which is 9% . At fourth mode the difference varies between $1\text{--}4\%$ due to variation in measurement results. Even though first four modes are under biggest interest as they are closest to operating range, also the higher modes can be used to compare the model and prototype. Fifth mode occurs around 150 Hz and the difference between the two is $< 1\%$. In the measurements a natural frequency can be found at 171 Hz which not present in the simulation model. One more mode can be seen in both cases close to 190 Hz in which the difference is $< 2\%$. Thus, accuracy of the simulation model in terms of modal analysis is 9% , based on the biggest difference at third mode.

If the accuracy is compared by looking the vibration velocities obtained with 10% error in eccentricity and applied 2.1 g mass unbalance the inaccuracy is more obvious. Table 12 presents vibration velocities on different modes measured from the simulation model and prototype. The corresponding natural frequency at each vibration mode varies as it was stated in the previous chapter.

Table 12. Vibration velocities at first four vibration modes on simulation model and prototype. Frequency of each mode might vary between simulation and measurement results.

Mode	Simulation model, x-direction [mm/s]	Measurement, x-direction [mm/s]	Simulation model, y-direction [mm/s]	Measurement, y-direction [mm/s]
1	2.70	0.42	5.52	2.82
2	6.88	1.37	0.72	0.37
3	4.08	4.68	10.72	4.70
4	10.86	11.38	3.25	6.59

As it can be seen from table 12, the vibration velocities are not as accurate as the natural frequencies between the simulation model and prototype. The table is also lacking velocities produced by the twice-rotation speed excitation since the simulation model does not take it into account. This adds the inaccuracy of the model.

Problems occur also when the motor frame is rotated in the simulation model. According to the measurements it does not have effect on the natural frequencies, yet the rotor dominated natural frequencies change when the air gap length varies in the motor end. Between 0 % and 20 % eccentricity the first natural frequency decreases by four hertz when measured from direction of decreased air gap length. Even though the same shift could not be detected in the actual prototype, it is in a good agreement with research performed by Chen, Yuan & Peng (2015, p. 548): they also found out how natural frequency of a rotor dominated mode decreases as the relative eccentricity increases. However, the change on the second mode is even bigger and not in a good agreement with other research: the second natural frequency increases by 24 Hz. This is assumed to occur because of the simplicity in the electromagnetic force modelling.

4.4.2 Possible errors in the simulation model

Several possible error sources can be found for the simulation model. One major error source is the linear spring elements used to describe the electromagnetic force. Approximate stiffness was given to the springs based on the calculations from electric motor manufacturer. Since the stiffness of the springs affected the first four natural frequencies, it was tuned in order to match the prototype. Difference in the behavior occurred when the air gap length was varied: the prototype did not show any shift in

natural frequencies but in the simulation model shift did occur in the rotor dominated modes, especially in the rotor mode which occurred in perpendicular direction with respect to direction of decreased air gap length. COMBIN14 element, which was used to model the springs, acts as a spring-damper in longitudinal direction. The damping characteristic was ignored by giving it a value close to zero. Stiffness was given negative value in order to simulate the attractive force between the rotor and stator. With the help of springs the rotor dominated modes could be discovered on much lower frequency than without springs. As the air gap length was changed in horizontal direction the length of the spring started to act in direction of hypotenuses instead of y-axis making the spring longer (Figure 59). Since the spring length (l_s) was inversely proportional to the spring force, the magnitude of the force decreased in vertical direction. This was assumed to cause the shift in natural frequencies, since without springs (i.e. attractive force is zero) the rotor dominated frequencies occurred at higher level. Instead of fixing the spring connection points, they should move along the surfaces in order to model the electromagnetic force more accurately.

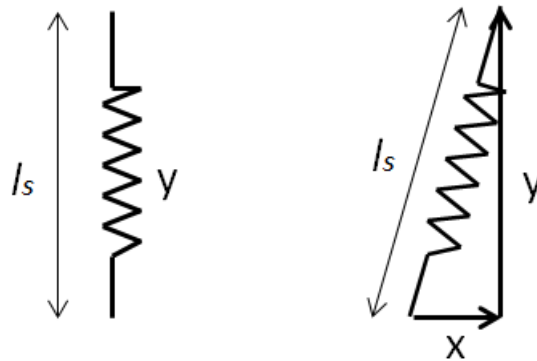


Figure 59. When the motor frame is concentric, the spring force affects in y-direction (left). Frame deflection makes the spring act in hypotenuses direction increasing its length.

Second major reason for inaccuracy is stiffness of the bearings. As the radial force varies, also radial stiffness of the bearings varies. According to bearing manufacturer the force-stiffness-relation is non-linear and very case sensitive. In the simulation model bearings were given constant radial stiffness. Since the radial stiffness affects the natural frequencies of the rotor dominated modes, it should be modelled as a nonlinear variable.

Third major aspect is the lack of 2X excitation in the simulation model. In the measurements it could be clearly seen how resonance is caused by the 2X excitation. In further research source for the twice-rotation speed excitation should be inspected in order to enable its modelling.

In addition, minor error is possible in stator current inspection. When the influence of stator current was inspected with and without current, the engine acceleration and deceleration times varied from each other's. The engine was accelerated from 0 rpm to 4100 rpm in 70 seconds. Free deceleration from 4100 rpm to 0 rpm took approximately 20 seconds. The difference between acceleration and deceleration times can have minor influence on resonance areas.

5 CONCLUSIONS

Vibration analysis of a centrifugal pump with integrated permanent magnet motor was carried out. Research was focused on vibration behavior in radial flux permanent magnet motor. Basic structure of PM motor with radial flux and most common sources of vibrations were presented. In the vibration sources main focus was on once- and twice-rotation speed induced excitations. One of the main sources of vibration was found to be air gap eccentricity. Scope of the work was to investigate the effect of electromagnetic forces in the air gap, which couples the rotor and stator together. It was discovered how stator current is directly related to radial force and radial force was found to be directly related to air gap length. It was also stated that rotor and stator are never perfectly concentric with respect to each other's because of manufacturing tolerances and imperfections. Eccentricity causes unequally distributed air gap length, which again leads to unequal radial force distribution. This causes effect of unbalanced magnetic pull in direction where air gap is shortest. The unequally distributed air gap length was found to be either rotor or stator induced and often caused by manufacturing or installation flaws.

In order to inspect the effect of unbalanced magnetic pull to system vibration behavior, a simulation model of a centrifugal pump with a radial flux permanent magnet motor was constructed. Electromagnetic force was considered as a magnetic spring with negative spring rate in order to simulate the attractive force between the rotor and stator. 18 linear spring elements were distributed equally, and placed between rotor and stator. Approximate spring rate was calculated using 2D-FEA and later on fine-tuned based on the natural frequencies of the prototype. Air gap length in the motor end was modified by rotating motor frame from bearing housing end. Modal analysis was used to discover system natural frequencies and harmonic analysis to inspect the vibration velocities with 0, 10 and 20 % eccentricity in the motor end. Simulation results were verified by performing vibration measurements with a prototype using similar kind of eccentricities.

Simulation model and prototype were compared with 10 % eccentricity and 2.1 g applied unbalanced mass. First rotor dominated mode could be seen in both data at 34 Hz and second at 48 Hz in the measurement data and 50 Hz in simulation model. Vibration

velocity of the first mode was 5.52 mm/s in simulation and 2.82 mm/s in measurement results. In second mode the velocity was 6.89 mm/s in simulation and 1.37 mm/s in measurement results. Difference between the vibration velocities is rather high, but the simulation model is very simplified model of a complex system and does not take into account all structural properties or excitations whose combined effect seem to lower the vibration velocities. Also the damping characteristics were set in a simple manner: 5 % damping was given for the whole structure and electromagnetic damping was not inspected in this research. However, the most important discovering is the natural frequencies which appeared to occur in the operating speed range of the motor. Gyroscopic effect was not found to have significant influence on the rotor dominated modes.

Both motor frame modes could be recognized in vertical and horizontal measurement data, which indicates that direction of vibration is not strictly vertical or horizontal. In the measurements horizontal motor frame bending mode occurs at 74 Hz which is 7 Hz lower than in simulation model. Vertical motor frame mode can be seen between 91–94 Hz which is 1–4 Hz lower than in simulation model. Vibration velocity of the horizontal mode was 10.78 mm/s in the simulation model and 4.70 mm/s in prototype. In vertical mode the corresponding velocities were 10.86 mm/s in simulation model and 11.38 mm/s in prototype. The measurement data showed also resonance caused by twice-rotation speed excitation in second multiple of the rotor dominated modes. These frequencies could be detected close to motor frame bending modes: first one at 68 Hz and second at 96–99 Hz. These frequencies could not be seen in the simulation model because only once-rotation speed excitation was modelled and the model does not take into account multiples of vibration modes.

As the air gap length of the prototype was decreased by 20 % in horizontal direction, vibration velocities in rotor dominated modes decreased. Vibration velocities of other modes and twice-rotation speed excitation increased or decreased depending on the direction of inspection. In simulation model decrease in vibration velocities could be seen in vertical direction when the frame was deflected in horizontal direction. However, a clear influence to vibration velocities was not found with variable air gap length.

According to measurements, decrease of stator current was found to increase system natural frequencies by 2–5 Hz. Similar kind of results were obtained with simulation model: increase in stator current was simulated by increasing the negative spring rate of the springs between stator and rotor which showed decrease in first four natural frequencies. From these results it can be concluded that natural frequencies of the components, which are coupled through electromagnetic force, vary according to stator current and thus required motor torque.

Compared to simulations performed without electromagnetic springs the results were remarkable. If the same system is simulated without the spring elements, critical speeds do not occur in the operating speed range. By taking the electromagnetic force into account, the first rotor dominated natural frequency decreases from 137 Hz to 34 Hz and second from 144 Hz to 50 Hz. Thus, it can be concluded that by considering the electromagnetic force between rotor and stator, two critical speeds can be found in the operating speed range.

In overall, the literature research gave good understanding about the nature of electromagnetic forces. The subject has been investigated a lot, but if the investigation is restricted for example in radial direction as in this case, the amount of information is not overwhelming. Linear relation between the attractive force and air gap length was rather easy to take into account during the simulation process. However, the twice-rotation speeds excitation source, especially in an overhung type rotor structures, was not observed sufficiently in the literature. This restricted the modeling of the excitation and left the model imperfect. Otherwise vibration analysis, even of a complex structure as in this case, is fairly easy to perform if the model is simplified enough. When the model is simplified, one must be careful when setting constraints, contacts and joints. For example in this case it was discovered how radial stiffness of the joints that presented bearings had significant influence on the most interesting natural frequencies.

This simulation method does not perfectly describe the system behavior under variable radial force distribution, but according to this research, spring elements with negative spring rate can be used to simulate vibration behavior of a system where electromagnetic forces occur between rotor and stator.

5.1 Further research

Since the simulation model vibration behavior did not correspond to the prototype perfectly, the subject needs further investigation. True source of twice-rotation speed excitation should be discovered so that it could be applied to the simulation model since clear resonance areas could be detected in the measurements with this excitation. In further research also electromagnetic force modelling should be investigated more. For example by using pressure between the rotor and stator the problem with fixed spring ends could be neglected and possibly get rid of the shift in natural frequencies. In this model the bearing stiffness was constant, but in further research the bearing non-linearity should be inspected more thoroughly and implemented to the simulation model.

In this research only static eccentricity was inspected. Dynamically changing air gap length is realistic in every motor because of rotor related manufacturing and installation tolerances. Dynamically changing air gap could be inspected with the simulation model, but the rotor misalignment is challenging to implement into the actual prototype. One option could be manufacturing of several taper bushings with variable runout in order to force different grades of angular misalignment to the rotor.

Despite the flaws presented in the modelling of the electromagnetic forces, this method can be used in the future in determination of critical speeds in pump-motor assemblies with integrated permanent magnet motor.

REFERENCE

ANSYS. 2015. ANSYS Help Viewer, Version 16.2.0.

Anwar M. N. & Husain I. 2000. Radial Force Calculation and Acoustic Noise Prediction in Switched Reluctance Machines. *IEEE Transactions on Industry Applications*, 36: 6. Pp. 1589–1597

Arkkio, A., Antila, M., Pokki, K., Simon, A., Lantto, E. 2000. Electromagnetic force on a whirling cage rotor. *IEE Proceedings Electric Power Applications*, 147: 5. Pp. 353–360.

Aura L. & Tonteri A. J. 1996. Teoreettinen sähkötekniikka ja sähkökoneiden perusteet [in Finnish]. 2. uudistettu painos. Porvoo: WSOY. 448 p.

Chen, X., Yuan, S. & Peng, Z. 2015. Nonlinear vibration for PMSM used in HEV considering mechanical and magnetic coupling effects. *Nonlinear Dynamics*, 80: 1. Pp. 541–552.

Chin, Y. K., Kanninen, P., Maki-Ontto, P., Sakki, R., Lendenmann H. 2009. Phenomenon of Magnetic Force in Permanent Magnet Wind Turbine Generators. *International Conference on Electrical Machines and Systems, 2009. ICEMS 2009*. Pp. 1–6.

Deshpande, U.S. 2003. Recent advances in materials for use in permanent magnet machines-a review. *Electric Machines and Drives Conference, 2003. IEMDC'03. IEEE International*, 1. Pp. 509–515.

Hanselman, D. 2006. *Brushless Permanent Magnet Motor Design. Second Edition*. Ohio: Magna Physics Publishing. 411 p.

Haring, T., Forman, K., Huhtanen, T. & Zawadzki M. 2003. Direct drive-opening a new era in many applications. *Pulp and Paper Industry Technical Conference, 2003. Conference Record of the 2003 Annual*. Pp. 171–179.

Huurinainen, K. 2016. VS: SHS pumpun värähtelyn lähteet kestopagneettimoottorilla [private e-mail]. Receiver: Atte Posa. Sent 10.08.2016, 15.19 o'clock (GMT+0200). Attachment: "SHS-Magneettivoimat_20160809.xlsx"

Inman, D. 2001. Engineering Vibrations. Second edition. New Jersey: Prentice-Hall Inc. 621 p.

Islam, J., Svechkarenko, D., Chin, R., Szucs, A., Mantere, J. & Sakki, R. 2012. Cogging torque and vibration analysis of a direct-driven PM wind generator with concentrated and distributed windings. Electrical Machines and Systems (ICEMS), 15th International Conference, October 2012. Pp. 1–6.

Islam, M. R. 2009. Cogging Torque, Torque Ripple and Radial Force Analysis of Permanent Magnet Synchronous Machines. Doctoral dissertation. University of Akron. 200 p.

Jahromi, A., Bhat, R. & Xie, W. 2015. Forward and Backward Whirling of a Rotor with Gyroscopic Effect. Mechanisms and Machine Science, Vibration Engineering and Technology of Machinery, 23. Pp. 879–887.

Kim, T., Hwang, S. & Park, N. 2000. Analysis of vibration for permanent magnet motors considering mechanical and magnetic coupling effects. IEEE Transactions on Magnetics, 36: 4. Pp. 1346–1350.

Krishnan, R. 2010. Permanent Magnet Synchronous and Brushless DC Motor Drives. Boca Raton, Florida: CRC Press. 575 p.

Overshott, K. 1991. Magnetism: It is permanent. IEE Proceedings A, 138: 1. Pp. 22–30.

Parviainen, A. 2005. Design of axial-flux permanent-magnet low-speed machines and performance comparison between radial-flux and axial-flux machines. Lappeenranta: 19.04.2005. Doctoral dissertation. Lappeenranta University of Technology. 153 p.

PSK 5707. 2011. Vibration Measurement in Condition Monitoring. Diagnosis. 5th edition. PSK Standards Association. 34 p.

Puranen, J. 2006. Induction motor versus permanent magnet synchronous motor in motion control applications: a comparative study. Lappeenranta: 5.12.2006. Doctoral dissertation. Lappeenranta University of Technology. 147 p.

Pyrhönen, J., Jokinen, T. & Hrabovcová, V. 2008. Design of rotating electrical machines. Chichester: Wiley. 512 p.

Sopanen, J. 2015. Lecture material. Machine Dynamics. Lappeenranta: Lappeenranta University of Technology.

Srisiriwanna, T. & Konghirun, M. 2012. A study of cogging torque reduction methods in brushless dc motor. In: Electrical Engineering/Electronics, Computer, Telecommunications and Information Technology (ECTI-CON), 2012 9th International Conference, May 2012. Pp. 1–4.

Sulzer. 2016. Guideline for Finite Element Analysis of Pump Casing. [Sulzer Intranet] Updated 1, 2015. [Referred 26.10.2016].

Taplak, H., Erkaya, S. & Uzmay, İ. 2013. Experimental analysis on fault detection for a direct coupled rotor-bearing system. Measurement, 46: 1. Pp. 336–344.

Tarhonen, K. 2016a. FW: FMR-Moottorit Ahlstarssissa [private e-mail]. Receiver: Atte Posa. Sent 30.05.2016, 10.25 o'clock (GMT+0200). Attachments: "A0-1111-A.pdf", "A0-1110-A.pdf".

Tarhonen, K. 2016b. Product Development Engineer, Sulzer Pumps Finland Oy. Private conversation 2.5.2016.

Taylor, J. 1994. The vibration analysis handbook. First Edition, Second Printing. Florida: Vibration Consultants. 360 p.

Tenhunen, A., Benedetti, T., Holopainen, T. P. & Arkkio, A. 2003. Electromagnetic forces of the cage rotor in conical whirling motion. *IEE Proceedings: Electric Power Applications*, 150: 5. Pp. 563–568.

Tiwari, M., Gupta, K. & Prakash, O. 2000. DYNAMIC RESPONSE OF AN UNBALANCED ROTOR SUPPORTED ON BALL BEARINGS. *Journal of Sound and Vibration*, 238: 5. Pp. 757–779.

Tong, W. 2014. *Mechanical Design of Electric Motors*. Florida: CRC Press.

Virtanen, S. 2016. Product Development Manager, Sulzer Pumps Finland Oy. Private conversation 2.5.2016.

Werner U. & Binder A. 2005. Dynamic analysis due to eccentricity in asynchronous machines. In: *SDEMPED 5th IEEE International Symposium Diagnostics for Electric Machines, Power Electronics and Drives*, held at Vienna, Austria 7-9 September, 2005. IEEE Conference Publications. Pp. 1–6.

Yamamoto, T. & Ishida, Y. 2001. *Linear and Nonlinear Rotordynamics: A Modern Treatment with Applications*. New York: Wiley cop. 325 p.

Zeraoulia, M., Benbouzid, M. E. H. & Diallo, D. 2006. Electric Motor Drive Selection Issues for HEV Propulsion Systems: A Comparative Study. *IEEE Transactions on Vehicular Technology*, 55: 6. Pp. 1576–1764.

Zhu, H. & Li, H. 2015. Magnetic Field Equivalent Current Analysis-Based Radial Force Control for Bearingless Permanent Magnet Synchronous Motors [web document]. Zhenjiang: May 2015 [Referred 26.10.2016]. *Energies* 2015, 8: 6. Pp. 4920–4942. Available in PDF-file: <http://www.mdpi.com/1996-1073/8/6/4920>.

Zhu, Z., Chen, J., Wu, J. & Howe, D. 2008. Influence of Stator Asymmetry on Cogging Torque of Permanent Magnet Brushless Machines. *IEEE Transactions on Magnetics*, 44: 11. Pp. 3851–3854.

Simulation model contact pairs.

Table I.1 Contact pairs. In all connections contact type was bonded and formulation was set to MPC.

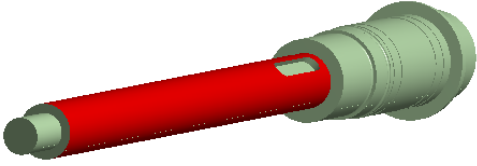
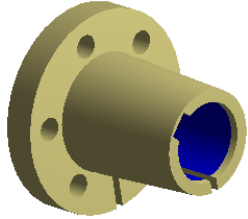
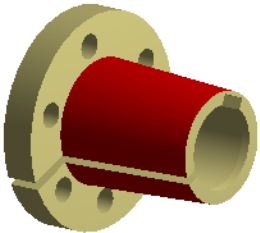
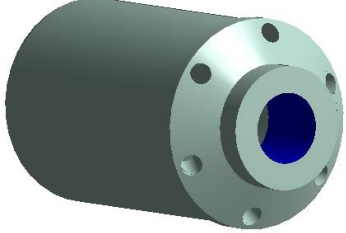
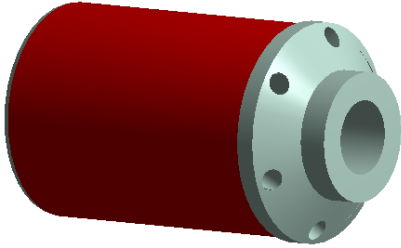
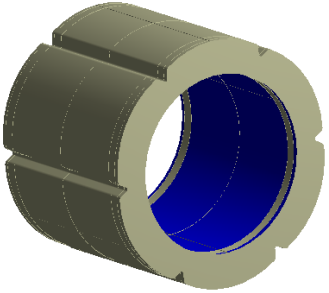
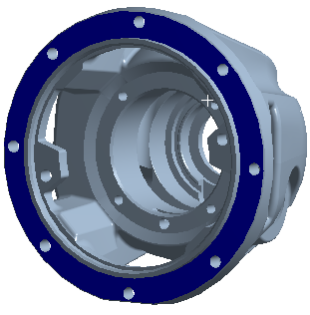
Case	Contact	Target
1		
2		
3		
4		

Table I.1 continues. Contact pairs. In all connections contact type was bonded and formulation was set to MPC.

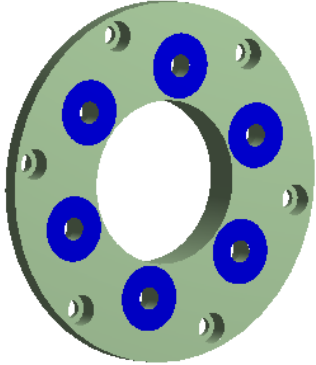
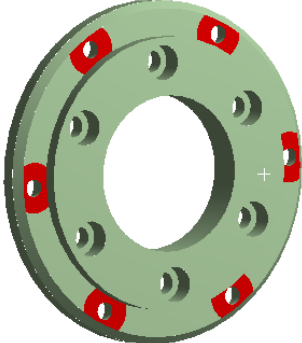
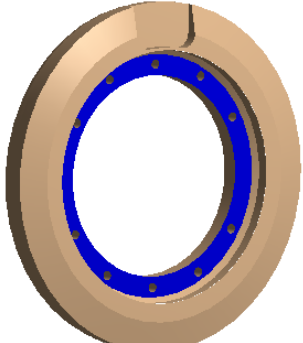
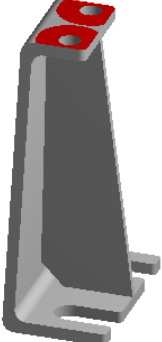
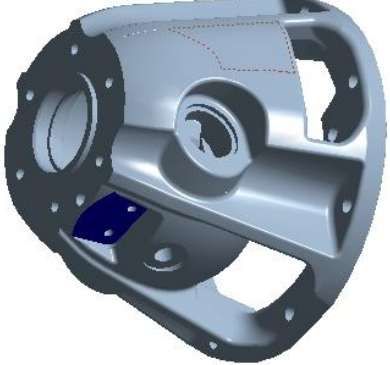
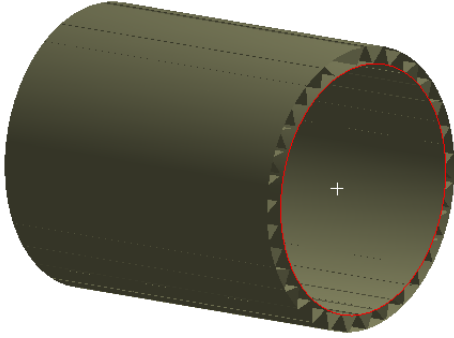
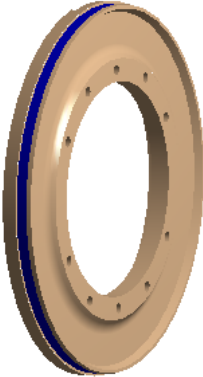
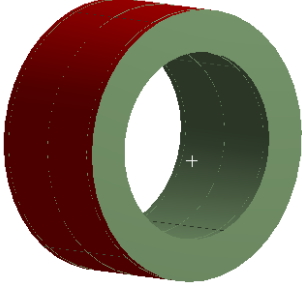
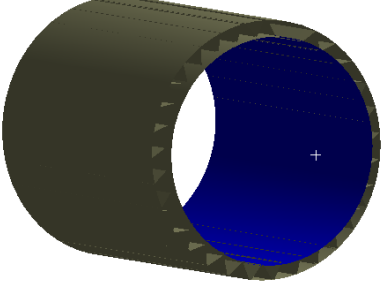
Case	Contact	Target
5		
6		
7		

Table I.1 continues. Contact pairs. In all connections contact type was bonded and formulation was set to MPC.

Case	Contact	Target
8		
9		

Natural frequencies and mode shapes for concentric rotor/stator

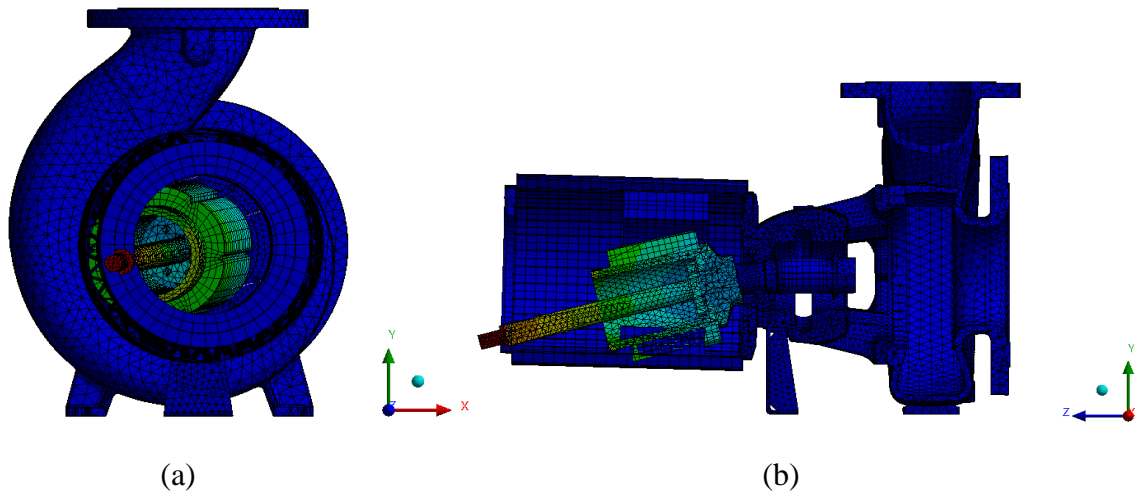


Figure II.1. 1st vibration mode at 33.99 Hz (a) and 2nd at 49.69 Hz (b).

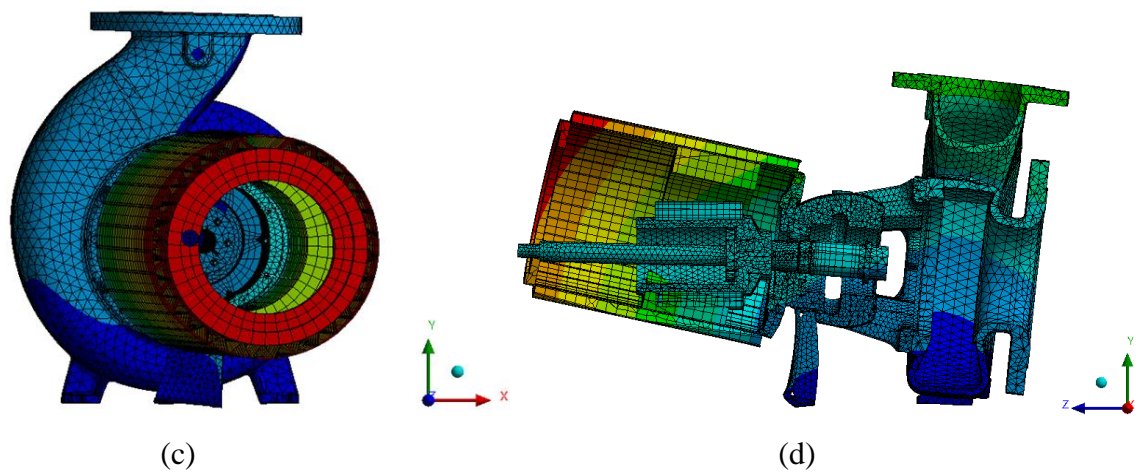


Figure II.2. 3rd vibration mode at 81.13 Hz (c) and 4th at 95.48 Hz (d).

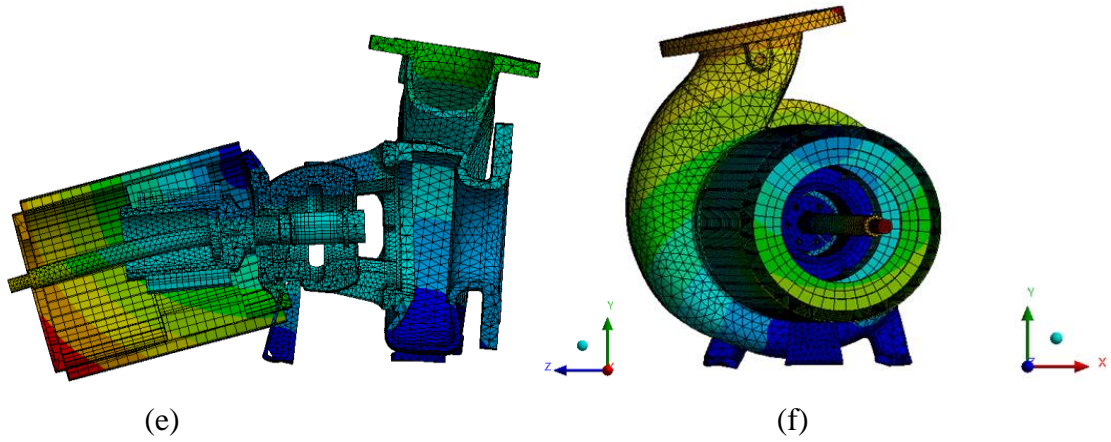


Figure II.3. 5th vibration mode at 151.75 Hz (e) and 6th at 195.3 Hz (f).

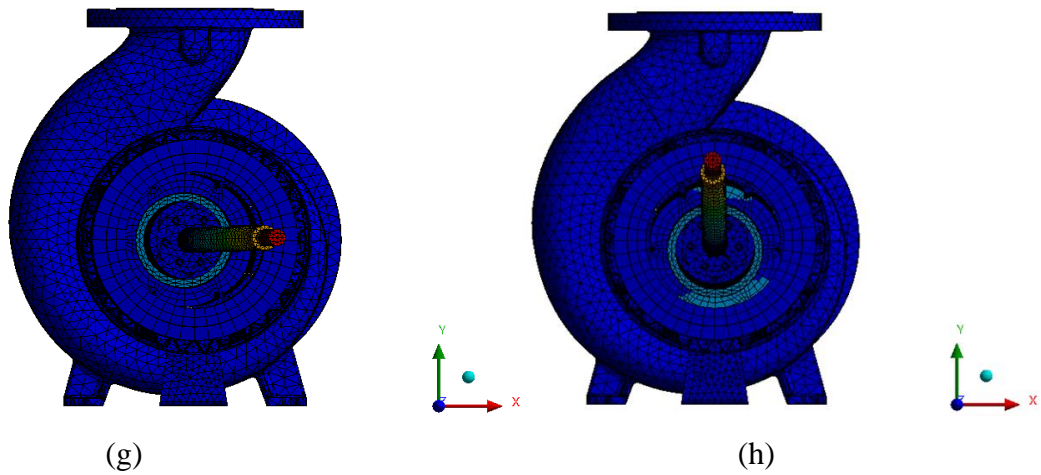


Figure II.4. 7th vibration mode at 266.77 Hz (g) and 8th at 268.29 Hz (h).

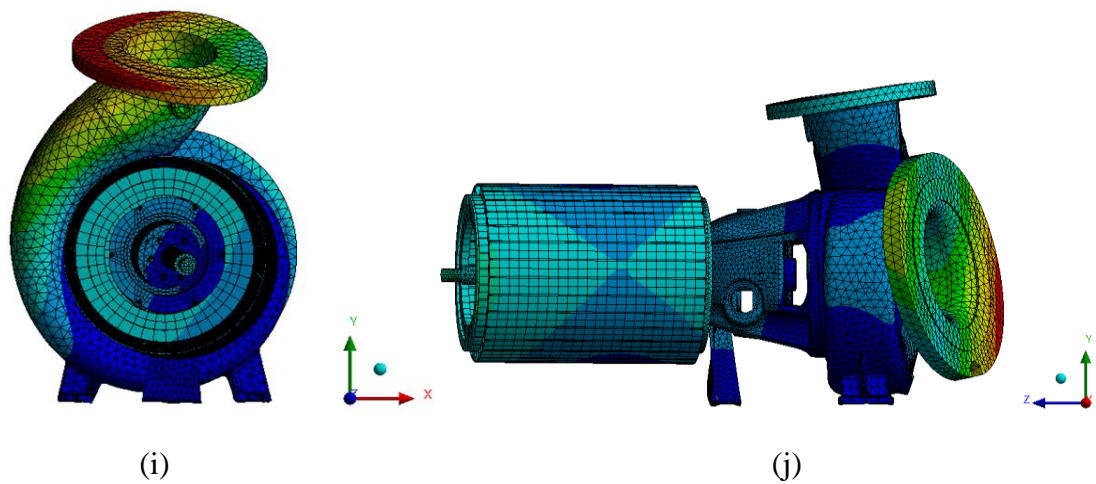


Figure II.4. 9th vibration mode at 315.12 Hz (i) and 10th at 355.24 Hz (j).

Ansys Commands

```

U_mag = 1.05e-4      !Unbalance magnitude to be applied = 2 gram at 52.5 mm
radius
iNode = 279         !Node number where unbalance is applied
F,iNode,fx,U_mag   !These commands will apply unbalance.
F,iNode,fy,, -U_mag !Force will rotate in XY plane from X-axis to Y-axis (around
positive Z-axis)

kbc,1               !Specifies stepped loading
CMOMEGA,ROOTTORI,,3000*0.10471976 !Rotational velocity for Coriolis
Effect
coriolis,on,,,on   !Activation of Coriolis effect
SYNCHRO,,,Roottori !Specifies the excitation frequency
to be synchronous with the
rotational velocity of the
structure

```

Measurement results

Table IV.1. Measurement results without applied unbalanced mass on different motor frame eccentricities in vertical direction.

Mode	Frequency [Hz]	Velocity, 0 % ecc. [mm/s]	Velocity, 10 % ecc. [mm/s]	Velocity, 20 % ecc. [mm/s]
1	34	0.72	0.43	0.44
2	48	1.59	1.04	1.35
1 (2X)	68	12.79	12.92	3.74
3	74	3.43	6.24	8.45
4	93-95	9.54	8.81	6.07
2 (2X)	96-99	8.89	10.17	9.82

Table IV.2. Measurement results without applied unbalanced mass on different motor frame eccentricities in horizontal direction.

Mode	Frequency [Hz]	Velocity, 0 % ecc. [mm/s]	Velocity, 10 % ecc. [mm/s]	Velocity, 20 % ecc. [mm/s]
1	34	3.00	2.01	2.63
2	48	0.49	0.37	0.45
1 (2X)	68	1.68	1.29	1.79
3	74	3.89	6.48	6.43
4	93-95	4.39	5.47	6.28
2 (2X)	96-99	5.10	5.45	3.86

Table IV.3. Measurement results with 2.1 g applied unbalanced mass on different motor frame eccentricities in vertical direction.

Mode	Frequency [Hz]	Velocity, 0 % ecc. [mm/s]	Velocity, 10 % ecc. [mm/s]	Velocity, 20 % ecc. [mm/s]
1	34	0.81	0.42	0.47
2	48	1.88	1.36	1.93
1 (2X)	68	16.64	8.53	13.01
3	74	3.26	4.68	6.92
4	91-93	9.13	11.38	5.89
2 (2X)	95-97	9.14	6.79	8.10

Table IV.4. Measurement results with 2.1 g applied unbalanced mass on different motor frame eccentricities in horizontal direction.

Mode	Frequency [Hz]	Velocity, 0 % ecc. [mm/s]	Velocity, 10 % ecc. [mm/s]	Velocity, 20 % ecc. [mm/s]
1	34	3.76	2.82	3.15
2	48	0.50	0.39	0.51
1 (2X)	68	3.15	2.43	4.29
3	74	4.80	4.70	6.32
4	93-95	3.04	6.59	5.48
2 (2X)	95-97	2.84	7.03	5.65